Design and Synthesis of Reactive Aramid Nanostructures for Advanced Nanocomposites with Tailored Morphology and Properties

by

Keqin Cao

A dissertation submitted in partial fulfillment
of the requirements for the degree of
Doctor of Philosophy
(Mechanical Engineering)
in the University of Michigan
2013

Doctoral Committee:

Professor Ellen M. Arruda, Co-Chair
Professor Michael Thouless, Co-Chair
Professor Nicholas A. Kotov
Professor Joerg Lahann
Professor Anthony M. Waas, Cognate

To my mom, dad and my husband Kevin

Acknowledgements

This thesis would not have been possible without the help and support of my committee, my colleagues, my friends and my family. First, I would like to express my sincere gratitude to my co-advisors Prof. Ellen M. Arruda and Prof. Michael Thouless for their tremendous guidance, encouragement, support, and trust in me during the past five years. The good advice, support and friendship of my supervisors have been invaluable on both an academic and a personal level, for which I am extremely grateful. I am also very grateful for their knowledge and research skills. I am always encouraged and inspired by their passion towards research. I appreciate the brilliant ideas that they provided to me and their accessibility whenever I needed help and guidance. Their attention, moral support and timely suggestions have been useful at every stage of my PhD study throughout the past five years.

Next, I would like to thank Prof. Anthony M. Waas, Prof. Nicholas A. Kotov and Prof. Joerg Lahann for their valuable advice and participation in my dissertation committee. I appreciate working with Prof. Anthony M. Waas and Prof. Nicholas A. Kotov of Aerospace Engineering and Chemical Engineering department respectively throughout my PhD work. I am thankful to Prof. Waas for his guidance and brilliant ideas at modeling composite materials. I am thankful to Prof. Kotov for all his guidance and discussion on polymer chemistry and polymer physics. Their broad knowledge of the fields helped me to have a better vision of my goals. I am also thankful to Prof. Lahann for providing me access to his FTIR equipment and collecting important experiment data.

Next, I would like to thank Prof. John Kieffer for access to Raman spectroscopy in his laboratory. I am grateful to Prof. Samantha H. Daly for access to her lab equipment and Prof. Ralph T. Yang for access to filtration systems and ovens. I would like to thank Prof. Wayne Jones for the research opportunity with him during my junior and senior years as an undergraduate student. This opportunity made me interested in research and decided to go to graduate school. I also want to express my gratitude to Robin Fowler from Program in Technical Communication for her help with my dissertation writing.

I appreciate working with Amit, Jinjin, Tanaz, Jess, Harish and Kaitlyn from my lab; Ming, Bongjun and Jian from Prof. Kotov's group; Jared, Yue, Adam and Kyubum from Prof. Daly's group; Eugene and Evan from Prof. Waas's group; Lang from Prof. Kieffer's group and Aftin from Prof. Lahann's group. Specifically, I am thankful to Amit, Jess and Jian for their help in training me with experiment setups. I would like to thank Eugene, Bongjun, Lang and Aftin for the help with collecting experiment data. I need to express my gratitude to Jared for the collaboration on the modeling work and to Adam for his preparation of gold nanoparticles.

I also appreciate working with many undergraduate students, Carlos, David, Bret, John, Jason F., Ryan, Staci, Grace and Jason L., who worked with me closely and assisted me with experiment. Their hard work and discussions with me on research also greatly helped me with my PhD work. Specifically, I would like to thank Carlos for his tremendous passion and effort in carrying out experiment and having long discussions with me in the past three years. His knowledge and passion in chemical engineering gave me great influence and motivation.

Next, I would like to thank my friends and roommates in Ann Arbor: Shinuo, Yue, Ling, Jenny, Jinjin, Hanxiao, Lu, Chen, Mingming, Yihan, Yifeng, Bin, Tong, Qiliang, Yinghao, Yijun, Xiaofei, Hao, Jian, Boyun, Zhaori, Bangxin, Jiangpeng, Ye, Jun, Sean, Jeremy, George and many others. I appreciate so much for your accompany and support. I cherish our friendships so much and hope they shall always last.

Lastly, I would like to give my deepest appreciation to my parents and my husband Kevin. Without their trust, support, patience, and love, I could not have overcome the hardships and difficulties during the past five years. I would like to thank my parents for their great love and their long-distance phone calls whenever I need support. They are always the best and I feel so loved and lucky to have them. I would like to thank Kevin for always being so caring, patient and supportive to me. Thank you for always forgiving me when I lost control of my temper, for helping me organize my thoughts when I felt lost and for encouraging me when I was lack of my confidence. Thank you for being such a perfect husband. To all of you, I dedicate this dissertation.

This work was financially supported by the Office of Naval Research, the Department of Mechanical Engineering, and Rackham Travel Grant.

Table of Contents

List of Figures

Figure

List of Tables

Table

Abstract

The higher strength-to-weight ratios of nanocomposites have made them novel materials to replace metals in applications requiring high material performance such as windmill blades or aircraft components. Nanofiller-reinforced polymer nanocomposites are formed primarily through dispersing strong and stiff nanoparticles in various polymeric matrices, and much of the recent work on nanocomposite mechanics only focuses on improving the reinforcement phase, e.g. the dispersion of nanofillers. The design of high-performance nanocomposites, however, also requires polymeric matrices with superior mechanical properties and versatile techniques to tailor these matrices. Suitable polymeric nanoscale building blocks for advanced composite matrices can be prepared from conventionally strong materials. In this dissertation, a high performance polymer poly-paraphenylene terephtalamide (PPTA), better known as Kevlar or aramid polymer, is employed as a matrix material in the form of nanoscale building blocks for nanocomposites. The synthesis of reactive aramid nanoscale structures has addressed the limitations in the field of synthetic nanocomposites, which has traditionally relied on a set of polymeric building blocks with low reactivity and of limited variability.

Reactive nanoscale aramid structures are created to bond with various moieties to form aramid networks with tailored nanostructures, morphologies, and mechanical properties. Stable dispersions of nanoscale Kevlar fibers with diameters between 3 and 30 nm were first obtained through deprotonating macroscale, commercial Kevlar yarns. The high-aspect-ratio aramid nanofibers were then functionalized to improve their reactivity for bonding by surface treating with phosphoric acid (PA). The PA hydrolysis treatment resulted in two aramid building block nanostructures: nanofibers or nanosheets, depending on the treatment extent. Thirdly, the reactive aramid nanostructures were used as polymeric building blocks that can form strong interactions with citrate-stabilized gold nanoparticles (AuNPs). The resulting Kevlar/gold nanocomposites have an optimized combination of stiffness, strength and strain to failure owing to the reinforcement effect of the metal particles (i.e. AuNPs) through their bonding with the aramid matrix. Through

Fourier-transform infrared spectroscopy, transmission-electron microscopy, uniaxial tensile testing, ultraviolet–visible spectroscopy and thermo-gravimetric analysis, the chemical structures, morphologies, and interactions among the constituents of the nanocomposites, as well as their mechanical and thermal properties were characterized. A structure-property relationship was obtained to systematically tailor and optimize the mechanical properties of these advanced aramid nanofiber/gold nanoparticle composites.

These results are the first demonstration of the possibility for aramid nanoscale fibers to form versatile nanosized building blocks that can then be crosslinked or conjugated to fabricate composite structures involving materials previously thought to be impossible to use in such applications, and thus creating a new generation of nanostructured aramid materials. The Kevlar/gold nanocomposites synthesized based on aramid nanostructures have a higher strain energy density than that of a commercial plain-woven Kevlar mat tested along its strongest axis, thus indicating their potential as high performance materials to resist extreme high rate loadings such as blasts.

Chapter 1

Project Motivation and Outline

Mechanical engineers and material scientists are always in search of new high-performance materials that can be used for industrial and commercial applications. Studies on natural materials with high strength and high toughness have revealed complex hierarchical structures of those materials. Nacre, wood and bone are all biological composites with hierarchical architectures to account for their attractive physical or mechanical properties. These discoveries have inspired the design of synthetic nanocomposites to mimic such properties. Much of the recent work on nanocomposite mechanics focuses on improving the reinforcement phase, such as carbon nanotubes and graphene nanosheets. Many studies have been looked into how to effectively utilize those nanofillers in polymer matrices through improving their bonding and dispersion. However, the design of high-performance nanocomposites also requires polymeric matrices with superior mechanical properties and versatile techniques to tailor these matrices. Traditionally, the field of synthetic nanocomposites has relied on a fairly limited set of polymeric building blocks, many with low reactivity and of limited variability. These limitations are addressed in this thesis by the creation of functionalized nanoscale aramid structures, in the form of nanofibers and nanosheets. A high performance polymer poly-paraphenylene terephtalamide (PPTA), better known as Kevlar or aramid, was employed as a matrix material in high strength and high toughness polymer nanocomposites. Two crucial aspects were considered in this work: 1) designing a nanoscale material structure to probe the possibility of controlling the resulting mechanical properties and deformation mechanisms in the material upon loading; and 2) optimizing a synthetic process to obtain a controlled manner of assembling molecules which will yield a desired material structure.

The objective of this thesis is to effectively employ Kevlar, as a matrix material, in ultra-high strength and high toughness polymer nanocomposites with tailorable properties. In order to obtain an optimized synthesis strategy of aramid-based nanocomposites, the structure-property relationship of the synthesized materials is investigated through various characterization methods to probe their microstructure, morphology and material properties. Specifically, Chapter 2 first reviews the current state of deformation mechanisms in nanofiller-reinforced polymer composites. The mechanical properties and reinforcement effect of those nanocomposites are compared with the aramid nanocomposites developed in this work. Second, the limitations of commercial Kevlar yarns and microfibers are discussed in detail. Third, an introduction of how to control the size of gold nanoparticles and how to characterize their interactions with polymers are also discussed with details.

Chapter 3 details the synthesis of aramid-based nanocomposites and various experimental characterization techniques. The synthesis process includes the dispersion of aramid nanofibers, the assembly of aramid networks through layer-by-layer and vacuum-assisted filtration methods, and the chemical treatment of aramid nanofibers with phosphoric acid, glutaraldehyde and citrate. The characterization techniques include mechanical, thermal, morphological and structural characterization. Uniaxial tensile testing and dynamic mechanical analysis are used to characterize the mechanical properties of the nanocomposites. Transmission electron microscopy and scanning electron microscopy are used to visualize the material morphology. Fourier-transform infrared spectroscopy is used to analyze the change in chemical structures of nanocomposites.

Chapter 4 investigates the nature of aramid nanofibers (ANFs) to understand how they can be used as nanoscale building blocks to assemble ANF-based films. The morphology and dimension of ANFs dispersed in dimethyl sulfoxide are investigated. Various ANF-based materials are assembled via the layer-by-layer method and the resulting network mechanical properties are characterized. Strategies to functionalize and crosslink ANFs are discussed.

In Chapter 5, the detailed reaction mechanisms of the phosphoric acid/glutaraldehyde (PA/GA) treatment are discussed. A family of PA/GA treated aramid films is synthesized with various amounts of PA and GA for a parameter study of how each treatment step affects the properties. Various characterizations on the PA/GA treated aramid-based networks are carried

out to reveal how the treatment controls the aramid nanostructures, network morphology and mechanical properties.

Chapter 6 compares the stiffness of three Kevlar fiber based networks measured via low strain rate uniaxial tensile testing. The three networks are commercial plain-woven Kevlar mats, aramid nanofiber networks assembled by the layer-by-layer method and aramid nanofiber networks assembled by the filtration method. Through observation of the network microstructure and analytical results obtained from modeling, the effect of the fiber geometry and fiber orientation on the network stiffness is discussed.

In Chapter 7, Kevlar/gold nanocomposites (aramid nanostructures reinforced by gold nanoparticles (AuNPs)) are synthesized with an outstanding combination of stiffness, strength and strain to failure. Details of how each constituent, phosphoric acid (PA), citrate and AuNPs, affects the resulting mechanical properties are investigated in great detail. Optimized levels of each treatment step: the PA hydrolysis, citrate crosslinking and AuNP reinforcement were applied to make AuNPs-reinforced aramid nanocomposites, based on their structure-property relationships.

Finally, Chapter 8 briefly summarizes the work presented in this thesis, highlighting the significance of the results obtained and suggesting future efforts in developing aramid-based nanocomposites.

Chapter 2

Introduction

2.1 The State of Deformation Mechanisms in Nanocomposites

Much effort has been focused on designing novel light-weight materials with ultra-high mechanical properties [1-6]. The higher strength-to-weight ratios of nanocomposites have made them novel materials to replace metals in applications requiring high material performances such as windmill blades or aircraft components. The idea of combining nanoparticles with polymers to form novel nanocomposites has attracted considerable attention in material research, as it offers possibility and versatility to yield multifunctional and advantageous macroscopic properties by controlling materials down to the nanoscale [5-8]. On the other hand, studies on the micro-architecture of nacre, a natural nanocomposite with amazing mechanical properties, have inspired us with its 'brick-and-mortar' arrangement that combines ceramic platelets and polymer to yield high toughness [**7**]. Dispersing strong, highly stiff nanoparticles, fibers or ceramic platelets in polymer matrices, thus, has been a paradigm for the design of high-performance light-weight nanocomposites.

2.1.1 The Structural Features of Nacre: A Biomaterial

Many natural materials demonstrate exceptional mechanical properties that surpass those of synthetic composites. Natural fibers like spider dragline silk are renowned for their high strength, hardness and toughness [8]. Nacre, an inner layer of abalone shells, is another

composite that demonstrates these great properties due to its sophisticated structure on different scales [9]. The hierarchical structure of nacre enables different mechanisms from the nanometer scale to the micrometer scale, which contributes to its renowned toughness and other exceptional properties [9, 10]. Understanding the structure of nacre and its unique features and mechanisms at different scales has provided inspiration for the design of synthetic composites.

Nacre is a composite composed of ~ 95 vol% aragonite ($CaCO_3$) tablets, which are sandwiched in thin polymer layers [9]. An aragonite tablet is very fragile, but after being composited with a small fraction of organic materials, it becomes 3,000 times more fracture resistant than a single crystal of the pure mineral [9]. However, synthetic materials made of interlocking ceramic tablets bound by a small amount of ordinary adhesives do not have toughness comparable to nacre [10]. The sophisticated structure of nacre is a hierarchical design that enables various mechanisms at different scales from nanometer to macroscopic sizes [10]. Figure 2.1 demonstrates this stacking pattern of the aragonite plates through observations on a piece of freshly cleaved nacre in scanning electron microscopy (SEM). The interpfaces of the aragonite plates are about 20 to 40 nm thick and are composed of different types of bio-molecules organized in a complex way. Direct connection between the aragonite plates is observed across the thin polymer layers and nanoasperities are also observed on the surfaces of the aragonite plates, both of which are believed to be important factors to toughen the material [8, 9].

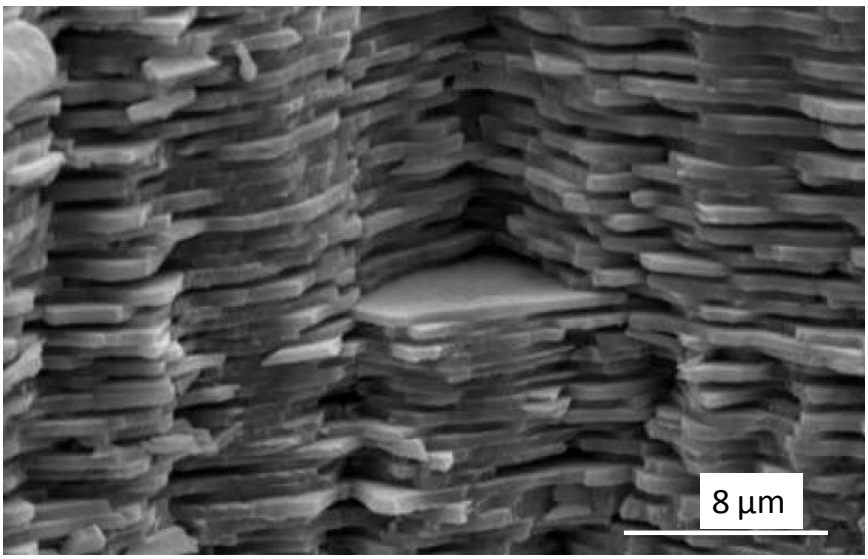

Figure 2.1 A SEM image showing the stacking pattern of the aragonite plates being sandwiched by the organic adhesive. Image in the public domain. Downloaded from http://commons.wikimedia.org/wiki/File:Bruchfläche_eines_Perlmuttstücks.JPG on May 6, 2013.

Through various structural observations and characterization of the different structural features of nacre, the sophisticated hierarchical structure of nacre that enables its different deformation mechanisms at various scales is revealed. Nacre is comprised of 95 vol% ceramic aragonite layers and organic polymer layers. The polymer layer serves as an adhesive, with a component called Lustrin A, which has a modular structure with domains that can be opened upon loading. This structure has subunits that have intermediately strong bonds and can be unfolded sequentially [8]. The great toughness of the polymer layer comes from its good ducitity and an intermediate strength. The aragonite tablets are around 15 times thicker than the polymer layers. Under SEM, both asperities and the direct connection between two tablets are found on the surfaces of the tablets. The asperities on the surface of the tablets serve as restrictions to sliding motion between the tablets and the adhesive layers under shear; thus effective load transfer is achieved and toughness is enhanced. Through nano-indentation tests and using a finite element model to fit the force-deflection curves obtained by the indentation, the Young's modulus of both the tablet and confined interfacial layer were determined to be

79 ± 15 GPa and 2.84 ± 0.27 GPa. Figure 2.2 shows the tensile mechanical deformation response of nacre, with its Young's modulus determined to be 34 GPa [9].

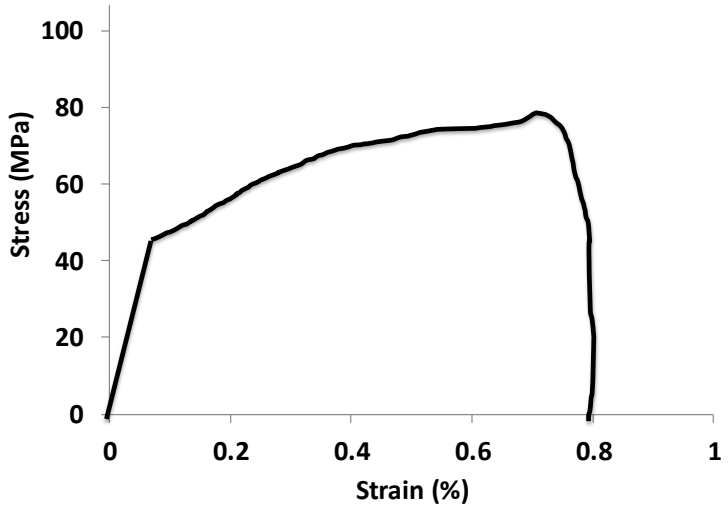

Figure 2.2 Stress strain curve of nacre under uniaxial tension from uniaxial tensile experiment. The model captures the stiffness of nacre accurately. Figure adapted from Barthelat et al., 2006 [9].

2.1.2 Synthetic Nanocomposites

The structural features of nacre have shed light on the design of synthetic nanocomposites for obtaining excellent mechanical properties. The development of nanofillers with high stiffness and strength, on the other hand, also provides the possibility to mimic the structural features of nacre by embedding them in various polymer matrices [1, 5, 6, 11-16**]**. The most common nanofillers are carbon nanotubes (CNT), graphene nanosheets (GNS) and montmorillonite (MTM) clay particles, as shown in Figure 2.3SW. CNTs are composed of carbon atoms arranged in a hexagonal pattern. Single walled carbon nanotubes (SWNTs) are single rolled graphite sheets with a diameter of 1-2 nm and variable length [17]. Multi-walled carbon nanotubes (MWNTs) consist of concentric shells of rolled graphite sheets with typically much larger diameters. The SWNTs have ultimate tensile strengths in the

range of 10-300 GPa and a Young's modulus of approximately 1100 GPa, which have been heralded to be the strongest material on the earth. The crystal structure of MTM consists of layers made up of two silicon atoms fused to an octahedral sheet of aluminum. Each silicate layer is a rigid inorganic polymer consisting of mainly silicon and oxygen, and a small amount of aluminum, magnesium and other metal ions. An alkali metal cation (typically, Na+) holds the silicate layers together by an intermolecular force. Each silicate layer has a thickness of around 1 nm. The Young's modulus of graphene nanosheets is on the order of 1100 GPa and that of clay nanosheets is about 150-300 GPa [18, 19].

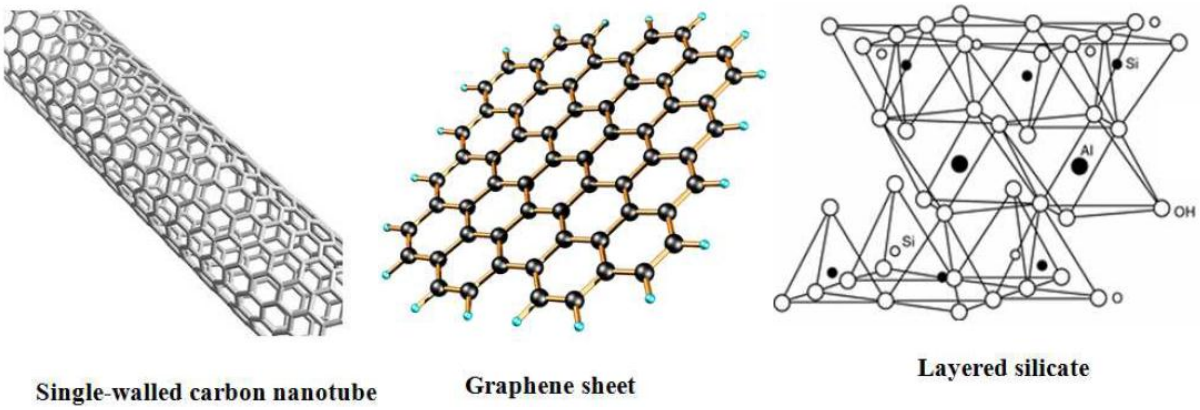

Figure 2.3 Common nanofillers in nanocomposites. Figure adapted from thesis of Kaushik, 2010 [20].

Despite the outstanding properties of these nanofillers, several challenges have hindered the development of nanoparticle-reinforced polymer nanocomposites from achieving desired nanocomposite properties [21]. As both the bonding of nanoparticles with polymer matrices and the dispersion of nanoparticles determine the effective load transfer from polymer matrices to nanofillers [5, 21], the inertness and aggregations of the common nanofillers have caused major problems in utilizing them more effectively. The low surface affinity of CNTs and GNSs makes it hard to scale up their excellent mechanical properties at the nanoscale to properties at the macroscopic scale [3, 16, 22]. Much effort has been raised to

functionalize CNTs and GNSs, in order to achieve better bonding with polymers. However, their reinforcement effect is only prominent when a weight fraction of ~ 1 to 2 % is implemented in nanocomposites. Further addition usually either fails to or degrades composite mechanical properties owing to the aggregation of and weak interactions between nanofillers and polymer matrices [16, 23]. Table 2.1 shows the magnitudes of mechanical properties of various nanocomposites with CNT, MTM or GNS as nanofillers in polymer matrices and the effect of the reinforcement by normalizing the composite property by its base polymer property. Nanocomposite no. 8 is a nanocomposite with gold nanoparticles as nanofillers, which is the main focus of this thesis. A best combination of stiffness, strength and strain to failure is achieved in nanocomposite no. 8 by combining gold nanoparticles with aramid-based matrix. Figure 2.4 further compares those nanocomposites by plotting those properties.

		Filler Amount		Absolute Value of Composites			Normalized Value over Polymers		
No	Nanocomposites	wt%	vol%	Stiffness (GPa)	Strength (MPa)	Strain at Failure (%)	Stiffness	Strength	Strain at Failure
1	**CNT-GNS/Epoxy** [5]	0.5	-	3.0	68	4.8	1.40	1.36	0.998
2	**ANF-GNS/PMMA**[16]	0.7	-	3.4	63	4.1	1.71	1.85	1.24
3	**CNT/PVA** [13]	0.8	0.63	4.3	107	40	1.79	1.47	0.65
4	**CNT/Epoxy** [12]	1.0	-	1.6	58	5.2	1.17	1.21	1.24
5	**GNS/PMMA** [24]	1.0	-	3.8	84	-	1.80	1.20	-
6	**SWNT/Nylon 6** [5]	1.5	-	1.2	75	120	0.75	0.9	0.29
7	**CNT/PU** [25]	-	2.5	0.1	19	-	2.71	4.70	-
8	**AuNP/Aramid**	**6**	**-**	**9.3**	**283**	**11**	**1.31**	**2.45**	**1.34**
9	**MTM/PU** [1]	41	26	3.6	34	0.8	144	2.59	0.001
10	**PEI/WMNT** [14]	50	-	4.5	150	0.03	1.13	16.67	0.01
11	**$((PEI/PAA)(PEI/SWNT)_5)_8$** [15]	50	-	35	220	1.0	8.75	24.44	0.24
12	**MTM/PVA** [6]	70	50	106	400	0.33	62.35	10.00	0.01

Table 2.1 The mechanical properties of various nanofiller reinforced polymer nanocomposites.

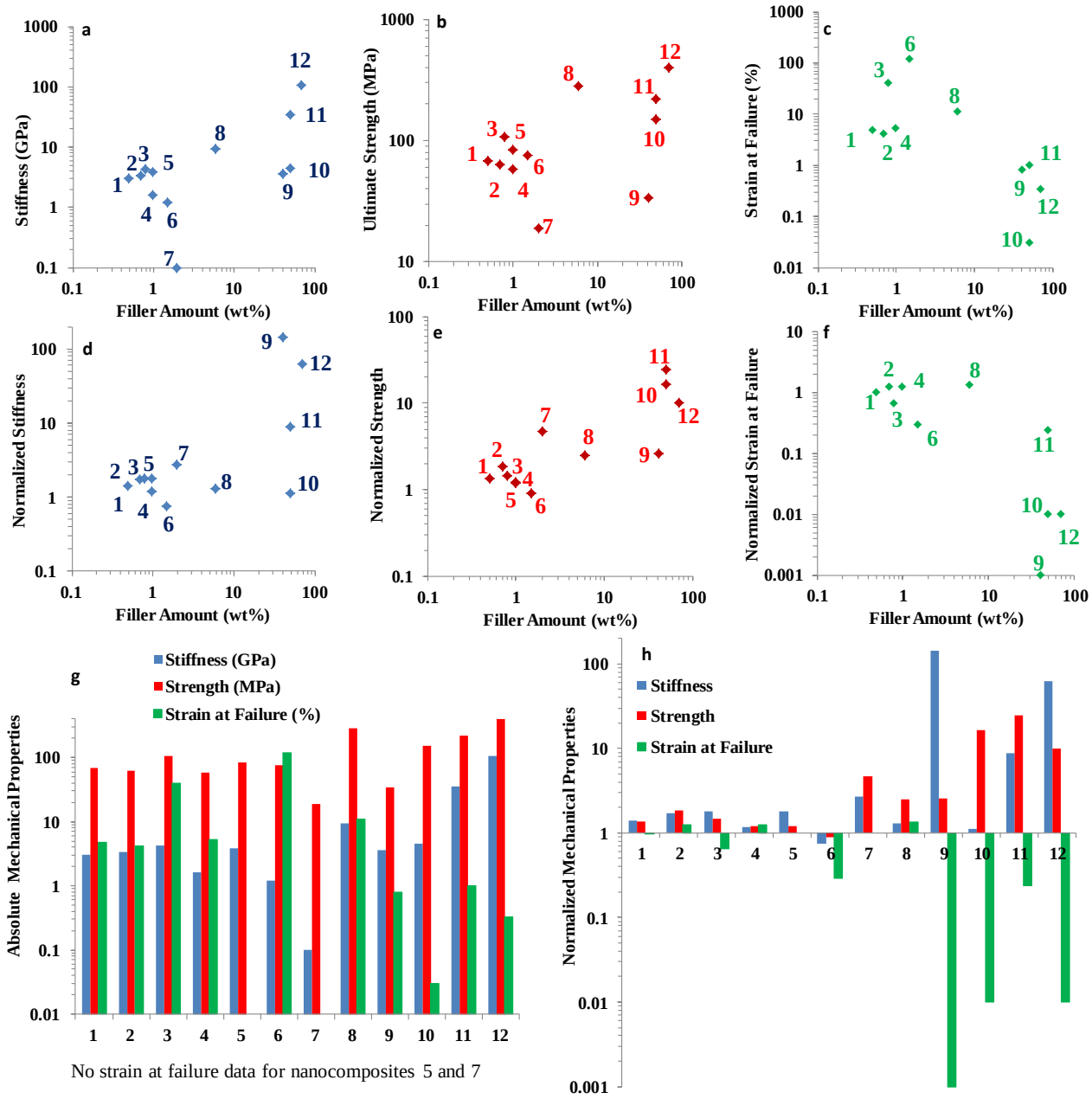

Figure 2.4 The mechanical properties and normalized mechanical properties of various nanocomposites with nanofillers embedded in different polymer matrices. The magtinudes of a) stiffness b) ultimate strength and c) strain to failure of the nanocomposites with respect to nanofiller weight fraction. The normalized values of a) stiffness b) ultimate strength and c) strain to failure of the nanocomposites with respect to nanofiller weight fraction.

For a low content of nanofillers, proper functionalization is the key for obtaining effective reinforcement effect, whereas at higher contents, the difficulty in achieving better reinforcement effect is caused by the nanofiller aggregation. When the amount of the nanofillers is small, as in nanocomposites no. 1-7, properly functionalized nanofillers enhance both the stiffness and strength of the nanocomposites, as shown in Table 2.1 and Figure 2.4. The strain to failure, however, usually decreases owing to the addition of the nanofillers. The nanocomposites with ultra-high nanofiller content are prepared by a layer-by-layer assembly method to eliminate the aggregation problems. Increases of the stiffness and strength can reach more than 10 fold with a large amount of nanofillers. The stiffness of the PVA/MTM nanocomposite (no.12) reaches the theoretical maximum of combining the two constituents, indicating excellent bonding and dispersion of the nanofillers [6]. However, these nanocomposites (no. 9-12) with ultra-high content of nanofillers all have very low strain to failure. Most of them eliminate the ductility of the polymers by 100%, and the brittleness of the materials can limit their application significantly.

2.2 Aromatic Polyamides and Aramid Fibers

As much of the recent work on nanocomposite mechanics has been focused on improving the reinforcement phase (e.g. dispersion of nanofillers) [12, 25-27], a lack of effort on the polymeric matrix exists in the development of nanocomposites. Polymeric matrices with superior mechanical properties and versatile techniques to tailor these matrices are also required in order to obtain advanced nanocomposites. Suitable polymeric nanoscale building blocks for advanced composite matrices can be prepared from conventionally strong materials. Poly-paraphenylene terephthalamide (PPTA), a high performance para-aramid polymer better known by its trade-name Kevlar, has exceptional stiffness and strength, and serves as a promising candidate for such a matrix material. Kevlar belongs to the class of high-performance polymers used as the reinforcing fibers in structural components of aircrafts and high-functionality boats [28]. The high stiffness and tensile strength of Kevlar, as well as its

durability and low density, make it an alternative to metal and nylon as a bulletproof material in ballistic products [28]. The Kevlar fibers consist of long molecular chains oriented parallel to each other. Each Kevlar molecular chain can have from one to five million monomers bonded together. This high alignment of the molecular chains results in anisotropic Kevlar fibers with high stiffness and strength only along the fiber axis [29, 30], as shown in Figure 2.5. The mechanical properties of Kevlar fiber are shown in Table 2.2.

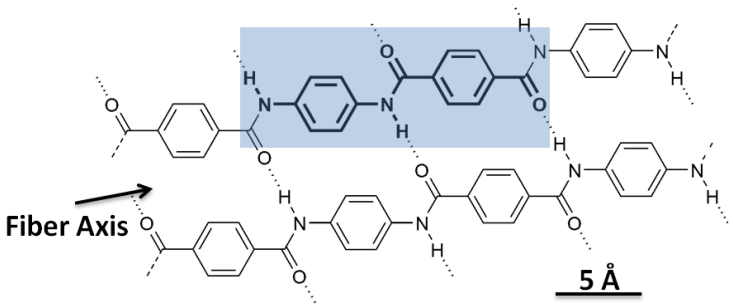

Figure 2.5 Chemical structure of Kevlar fiber. The parallel-oriented molecules of the fiber as a crystalline structure contribute to its anisotropy and high stiffness and strength only along the fiber axis. The bold part indicates the aramid monomer that has an amide linkage bonded between two aromatic rings [31].

Mechanical Properties	**Kevlar KM2 fiber** [29]
Tensile Strength (GPa)	4.9
Tensile Modulus (GPa)	85
Strain at Failure (%)	4.5

Table 2.2 The mechanical properties of Kevlar fiber along the fiber axis.

Since its initial development, the application of Kevlar has been primarily limited to fiber reinforcement in a polymer matrix and woven fiber mats, and the useful mechanical properties of Kevlar are realized only along the fiber axes [32-34]. Relying on the superior mechanical properties, aramid microfibers have been used to reinforce high-ductility, low-stiffness polymers, to raise the stiffness and yield strength of polymer matrix composites while preserving toughness [34-36]. However, this approach using Kevlar microfibers has been hindered by the lack of an effective way to promote or improve the adhesion between aramid fibers and polymer matrices. The same problem of weak adhesion between aramid fibers and inorganic nanoscale components such as carbon nanotubes has also limited their use in nanocomposites [37].

The paradigm of aramid microfibers as relatively inert and possessing a low affinity for surface bonding has long been recognized. This has motivated many efforts to develop techniques such as hydrolysis or surface coating to enhance the interaction between Kevlar and other materials [34-36, 38-42]. The surface of an aramid microfiber contains a limited number of reactive sites to bond with other materials [43, 44], and the core is an inert region consisting of closely packed macromolecular chains with a high density of hydrogen bonds between them. The low surface to volume ratio of a microfiber results in chemically stable fibers and yarns as shown in Figure 2.8. Kevlar fibers are also widely used as gloves as they are inherently flame-resistant, so they won't burn, melt, or support combustion. Figure 2.9 shows a thermogravimetric analysis of Kevlar and the fiber is thermally stable up to ~ 550 $^{\circ}$C.

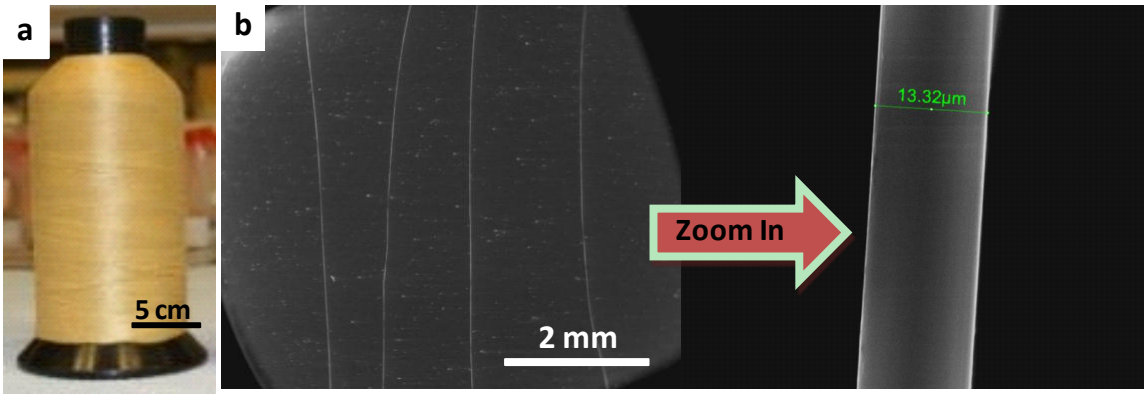

Figure 2.6 a) Commercial Kevlar yarns used as fiber reinforcement or woven into mats. b) Aramid microfibers with diameters of around 14 µm separated from commercial Kevlar yarns and observed in an SEM [31].

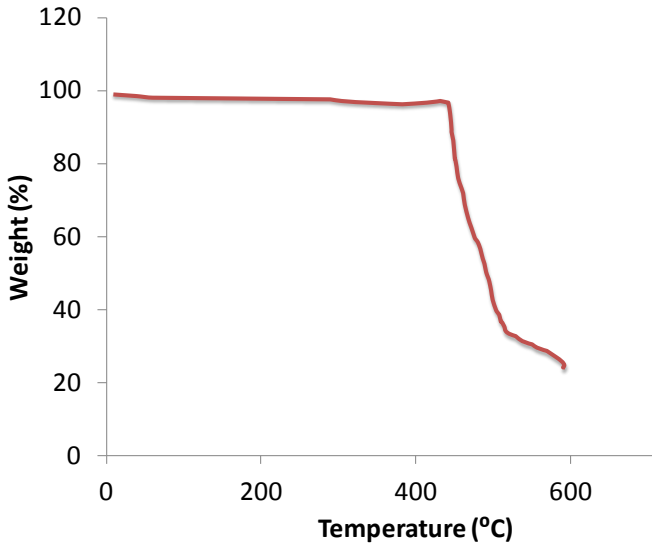

Figure 2.7 Thermogravimetric analysis of Kevlar 49 in air at a temperature rise of 10 °C/min. Figure reproduced from a document in the public domain, "Technical Guide Aramid Fiber - DuPont". Downloaded from <http://www2.dupont.com/Superfibers_Contest/cs_CZ/assets/downloads/Technicke%20soubsou/Technical%20Guide%20for%20KEVLAR%C2%AE.pdf> on May 8 2013.

2.2 Gold Nanoparticles

Gold nanoparticles (AuNPs) are the stablest metal nanoparticles with size-related electronic, magnetic and optical properties (quantum size effect) [45]. They have been widely used as catalysts and for biological applications [45]. AuNPs however, haven't been used as nanofillers to reinforce the mechanical properties of polymers. AuNPs can be prepared using different reduction methods. One particular method, reducing gold by sodium citrate from chloroauric acid ($HAuCl_4$) in water, is an easy and effective way to generate stable monodispersions of AuNPs with controlled particle sizes [46]. As sodium citrate reduces gold from Au^{3+} in gold chloride to gold atoms and those atoms then nucleate into AuNPs, the concentration of the citrate determines the amount of gold atoms reduced and thus it determines the final nanoparticle sizes. A larger citrate concentration yields a smaller AuNP size, as more citrate molecules attach to the surfaces of the AuNPs, preventing further nucleation of the AuNPs. A desired AuNP size thus can be prepared by using a certain gold chloride to sodium citrate ratio during AuNP synthesis. The monodispersion of gold nanoparticles with certain sizes, are controlled by the ratio of Solution I and Solution II used during the particle preparations [46]. Solution I is the gold chloride solution ($HAuCl_4$, 10^{-2} wt%) and Solution II is the sodium citrate solution (Na_3-citrate, 1wt%). The color of the gold nanoparticles changes from red to violet with the increase of the particle sizes (quantum size effect).

Gold nanoparticles are also well known for their strong interactions with visible light. The collective oscillations of the conduction electrons within the particles excited by light can create strong near-field electromagnetic fields and far-field propagating waves that enhance the light absorption and photocurrent of organic photovoltaic devices [47]. This strong interaction also makes the analysis of AuNPs possible by probing them using light. Ultraviolet–visible (UV-vis) spectroscopy is widely used to probe the shape and the density of AuNPs as well as their interaction with polymers, as UV-vis spectroscopy measures the absorption or reflectance spectroscopy in the ultraviolet-visible spectral region. The shape changes of the AuNPs from nanorods to isotropic nanodots is reflected in the shape of the

UV–vis spectrum, in which a single plasmon band centered near 530 nm is present from the isotropic “dot” shape compared with the two distinct plasmon bands in the spectrum from the anisotropic nanorod shapes [47]. The broadening and red-shift of absorption spectra are mainly caused by a reduced nanoparticle-nanoparticle distance and a change in the refractive index as a result of the polystyrene sulfonate (PSS) adsorbed onto the functionalized AuNPs (DMAP-AuNP). This suggests electrostatic interaction between the DMAP-AuNP and PSS [48].

2.4 Purpose and Research Overview

As a study of the biomaterial nacre revealed the mechanism behind the enhanced toughness obtained from brittle constituents, we are fascinated by nacre’s ‘brick-and-mortar’ architecture, which combines stiff particles with polymer layers. Synthetic nanocomposites have been designed with this paradigm of embedding stiff and strong nanofillers such as MTM clay particles, carbon nanotubes and graphene nanosheets in various polymer matrices. And the recent work on nanocomposite mechanics has been focused on improving attributes of these reinforcement phases. Polymeric matrices with superior mechanical properties and versatile techniques to tailor these matrices are also needed to achieve advanced nanocomposites. Suitable polymeric nanoscale building blocks for advanced composite matrices can be prepared from conventionally strong materials. Kevlar with its exceptional stiffness and strength serves as a promising candidate for such a matrix material. In this work, we will start with the focus on the aramid polymer, as its excellent mechanical properties make it an ideal candidate for a polymer matrix, to show how nanoscale aramid building blocks can offer advantageous features over the macroscopic Kevlar fibers and many other polymers. Through certain chemical treatments and assembly methods, the nanostructure, and the morphology as well as the resulting mechanical and thermal properties of aramid nanostructured networks can be tailored. Based on this aramid network with great mechanical

and thermal properties, gold nanoparticles are chosen as the nanofiller to further enhance the nanocomposite properties. Enhancement of stiffness, strength and strain to failure are achieved at the same time by embedding AuNPs in aramid nanostructured networks, and a nanocomposite with an optimal combination of stiffness, strength and strain to failure is created with great potentials as an impact-resisting material.

Reference

[1] A. K. Kaushik , P. Podsiadlo, M. Qin, C. M. Shaw, A. M. Waas, N. A. Kotov, E. M. Arruda, "The Role of Nanoparticle Layer Separation in the Finite Deformation Response of Layered Polyurethane-Clay Nanocomposites," *Macromolecules* **2009**, Vol. 42, pp. 6588-6595.

[2] M. Schiek, F. Balzer, K. Al-Shamery, J. R. Brewer, A. Lutzen and H.-G. Rubahn, "Organic Molecular Nanotechnology," *Small* **2008**, Vol. 4, No.2, pp. 176-181.

[3] M. Zhang, L. Su and L. Mao, "Surfactant functionalization of carbon nanotubes (CNTs) for layer-by-layer assembling of CNT multi-layer films and fabrication of gold nanoparticle/CNT nanohybrid," *Carbon* **2006**, Vol. 44, pp.276-283.

[4] T. Vossmeyer, B. Guse, I. Besnard, T. E. Bauer, K. Mullen and A. Yasuda, "Gold Nanoparticle/Polyphenylene Dendrimer Composite Films: Preparation and Vapor-Sensing Properties," *Adv. Mater.* **2002**, Vol. 14, No.3, pp. 238-242.

[5] W. Li, A. Dichiara and J. Bai, "Carbon nanotube-grphene nanoplatelet hydrids as high-performance multifunctional reinforcements in epoxy composites," *Compos. Sci. Technol.* **2013**, Vol. 74, pp. 221-227.

[6] P. Podsiadlo, A. K. Kaushik, E. M. Arruda, A. M. Waas, B. S. Shim, J. Xu, H. Nandivada, B. G. Pumplin, J. Lahann, A. Ramamoorthy, N. A. Kotov, "Ultrastrong and Stiff Layered Polymer Nanocomposite," *Science* **2007**, Vol. 318, pp. 80-83.

[7] G. M. Luz and J. F. Mano, "Biomimetic design of materials and biomaterials inspired by the structure of nacre," *Phil. Trans. R. Soc. A* **2009**, Vol. 367, pp. 1587–1605.

[8] B. L. Smith, T. E. Schäffer, M. Viani, J. B. Thompson, N. A. Frederick, J. Kindt, A. Belcher, G. D. Stuckyk, D. E. Morse and P. K. Hansma, "Molecular mechanistic origin of the toughness of natural adhesives, fibers and composites," *Nature* **1999**, Vol. 399, pp. 761-763.

[9] F. Barthelat, C. M. Li, C. Comi and H. D. Espinosa, "Mechanical properties of nacre constituents and their impact on mechanical performance," *J. Mater. Res.* **2006**, Vol. 21, No. 8, pp. 1977-1986.

[10] E. Munch, M. E. Launey, D. H. Alsem, E. Saiz, A. P. Tomsia and R. O Ritchie, "Tough, Bio-inspired Hybrid Materials," *Science* **2008**, Vol. 322, pp. 1516-1520.

[11] J. Gao, M. Itkis, A. Yu, E. Bekyarova, B. Zhao and R. C. Haddon, "Continuous Spinnning of a Single-Walled Carbon Nanotube-Nylon Composite Fiber", *J. AM. CHEM. SOC.* **2005**, Vol. 127, pp. 3847-3854.

[12] J. A. Kim, D. G. Seong, T. J. Kang and J. R. Youn, "Effects of surface modification on rheological and mechanical properties of CNT/epoxy composites," *Carbon* **2006**, Vol. 44, pp. 1898–1905.

[13] L. Liu, A. H. Barber, S. Nuriel and H. D. Wagner, "Mechanical Properties of Functionalized SingleCarbon-Nanotube/Poly(vinyl alcohol) Nanocomposites," *Adv. Funct. Mater* **2005**, Vol. 15, pp. 975-980.

[14] M. Olek, J. Ostrander, S. Jurga, H. Mohwald, N. A. Kotov, K. Kempa and M. Giersig, "Layer-by-Layer Assembled Composites from Multiwall Carbon Nanotubes with Different Morphologies", *Nano Lett.* **2004**, Vol. 4, No. 10, pp. 1889-1895.

[15] A. A. Mamedov, N. A. Kotov, M. Prato, D. M. Guldi, J. P. Wicksted and A. Hirsch, "Molecular design of strong single-wall carbon nanotube/polyelectrolyte multilayer composites," *Nat. Mater.* **2002**, Vol. 1, pp. 190-194.

[16] J. Fan, Z. Shi, L. Zhang, J. Wang and J. Yin, "Aramid nanofiber-functionalized graphene nanosheets for polymer reinforcement," *Nanoscale* **2012**, Vol. 4, pp. 7046–7055.

[17] S. Iijima, "Helical microtubules of graphitic carbon", *Nature* **1991**, Vol. 354, pp. 56-58.

[18] J. K. Holt, H. G. Park, Y. Wang, M. Stadermann, A. B. Artyukhin, C. P. Grigoropoulos, A. Noy, O. Bakajin,"Fast Mass Transport Through Sub-2- Nanometer Carbon Nanotubes," *Science* **2006**, Vol. 312, pp. 1034-1037.

[19] F. Fornasiero, H. G. Park, J. K. Holt, M. Stadermann, C. P. Grigoropoulos, A. Noy, O. Bakajin, "Ion exclusion by sub-2-nm carbon nanotube pores," *PNAS* **2008**, pp. 1-6.

[20] Kaushik, Amit. "Deformation Mechanisms in Polymer-Clay Nanocomposites," Thesis. *University of Michigan* **2010**.

[21] A. C. Balazs, T.E. and T. P. Russell, "Nanoparticle Polymer Composites: Where Two Small Worlds Meet," *Science* **2006**, Vol. 314, pp. 1107-1110.

[22] I. O'Connor, H. Hayden, J. N. Coleman, Y. K. Gun'ko, "High-Strength, High-Toughness Composites Fibers by Swelling Kevlar in Nanotube Suspensions," *Small* **2009**, Vol. 5, No. 4, pp. 466-469.

[23] Z. Spitalskya, D. Tasisb, K. Papagelis and C.Galiotis, "Carbon nanotube–polymer composites: Chemistry, processing, mechanical and electrical properties," *Prog. Polym. Sci.* **2010**, Vol. 35, pp. 357–401.

[24] T. Ramanathan, A. A. Abdala, S. Stankovich, D. A. Dikin, M. Herrera-Alonso, R. D. Piner, D. H. Adamson, H. C. Schniepp, X. Chen, R. S. Ruoff, S. T. Nguyen, I. A. Aksay, R. K. Prud'homme, L. C. Brinson, "Functionalized graphene sheets for polymer nanocomposites", *Nat. Nanotechnol.* **2008**, Vol. 3, pp. 327-331.

[25] H. C. Kuan, C. M. Ma, W. P. Chang, S. M. Yuen, H. H. Wu, T. M. Lee, "Synthesis, thermal, mechanical and rheological properties of multiwall carbon nanotube/waterborne polyurethane nanocomposite," *Compos. Sci. Technol.* **2005**, Vol. 65, pp. 1703–1710.

[26] X. Zhao, Q. Zhang, D. Chen, P. Lu, "Enhanced mechanical properties of graphene-based poly (vinyl alcohol) composites," *Macromolecules* **2010**, Vol. 43, pp. 2357–2363.

[27] M. A. Rafiee, J. Rafiee, Z. Wang, H. Song, Z. Yu, N. Koratkar, "Enhanced mechanical properties of nanocomposites at low graphene content, " *ACS Nano* **2009**,Vol. 3, No. 12, pp. 3884-3890.

[28] "Processing Kevlar Aramid Fiber." *Bulletin No. LM-226*. Inc., Litterford Bors.. Web. 12 May 2013. <www.littleford.com/images/09_brochures/MEDIUM/Processing_Kevlar_Aramid_Fiber.pdf>.

[29**]** M. Cheng, W. Chen, T. Weerasooriya, "Mechanical Properties of Kevlar KM2 Single Fiber," *J. Eng. Mater. Technol.* **2005**, Vol. 127, pp. 197-203.

[30**]** H. H. Yang, "Kevlar Aramid Fiber," *Chichester J. Wiley* **1993**, Print.

[31] K. Cao, C. Pons Siepermann, M. Yang, A. M. Waas, N. A. Kotov, M. D. Thouless, and E. M. Arruda, "Reactive Aramid Nanostructures as High-Performance Polymeric Building Blocks for Advanced Composites," *Adv. Funct. Mater.* **2013**, Vol. 23, pp. 2072–2080.

[32] J. Kalantar and L. T. Drzal, "The bonding mechanism of aramid fibers to epoxy matrices*," J. Mater. Sci.* **1990**, Vol. 25, pp. 4186-4193.

[33**]** S. K. N. Kutty and C. B. Nando, "Short Kevlar Fiber-Thermoplastic Polyurethane Compostie," *J. Appl. Polym. Sci.* **1991**, Vol. 43, pp. 1913-1923.

[34**]** S. Saikrasun, T. Amornsakchai, C. Sirisinha, W. Meesiri, S. Bualek-Limcharoe, "Kevlar reinforcement of polyolefin-based thermoplastic elastomer," *Polymer* **1999**, Vol. 40, pp. 6437-6442.

[35] T. K. Lin, S. J. Wu, J. G. Lai, S. S. Shyu, "The Effect of Chemical Treatment on Reinforcement/Matrix Interaction in Kevlar-fiber/Bismaleimide Composites," *Compos. Sci. Technol.* **2000**, Vol. 60, pp. 1873-1878.

[36] F. Guo, Z. Zhang, W. Liu, F. Su, H. Zhang, "Effect of Plasma Treatment of Kevlar Fabric on the Tribological Behavior of Kevlar Fabric/Phenolic Composites," *Tribol. Int.* **2009**, Vol. 42, pp. 243-249.

[37] F. H. Gojny, J. Nastalczyk, Z. Roslaniec, K. Schulte, "Surface modified multi-walled carbon nanotubes in CNT/epoxy-composites," *Chem. Phys. Lett.* **2003**, Vol. 370, pp. 820–824.

[38] Z. Yu, A. Ait-Kadi, J. Brisson, "Nylon/Kevlar Composites. I: Mechanical Properties," *Polym. Eng. Sci.* **1991**, Vol. 31, No. 16.

[39] G. Li, C. Zhang, Y. Wang, P. Li, Y. Yu, X. Jia, H. Liu, X. Yang, Z. Xue, S. Ryu, "Interface Correlation and Toughness Matching of Phosphoric Acid Functionalized Kevlar Fiber and Epoxy Matrix for Filament Winding Composites," *Compos. Sci. Technol.* **2008**, Vol. 68, pp. 3208-3214.

[40] S. Park, M. Seo, T. Ma, D. Lee, "Effect of Chemical Treatment of Kevlar Fibers on Mechanical Interfacial Properties of Composites," *J. Colloid Interface Sci.* **2002**, Vol. 252, pp. 249-255.

[41] M. Rajabian, C. Dubois, "Polymerization Compounding of HDPE/Kevlar Composites. I. Morphology and Mechanical Properties," *Polym. Compos.* **2006**, Vol. 27, Issue 2, pp. 129-137.

[42] A. Mathur, N. Netravali, "Modification of mechanical properties of Kevlar fibre by polymer infiltration," *J. Mater. Sci.* **1996**, Vol. 31, pp. 1265-1274.

[43] W. Sweeny, "Improvements in Compressive Properties of High Modulus Fibers by Crosslinking," *J. Polym. Sci., Part A: Polym. Chem.* ***1992***, Vol. 30, pp. 1111-1122.

[44] J. W. Downing, Jr., J. A. Newell, "Characterization of Structural Changes in Thermally Enhanced Kevlar-29 Fiber," *J. Appl. Polym. Sci.* **2004**, Vol. 91, pp. 417-424.

[45] M.-C. Daniel and D. Astruc, "Gold Nanoparticles: Assembly, Supramolecular Chemistry, Quantum-Size-Related Properties, and Applications toward Biology, Catalysis, and Nanotechnology", *Chem. Rev.* **2004**, Vol. 104, pp. 293-346.

[46] G. Frens, "Controlled Nucleation for the Regulation of the Particle Size in Monodisperse Gold Suspensions', *Nat. Phys. Sci.* **1973**, Vol. 241, pp. 20-22.

[47] J. H. Lee, J. H. Park, J. S. Kim, D. Y. Lee and K. Cho, "High efficiency polymer solar cells with wet deposited plasmonic gold nanodots," *Org. Electron.* **2009**, Vol. 10, pp. 416-420.

[48] J. Cho and F. Caruso, "Investigation of the Interactions between Ligand-Stabilized Gold Nanoparticles and Polyelectrolyte Multilayer Films," *Chem. Master*. **2005**, Vol. 17, pp. 4547-4553.

Chapter 3

Experimental Details

3.1 Synthesis

3.1.1 Dispersion of Aramid Nanofibers

A nano-scale dispersion of Kevlar fibers was achieved via a reaction of potassium hydroxide (KOH) with Kevlar in a dimethyl sulfoxide (DMSO) solution. Kevlar 49 fibers (1.5 g, from Thread Exchange Inc.) were soaked in 1-methyl-2-pyrrolidinone (NMP) (anhydrous, 99.5%, Sigma-Aldrich) and sonicated for two days to swell and disperse the Kevlar fibers and provide dissolution [1]. After sonication, the Kevlar fibers were washed with de-ionized water and completely dried. The NMP-sonicated Kevlar fibers were then mixed with potassium hydroxide KOH (1.5 g, 99.9% Semiconductor Grade, Sigma Aldrich) in 0.5 L of DMSO (99.9%, Sigma Aldrich). The mixture was stirred vigorously at room temperature for seven to nine days until the solution turned viscous and dark red, indicating the Kevlar fibers were fully dissolved. A similar preparation of Kevlar nanofibers without NMP sonication was shown to result in diameters of 3 to 30 nm and lengths on the order of 10 μm [2]. Figure 3.1 shows various stages of this aramid nanofiber (ANF) synthesis process.

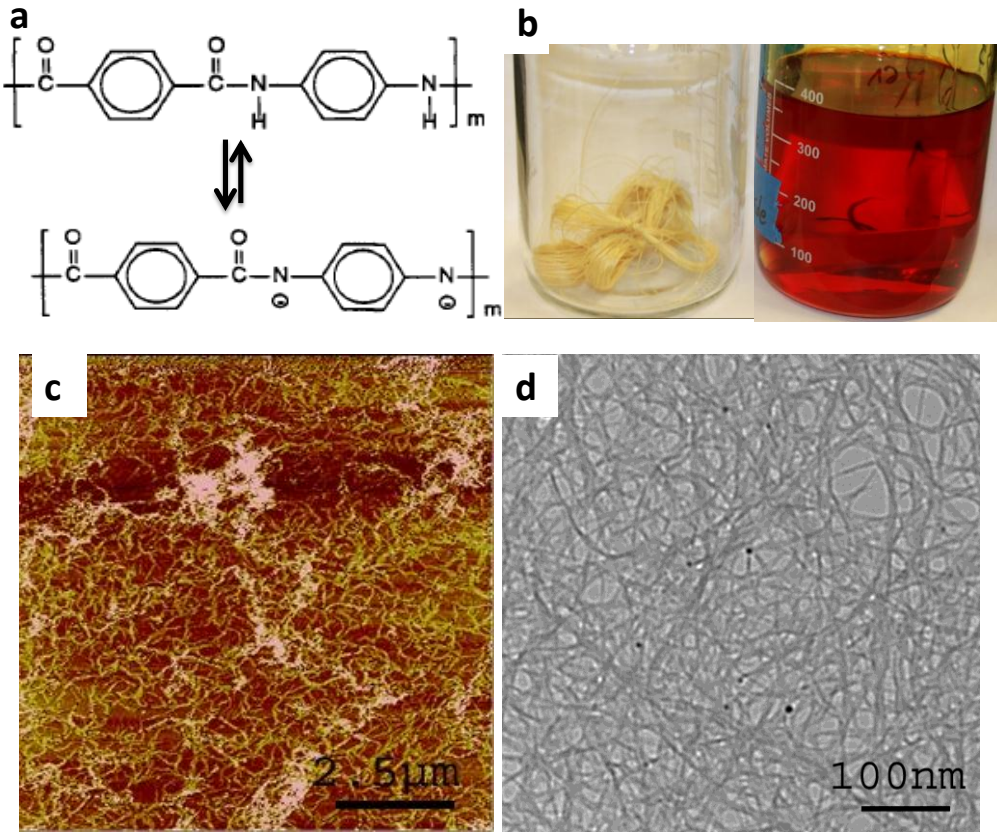

Figure 3.1 a) The dissolution of Kevlar fiber by KOH owing to partial destruction of hydrogen bonding between molecular chains [2, 3]. b) Left: commercial Kevlar fibers vs. dissolved Kevlar fiber in DMSO solution through the process in a). c) Atomic force microscopy (AFM) and d) transmission electron microscopy (TEM) images of Kevlar fiber dispersed in DMSO KOH solution and deposited on a substrate. Figures in c) and d) are reproduced from Yang et al., 2011 [2].

3.1.2 Synthesis of Aramid Nanofiber Networks

Two methods, layer-by-layer assembly and vacuum-assisted filtration, were used to prepare ANF networks from this Kevlar/DMSO solution. Both methods produced ANF networks in the form of thin films. The typical thickness of the ANF networks was on the order of 10 μm.

Layer-by-Layer Assembly

Layer-by-layer (LBL) assembly has been shown to be an effective method for assembling molecules in a highly ordered fashion to synthesize nanocomposites with enhanced mechanical properties [4-6**]**. This assembly process deposites oppositely charged macromolecules on a substrate in a layer-by-layer fashion. Owing to the interaction between the polyelectrolyte chains, spontaneous ordering of the macromolecules in the solution can be achieved through the alignment of molecules to maximize the attractive energy with the surface. This results in a highly ordered structure through a self-organizing mechanism during fabrication [5-7]. The dense bonding between the interfaces leads to better load transfer between the layers and enhancement of the mechanical properties compared to composites prepared by blending and casting [6]. The process of depositing one layer of ANF is as follows: A glass slide was used as a substrate and was coated with poly (diallyldimethylamonium chloride) (PDDA) by dipping in a PDDA solution (1% aqueous solution) for one minute to create a positively charged layer for the subsequent deposition of ANFs. The PDDA coated glass slide was then dipped in the Kevlar/DMSO solution for one minute. After a layer of ANF was deposited, the glass substrate was rinsed in de-ionized water and dried by compressed air. The ANFs were deposited on each layer due to the aromatic stacking interactions and hydrogen bonding between them. An ANF LBL film was made after hundreds of layers were deposited as shown in Figures 3.2 and 3.3.

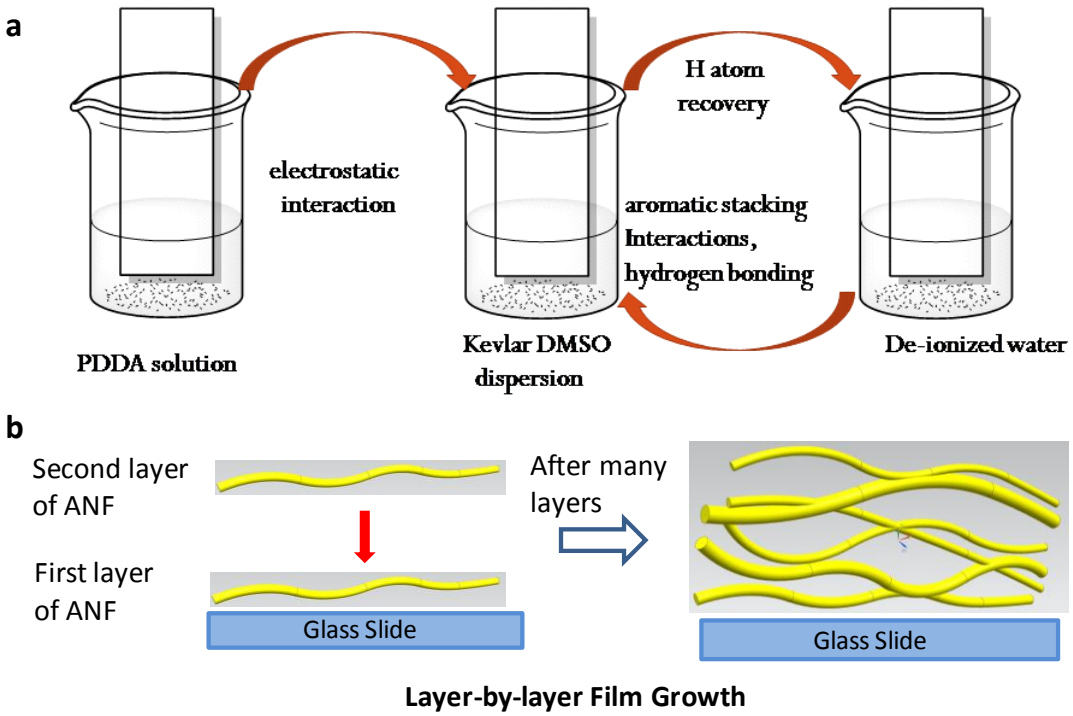

Figure 3.2 a) The layer-by-layer process of depositing the first layer of ANFs. b) An ANF LBL film was made by depositing ANFs layer by layer until a certain thickness was achieved.

Figure 3.3 An ANF film made by layer-by-layer assembly showing uniformity and transparency.

The traditional LBL process was automated via a StratoSequence VI machine, (NanoStrata Inc. Tallahassee, FL). The difficulties of the new LBL process using non-water-soluble constituents stem from the water-sensitivity of the Kevlar/DMSO solution. With the addition of a small amount of water, as is present in the humid environment of the StratoSequence VI, the ANFs precipitate owing to the restoration of hydrogen bonding which deteriorates the Kevlar/DMSO solution. A lid-opening robot was designed and built to shield the Kevlar/DMSO solution during the fabrication process, which automated the fabrication process via the NanoStrata apparatus again. The design of the robot is shown in Figure 3.4.

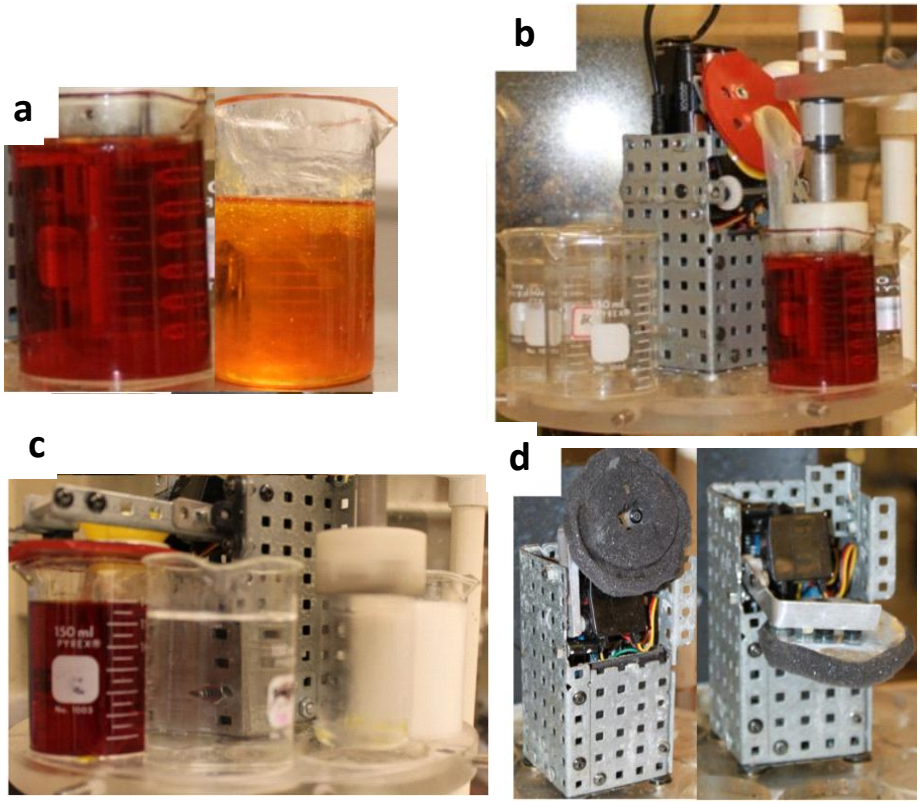

Figure 3.4 a): Kevlar/DMSO solution (left) vs. deteriorated solution with precipitates floating in the solution owing to a humid environment. The automated fabrication process: b) the lid opens during the ANF deposition step and c) the lid stays closed during other steps to shield the solution. d) The lid-opening robot: (left) open-lid vs. (right) closed-lid state.

Vacuum-Assisted Filtration

An ANF network was also prepared using a filtration method, by slowly adding water droplets in the Kevlar/DMSO solution at room temperature while stirring, until precipitation of protonated nanofibers was forced owing to the donation of hydrogen by water [2]. The resulting suspension was filtered using a hydraulic-powered pressure differential connected to a filtration flask, as shown in Figure 3.5. After pouring the products onto filter paper in a Büchner funnel, which was secured by a rubber bung on the top of the flask, a constant flow of water was used to create a pressure differential in the flask for 10-15 minutes until all the liquid was filtered through the paper. To remove any residually absorbed solvent, the recovered solid on the filter paper was placed in a 338 K oven for 24 hours. After this drying process, a homogeneous film resulted that could easily be separated from the filter paper using a razor blade, as shown in Figure 3.6a.

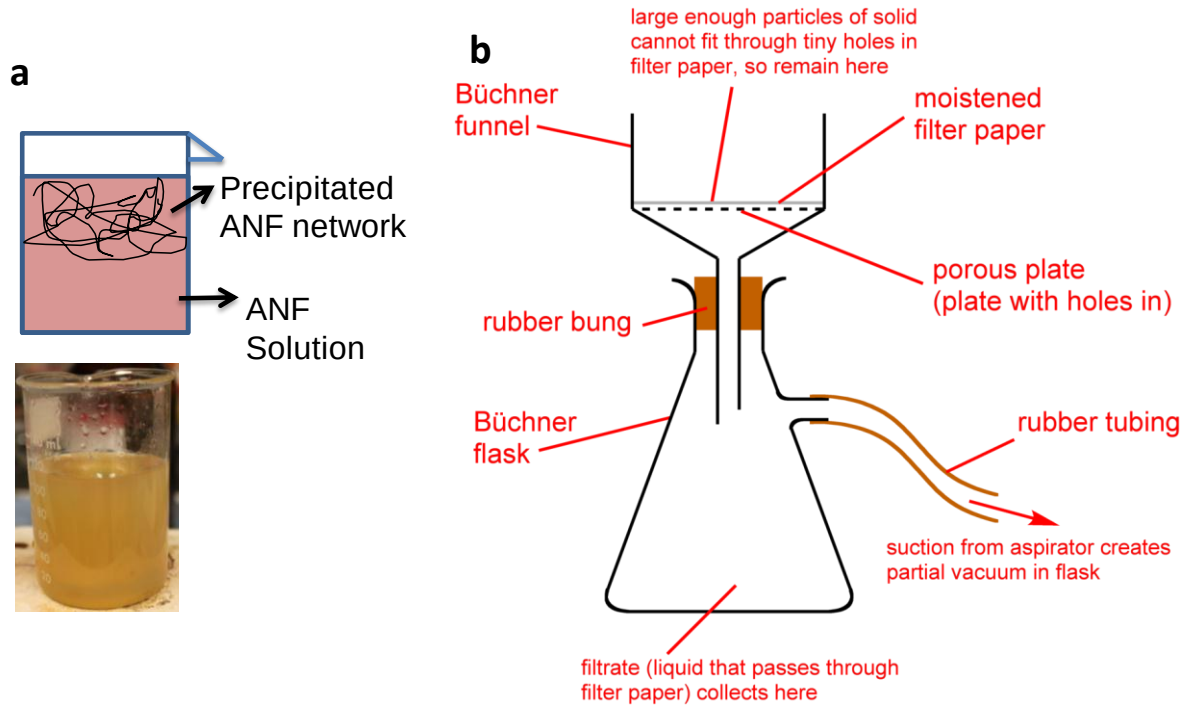

Figure 3.5 a) With the addition of water in the Kevlar/DMSO solution, the ANF network was formed by restored hydrogen bonding and the resulting suspension was filtered. b) The vacuum-assisted filtration system used to filter the solid. Image in the public domain. Downloaded from http://commons.wikimedia.org/wiki/File:Vacuum-filtration-diagram.png on May 8 2013.

3.1.3 Synthesis of Phosphoric Acid/Glutaraldehyde-Treated Aramid Nanostructured Networks

Layer-by-Layer Assembly

PA/GA-treated Kevlar LBL films were made by first coating a glass slide with poly (diallyldimethylamonium chloride) (PDDA) by dipping in 1% PDDA solution for one minute. This first layer of PDDA was necessary for the initiation of Kevlar layer growth since the positively charged PDDA provides an electrostatic attraction to the negatively charged nanofibers. The slide was then immersed in a Kevlar/DMSO solution (of section 3.1.1) for two minutes, followed by immersion in 10 wt% phosphoric acid (PA) (85 wt% in water, Sigma Aldrich) in de-ionized water and 10 wt% glutaraldehyde (GA) (50% in water, Fisher BioReagents) in de-ionized water for one minute respectively. This process deposited a monolayer of PA/GA-treated ANFs on the substrate. The slide was rinsed in de-ionized water for one minute to remove loosely attached nanofibers as well as excess PA and GA, and then dried by compressed air. The process was repeated beginning with dipping in the Kevlar/DMSO solution until the desired film thickness is achieved. The PA/GA treated Kevlar LBL film is also transparent. The process of making PA/GA-treated Kevlar LBL films was also automated via the StratoSequence VI machine (NanoStrata Inc.), which was modified by implementing a custom-designed and built robot for using the water-sensitive Kevlar/DMSO solution, as discussed in section 3.1.2.

Vacuum-Assisted Filtration

Acidic hydrolysis of ANFs. The acidic hydrolysis of ANFs was achieved by mixing the Kevlar/KOH/DMSO solution with PA (85 wt% in water, Sigma Aldrich) and de-ionized water (5 mL) to promote hydrolysis. The amount of acid used, from 0.25 to 2.5 mL for 100 mg Kevlar fiber, was varied to control the extent of reaction. The mixture was heated to 373 K and vigorously stirred for 5 hours. The temperature was carefully monitored and held below 383 K, the temperature at which DMSO may combust, but above 363 K, to induce hydrolysis of the amides on the aramid backbone molecules. The color of the hydrolyzed Kevlar solution depended upon the amount of acid; in general it was a clear, light-yellow liquid.

Condensation of hydrolyzed aramid nanostructures with GA. Upon completion of the hydrolysis reaction**,** GA (50% in water, Fisher BioReagents) was added to the hydrolyzed Kevlar/KOH/DMSO solution as a crosslinking agent after the hydrolysis reaction was complete. The amount of GA used, from 1.5 to 3 mL, was varied to alter the extent of reaction. The mixture was stirred at 373 K for three to four days. Condensation progression was monitored from the color of the mixture, which darkened and became cloudier with increased processing. The process was assumed to be complete when the color stabilized.

Vacuum-assisted filtration of the reacted product. The resulting suspension was filtered the same way as the ANF network shown in Figure 3.5. The color of the resulting film on the filter paper ranged from yellow to brown, depending on the extent of the reaction. A transparent-brown solution was recovered from the filtered solvent. Both the solid and liquid products were kept for subsequent analysis. The recovered solid on the filter paper was placed in a 338 K oven for 24 hours. After this drying process, a homogeneous film resulted, which could easily be separated from the filter paper using a razor blade.

3.1.4 Synthesis of Aramid Nanostructured Networks with Gold Nanoparticles

Citrate-based condensations and gold complexation. Upon completion of the same hydrolysis reaction discussed in section 3.1.3**,** gold nanoparticles (AuNPs) stabilized in an aqueous-citrate solution were added to the hydrolyzed Kevlar/KOH/DMSO as a crosslinking agent. The amount of the gold citrate solution and the diameter of the AuNPs, controlled by the ratio of citrate and gold used during the preparation of the AuNP solution **[**8**]**, were varied to study the effects of different reactive conditions on the properties of the final product. To induce this reactive mechanism, the hydrolyzed Kevlar solution was first cooled from 373 K to 353 K; then, the desired amount of AuNP solution was slowly dripped into the Kevlar/DMSO solution using a delivery pipette; the entire process was carried out under constant stirring. Once the AuNP solution was completely dripped into the reaction vessel, the system was left stirring for two hours at 353 K. A temperature of 353 K was selected for three reasons: to avoid the further hydrolysis of amines from the Kevlar backbone molecules and from the proposed citrate-amine condensation, to avoid the diffusion and conglomeration of

AuNPs into larger diameter particles, and to provide a high enough temperature to slowly evaporate water within the vessel and force the equilibrium of the system towards the products of the condensation reactions.

Vacuum-assisted filtration of the reacted product. The resulting suspension was filtered using the filtration flask, as discussed in section 3.1.2 and shown in Figure 3.5. The color of the resulting film on the filter paper ranged from dark yellow to gray, blue and purple, depending on the amount of AuNP solution used and the gold particle size. The optical picture of a typical film is shown in Figure 37. A transparent and colorless solution was recovered from the filtered solvent.

Solid product drying and cleaning. To remove any residually absorbed solvent and consolidate the formation of a solid product sheet, the recovered "slush" on the filter paper was placed in a 338 K oven for 24 hours. After this drying process, a homogeneous thin film resulted. The product could easily be separated from the filter paper after soaking the sample with the filter paper in de-ionized water and then removing the moist filter paper with tweezers. The clean product sheets were placed in hot water (353 K -373 K) for an hour; after this washing step, the samples became significantly thinner, less opaque, slightly more translucent, and substantially tougher. This change in morphology indicates an important increase in sample crystallinity, which is most likely induced by the transfer of protons from the water to the polymer structure. This process contributes to the restoration of surface and secondary bonding within the solid, causing an increase of inter-chain interaction that may improve properties. Figure 3.7 shows the sample pictures.

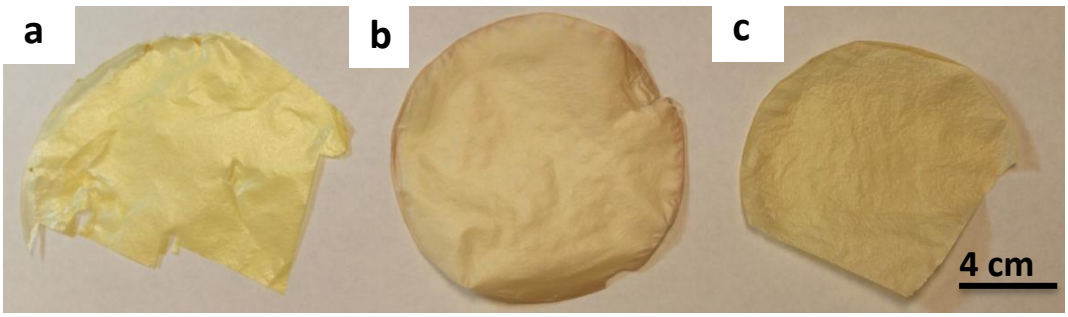

Figure 3.6 Optical images of aramid networks prepared by filtration method. a)An ANF network with no treatment. The aramid PA-treated/citrate sample (with no gold nanoparticles) with b) 4.2 mg citrate and c) 13 mg citrate.

3.1.5 Synthesis of Aramid PA-Treated/Citrate Sample (with No Gold Nanoparticles)

As a comparison to the samples with the PA/AuNP treatment and to determine the strengthening effects induced by the formation of Kevlar-gold complexes, samples of Kevlar reacted with pure tri-sodium citrate were prepared. The methodology for this synthetic step is exactly the same as that of Kevlar/AuNP samples, except that citrate powder (dehydrated, Sigma Aldrich) instead of the gold citrate solution was added into the reaction vessel after the PA hydrolysis step. Figure 3.6 b-c shows the aramid PA-treated/citrate samples (with no gold nanoparticles).

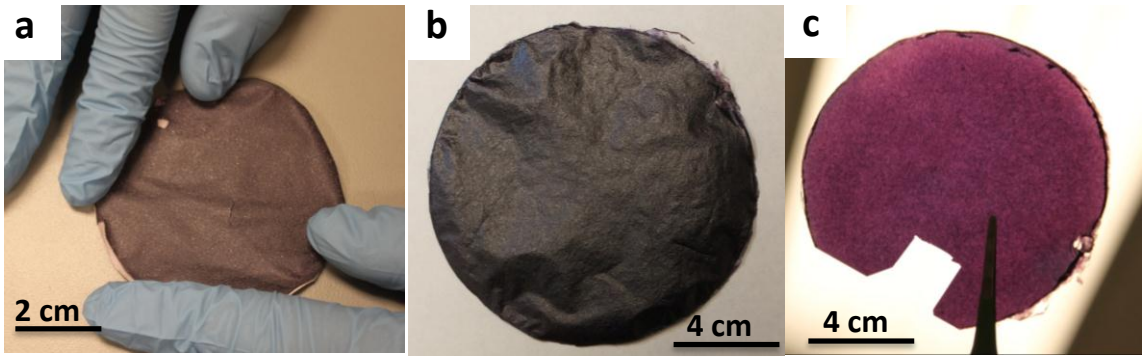

Figure 3.7 Aramid networks with gold nanoparticles (Kevlar/PA/Citrate+AuNP Nanocomposites), a) on a filter paper, b) on a piece of write paper, c) translucent through the light.

3.2 Characterization

3.2.1 Low-Rate Mechanical Testing

The mechanical properties of the filtered films were characterized by uniaxial tensile tests. Test specimens were 1.5 mm wide and 8 to 10 mm long in the gauge section. To verify the isotropy of the samples, test specimens were cut at various in-plane orientations from each sample. Each specimen was tested using an RSA III dynamic mechanical analyzer (DMA) (TA instruments), shown in Figure 3.8, under a constant nominal strain rate of 0.005 s^{-1} to ensure quasi-static loading until it fractured. The load was measured by a load cell with a maximum capacity of 3.5 N and a resolution of 1 μN. Digital image correlation (DIC) with a Grasshopper camera (Point Grey research) was used to measure displacements accurately, and the nominal strain field was computed by MetaMorph microscopy automation and image analysis software (Molecular Devices). Figure 3.9 shows a patterned sample and a Metamorph-processed image with strain contours. The tensile mechanical data were used to determine the stress-strain responses. The thickness of the films was determined by scanning electron microscopy (FEI Quanta 3D SEM/FIB and Philips XL30ESEM). The nominal stress was determined from load data divided by the initial cross-sectional area. The Young's modulus was determined from the slope of the initial linear region of the stress-strain response curves. The yield strength was determined as the proportional limit of the initial linear region of the stress-strain response curves, up to which, stress is proportional to strain.

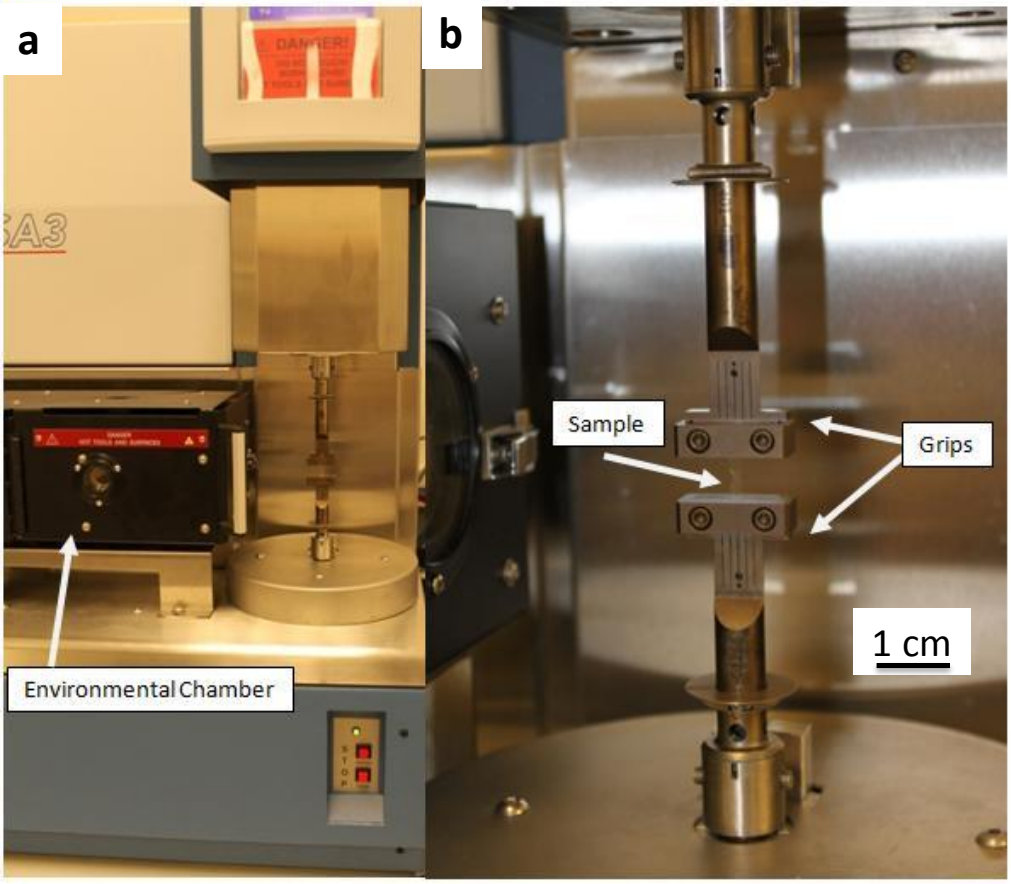

Figure 3.8 a) The RSA III dynamic mechanical analyzer (DMA) from TA instruments with an environmental chamber for changing temperature. b) A close-up view of the grips and sample.

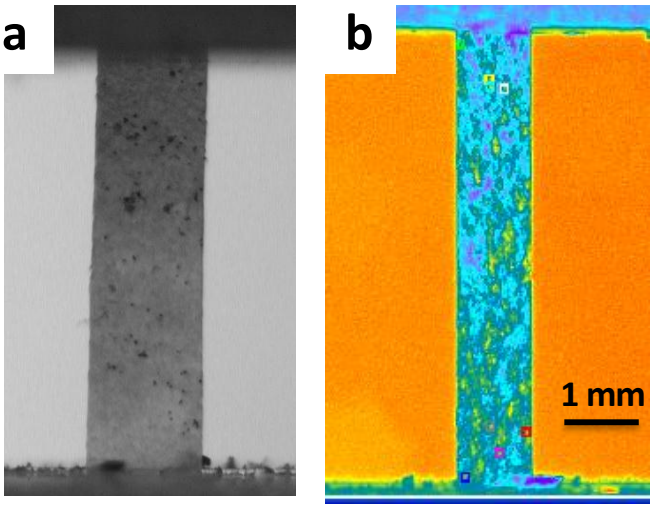

Figure 3.9 a) A patterned sample for low-rate uniaxial tensile testing. b) A Metamorph-processed image showing the contrast of different patterns on the samples which are used for tracking the deformation of the sample upon loading and for calculating the strain data.

3.2.2 Dynamic Mechanical Analysis

Temperature sweep tests using the RSA III DMA were conducted from -100 ^{0}C to 180 ^{0}C with 10 ^{0}C min^{-1} increments at 1 Hz. A strain of 0.25 ± 0.10 % was applied, from which the storage modulus and the loss tangent (tanδ) of the samples were characterized over the temperature range. The tensile and dynamic mechanical analysis data were used to determine the stress-strain responses and storage modulus and loss tangent vs. temperature responses. The storage modulus and loss tangent as a function of temperature were computed by Orchestrator software (TA instruments).

3.2.3 Fourier-Transform Infrared (FTIR) Spectroscopy

FTIR spectroscopy, through a liquid-nitrogen-cooled Thermo Nicolet 6700 spectrometer (Thermo Electron Corporation), was used to probe the chemical structures of the solid products obtained from specimens with and without the PA/citrate+AuNPs treatment in 85° grazing angle mode with a 16 mm aperture. At least 128 scans were taken per sample.

3.2.4 Transmission-Electron Microscopy (TEM) Characterizations

The morphologies of various aramids in DMSO solutions before, during and after the PA/GA or PA/citrate+AuNPs treatments were obtained using a JEOL 3011 high-resolution electron microscope at 300 kV. One drop of solution was placed on the surface of a copper grid coated with carbon (Ted Pella) and the solvent was evaporated prior to TEM characterization. The aramid structures were imaged at 10,000 to 20,000 × magnifications.

3.2.5 UV-Vis Spectroscopy Characterizations

The interaction of the AuNPs with the aramid matrix in both liquid and solid forms was inspected by UV-vis absorption spectra, taken with 8453 UV-Vis spectrophotometer (Agilent Technologies).

3.2.6 Thermo-Gravimetric Analysis (TGA)

The thermal properties of the aramid nanostructured networks were characterized by a thermo-gravimetric analyzer Pyris 1 (PerkinElmer) using a heating rate of 10 ^{0}C min^{-1} from 30 ^{0}C to 900 ^{0}C and an air purge at a flow rate of 20 mL·min^{-1}. The mass of the samples was controlled between 1.35 mg and 1.50 mg for all tests.

3.3 Commercial Kevlar Mat

Commercially available Kevlar mats with 0° & 90° plain woven fibers (Hexcel) were tested for their mechanical properties as a benchmark to compare with those of aramid networks. Both uniaxial tensile testing, via an MTS machine (Mini Bionix 858), and plane strain testing, via a custom-made machine, were conducted along the fiber axes of the mat at a

displacement rate of 1mm/s. Figure 3.10 shows the plane strain test on the mat by applying tension along the 90° fibers and holding along the 0° fibers. Figure 3.11 shows the uniaxial test on the mat by applying tension along the 90° fibers and with free ends for the 0° fibers.

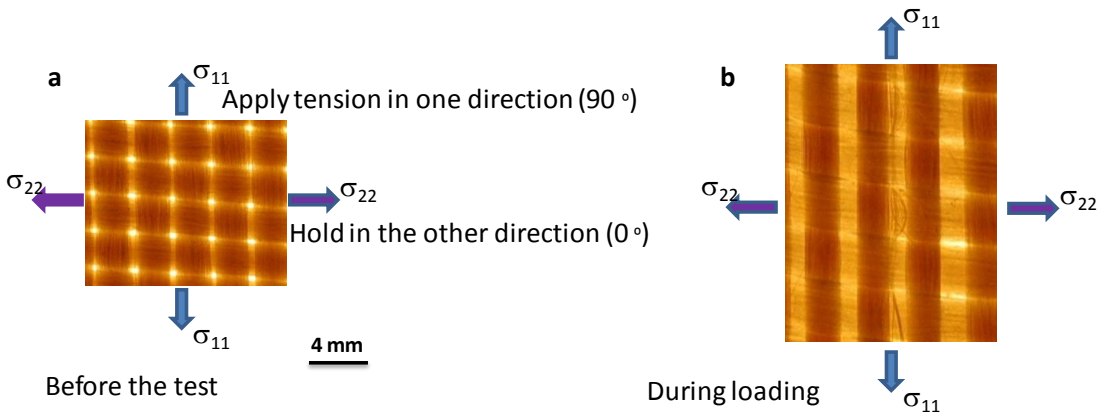

Figure 3.10 Plane strain testing on a 0° & 90° plain woven Kevlar mat. a) Before applying any tension. b) Fiber fracture upon tension.

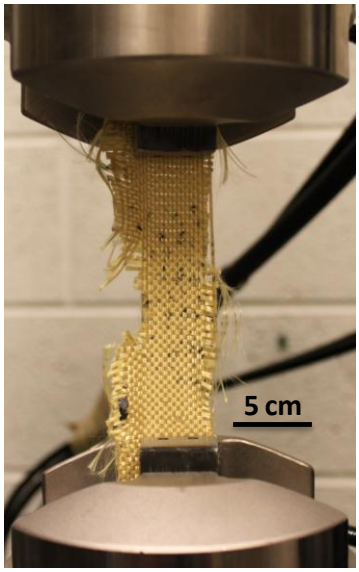

Figure 3.11 Uniaxial tensile testing on a 0° & 90° plain woven Kevlar mat.

Reference

[1] I. O'Connor, H. Hayden, J. N. Coleman, Y. K. Gun'ko, "High-Strength, High-Toughness Composites Fibers by Swelling Kevlar in Nanotube Suspensions," *Small* **2009**, Vol. 5, No. 4, pp. 466-469.

[2] M. Yang, K. Cao, L. Sui,Y. Qi, J. Zhu, A. M. Waas, E. M. Arruda, J. Kieffer, M. D. Thouless, N. A. Kotov, "Dispersions of ANSs: A New Nanoscale Building Block," *ACS Nano* **2011**, Vol. 5, No. 9, pp. 6945–6954.

[3] R. R. Burch and L. E. Manring, "N-Alkylation and Hofmann Elimination from Thermal Decomposition of R4N+ Salts of Aromatic Polyamide Polyanions: Synthesis and Stereochemistry of N-Alkylated Aromatic Polyamides,"*Macromolecules* **1991**, Vol. 24, pp. 1731-1735.

[4] Arif A. Mamedov, Nicholas A. Kotov, Maurizio Prato, Dirk M. Guldi, James P. Wicksted and Andreas Hirsch, "Molecular design of strong single-wall carbon nanotube/polyelectrolyte multilayer composites," *Nat. Mater.* **2002**, Vol. 1, pp. 190-194.

[5] P. Podsiadlo, A. K. Kaushik, E. M. Arruda, A. M. Waas, B. S. Shim, J. Xu, H. Nandivada, B. G. Pumplin, J. Lahann, A. Ramamoorthy, N. A. Kotov, "Ultrastrong and Stiff Layered Polymer Nanocomposite," *Science* **2007**, Vol. 318, pp. 80-83.

[6] A. K. Kaushik , P. Podsiadlo, M. Qin, C. M. Shaw, A. M. Waas, N. A. Kotov, E. M. Arruda, "The Role of Nanoparticle Layer Separation in the Finite Deformation Response of Layered Polyurethane-Clay Nanocomposites," *Macromolecules* **2009**, Vol. 42, pp. 6588-6595.

[7] Podsiadlo P. et al, "LBL Assembled Laminates with Hierarchical Organization from Nano- to Microscale: High-Toughness Nanomaterials and Deformation Imaging," *ACS Nano* **2009**, Vol. 3, No. 6, pp. 1564-1572.

[8] G. Frens, "Controlled Nucleation for the Regulation of the Particle Size in Monodisperse Gold Suspensions', *Nat. Phys. Sci.* **1973**, Vol. 241, pp. 20-22.

Chapter 4

Aramid Nanostructures: Nanoscale Building Blocks

The nanoscale polymer fibers, which differ from their bulk forms, are expected to bring about unique mechanical, electrical, and optical properties, similar to the nanoscale versions of many metals or semiconductors. The smaller size of these nanoscale ultrastrong fibers provides higher surface area over volume, which makes them interact with other materials better than their bulk counterparts and makes them ideal as constituents in composites. Polymer nanofibers should be considered as nanoscale organic "building blocks," similar to inorganic nanofibers well-known in materials science such as nanoparticles, nanowires, carbon nanotubes (CNTs), graphene nanosheets (GNSs), and clay nanosheets (MTM). Dispersions of polymer nanofibers in solutions are analogous to those obtained for all the other inorganic nanoscale components, and are most useful for the functional design of nanocomposites and metamaterials. Various combinations of organic components, in the forms of molecular solutions or nanofiber dispersions, and inorganic nanofillers will make possible material properties which are currently considered to be difficult or impossible to obtain. As the choice of polymer nanofiber dispersions is limited or not known for most polymers, compared to dispersions of inorganic nanoscale materials, the preparation of polymer nanofibers is virtually opening a new territory for both chemical and materials research.

4.1 The Nature of Kevlar/DMSO Solution

Stable dispersions of nanoscale Kevlar fibers with diameters between 3 and 30 nm were obtained by deprotonating macroscale, commercial Kevlar yarns with potassium hydroxide (KOH) in dimethyl sulfoxide (DMSO). These aramid nanofibers (ANFs) were negatively charged, uniformly sized in DMSO by controlled deprotonation with KOH [1]. Such dispersions represent the first example of nanofiber dispersions of synthetic polymers. They are suitable for making nanoscale materials using many techniques and can be considered as new nanoscale building blocks for ultrastrong materials [1].

The morphologies of ANFs were characterized by atomic force microscopy (AFM), transmission electron microscopy (TEM) and scanning electron microscopy (SEM) as shown in Figures 4.1 to 4.3. Figure 4.1 compares the differences of surface morphology with and without ANFs through AFM. Figure 4.1.a shows a surface of a layer of PDDA deposited on a glass substrate, and a flat surface without any nanofiber features was revealed. After a layer of ANFs was deposited on the PDDA layer, randomly-oriented fibers were observed, as shown in Figure 4.1.b. A height on the order of 10 nm was measured by AFM, which corresponsed to the diameter of ANFs. Figure 4.1.c shows a denser coverage of ANFs after four layers were deposited, indicating the growth of the layers through the interactions among the ANFs. TEM and SEM images in Figures 4.2 and 4.3 show similar nanofiber features and sizes. Figure 4.4 compares Raman scattering spectra of the Kevlar/DMSO solution and the Kevlar yarn, to observe the molecular vibrations by an inelastic scattering process. Most chemical bonds of ANFs are generally in a more relaxed state in DMSO (i.e. under less stretching owing to reduced distances), compared to those of the Kevlar fibers, as most of the peaks from ANFs shifted to higher wave-numbers. The phenyl (benzene ring) of the aramid backbone molecules, corresponding to the peak at 1613 cm^{-1}, was the only group that got more strained or stretched, possibly owing to the increased benezene ring interactions in the solution. The presence of ions in the solution, however, may also affect the peak wave-numbers.

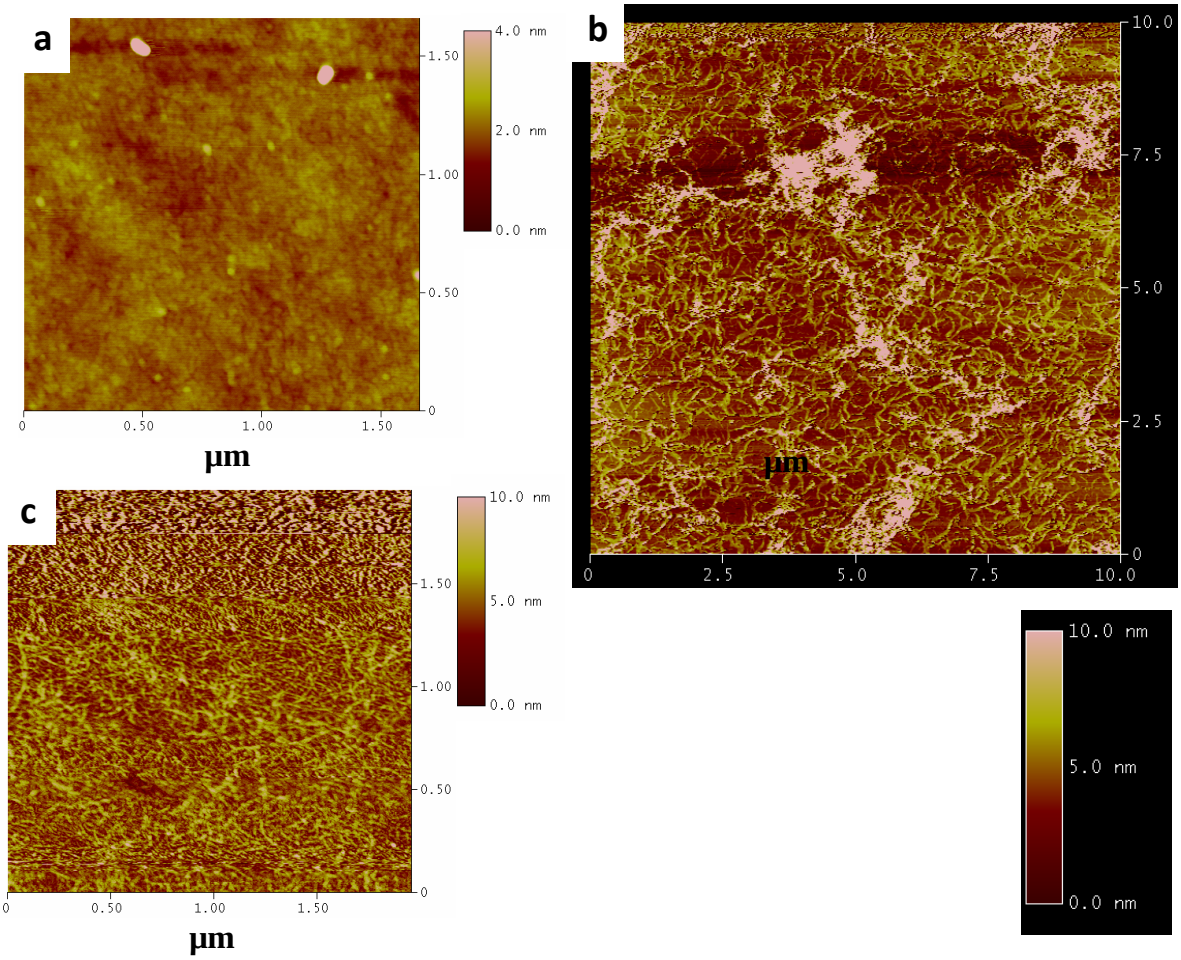

Figure 4.1. AFM images showing the morphologies of ANFs deposited on a glass substrate: a) a flat surface after coating the glass substrate with a layer of PDDA; b) randomly oriented ANFs after depositing a layer of ANFs on top of the PDDA layer, and a largest height of ~ 10nm was measured, which corresponded to the diameters of the ANFs; c) more ANFs were observed on the PDDA layers upon four layers of ANFs were deposited.

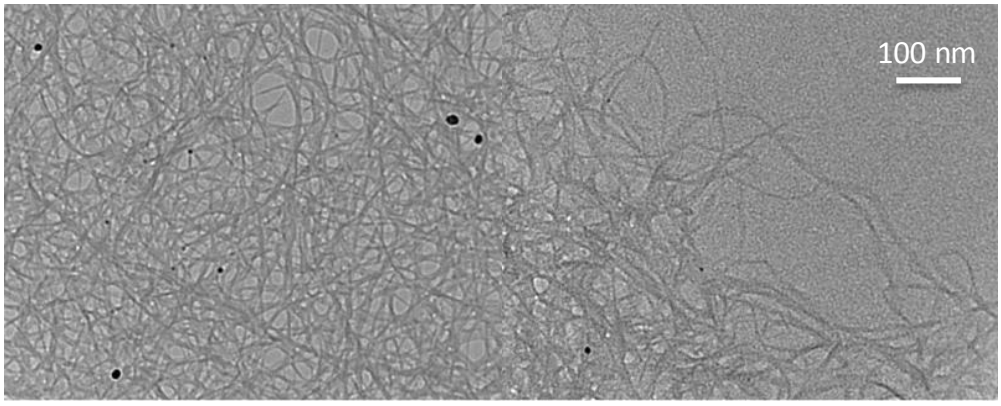

Figure 4.2. A TEM image showing the morphology of ANFs after evaporating DMSO. Image reproduced from Yang et. al., 2011 [1]**.**

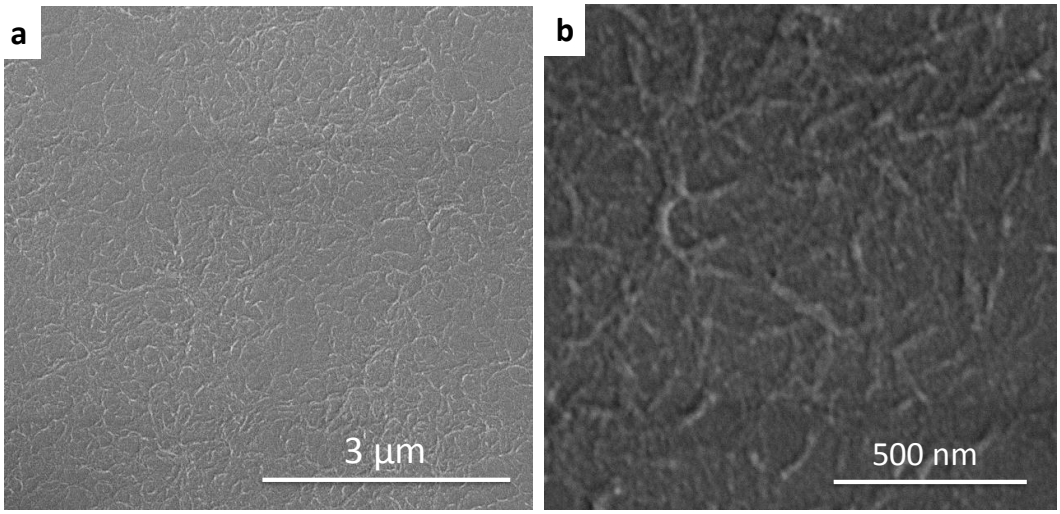

Figure 4.3. SEM images showing the morphologies of ANFs deposited on a glass substrate. Image reproduced from Yang et. al., 2011 [1]**.**

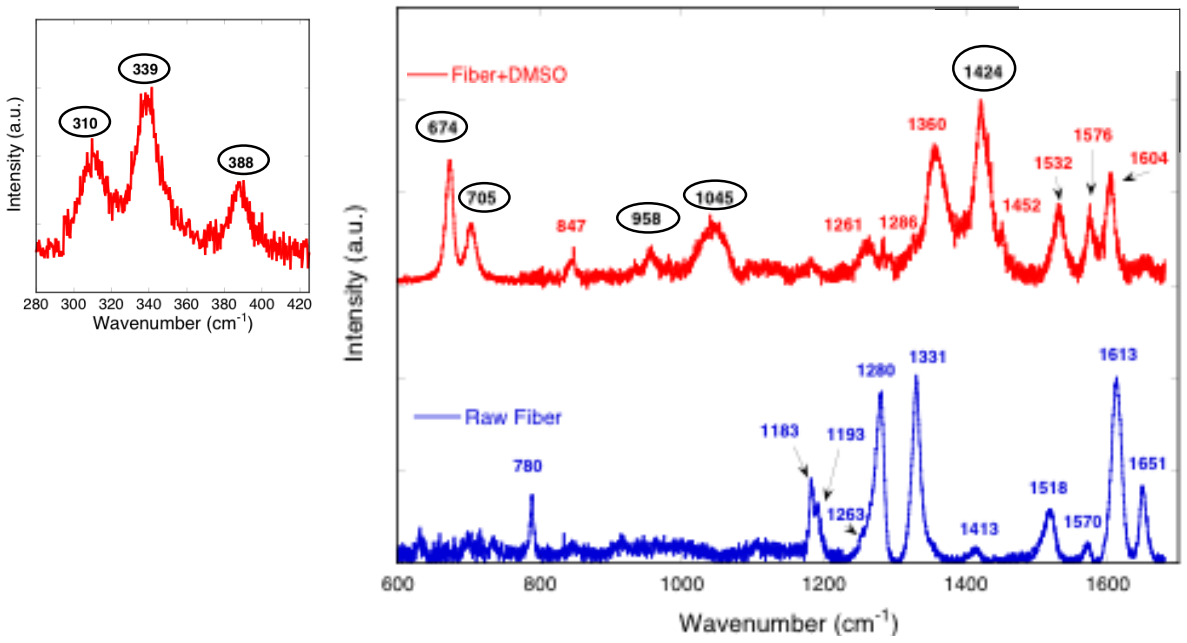

Figure 4.4 Raman scattering spectroscopy on Kevlar/DMSO solution (top) and Kevlar fiber (bottom). Peak numbers in circles indicate peaks from DMSO, and the rest of peaks are from Kevlar. There is a significant difference in the Raman scattering from Kevlar when it is dissolved in DMSO; most of the Kevlar peaks shift to higher wave-numbers with the exception of the peak at 1613 cm^{-1}. This suggests that, with the exception of the phenyl backbone (corresponding to the peak at 1613 cm^{-1}) which is more stretched, the Kevlar bonds are generally more relaxed in DMSO.

4.2 The LBL-Assembled ANF Films with No Treatment

The mechanical properties of the ANF LBL films (ANF networks with no treatment) were characterized by uniaxial tensile testing at a strain rate of 0.005/s at room temperature. Through the characterization, it can be concluded that ANFs are inert in terms of bonding with themselves or with other materials, which hampers the mechanical properties of ANF-based nanocomposites with no treatment. An ANF LBL film was made by depositing layers of ANFs repeatedly from the Kevlar/DMSO solution to form an ANF network. This assembly method yielded transverse isotropy of the network morphology, as the nanofibers were randomly oriented in the plane and were stacked along the out-of-plane/thickness direction, as shown in Figure 3.2. The resultant mechanical properties were isotropic in the plane parallel

to the substrate, compared to the thickness direction. Figure 4.5 shows a stress-strain curve of the ANF film, obtained from the uniaxial tensile testing to characterize its in-plane mechanical properties. As shown by the uniaxial tensile test, the ANF network was relatively brittle with a strain to failure of 1.3 %. This brittleness comes from the low surface affinity of ANFs with each other. As discussed in Chapter 2, aramid polymers have a characteristic of having weak bonding with other materials. The fracture of the network occurred at the weakest link in the network, where the weak bonding among the ANFs caused this premature failure, hampering the ultimate tensile strength of the ANF LBL network. The network failed without having the stiff and strong aramid macromolecules fully stretched. The strong aramid backbones should be fully utilized by having stronger bonding among them to have better load transfer and yield better mechanical properties.

The interaction of ANFs with other materials was investigated by implementing polyvinyl alcohol (PVA) and montmorillonite (MTM) clay nanoparticles in the LBL assembly to create ANF-based nanocomposites. An ANF/MTM film was made by alternating a layer of ANF and a layer of MTM to create a nanoparticle-filled nanocomposite. The resultant strain to failure of the ANF/MTM film was even lower than that of the ANF LBL film, and no significant increases of stiffness or strength was obtained. Given that the stiffness of MTM is ~109 GPa and there was an 11 wt% of MTM in the nanoscomposite, as measured by TGA, some reinforcement effect from the MTM nanoparticles should be observed. However, both the low strain to failure and decreased stiffness of the ANF/MTM film indicate limited interactions between ANFs and MTM. Moreover, an ANF/PVA film was made similarly by alternating a layer of ANF and a layer of PVA to create a nanocomposite with two different polymers. As shown in Table 4.1, the ANF/PVA film, crosslinked by GA via soaking in GA for 24 hours, yielded similar stiffness, strength and strain to failure as those of the ANF LBL film. This similarity of the mechanical properties was also caused by the limited interactions among the constituents of the ANF/PVA nanocomposites. Another film was made with layers of ANF, PVA, MTM and PVA. As PVA forms strong bonds with MTM, better stress transfer should be expected from the polymer matrix to the nanofillers. However, although this ANF/PVA/MTM/PVA nanocomposite had the best stiffness among all ANF LBL samples, the strain to failure of this nanocomposite was the lowest, which also supports the conclusion that ANFs are inert to form bonding with PVA or MTM.

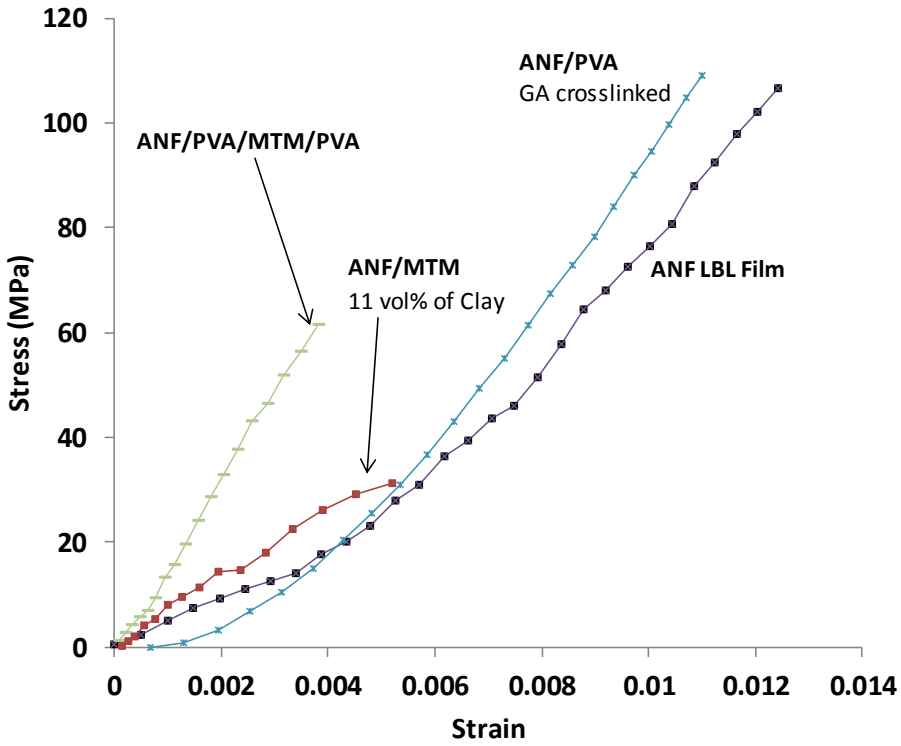

Figure 4.5 Stress-strain curves of the ANF films assembled by the LBL method characterized by uniaxial tensile test at 0.005/s. Here the materials were all considered as elastic and the stiffness was obtained by measuring the slope of each entire stress-strain curve.

Mechanical Properties	Tensile Strength (MPa)	Stiffness (GPa)	Strain at Failure (%)
ANF LBL Film	120 ± 15	11.0 ± 1.2	1.3 ± 0.2
ANF/MTM Nanocomposite	30 ± 4	6.2 ± 1.0	0.6 ± 0.2
ANF/PVA/MTM/PVA Nanocomposite	65 ± 6	17.3 ± 2.5	0.4 ± 0.1
ANF/PVA Nanocomposite	120 ± 12	12.5 ± 1.7	1.1 ± 0.4

Table 4.1 Mechanical properties of the ANF films assembled by the LBL method.

4.3 The LBL-Assembled ANF Films with PA/GA Treatment

To enhance the interactions among the ANFs, a two-step chemical treatment was introduced during the LBL process for better mechanical properties by creating crosslinks among the ANFs. Raman scattering indicated that Kevlar macromolecules are in a more relaxed state in the DMSO solution before gaining the hydrogen back by rinsing in the water. Thus, an in-situ functionalization process with phosphoric acid (PA) and glutaraldehyde (GA) was used to modify Kevlar macromolecules and introduce crosslinks between the polymer chains [2-4]. After dipping the PDDA-coated substrate into the Kevlar/DMSO solution for a layer of ANFs, the substrate was dipped into a 10wt% PA solution for one minute which was hypothesized to introduce chemical reactions promoting reactivity of the polymer chains. The ANF network was further crosslinked by submerging it in a 10 wt% GA solution for one minute. All the modifications on the Kevlar macromolecules were introduced during the fabrication process instead of during post-processing to ensure the effectiveness of the funtionalization. This PA and GA functionalized ANF/PA/GA film showed a 2.5 fold improvement of stiffness and strength over the untreated Kevlar LBL film and is comparable to the properties of plain-weaved Kevlar mat along its strongest axis: the fiber direction. The details of the uniaxial and plane strain tensile tests on Kevlar mat will be discussed further in Chapter 6. This ANF/PA/GA film also compares favorably to the properties described by Burch et al. [5] of Kevlar thin films prepared by casting a Kevlar polyanion orangnic solution. Burch et al. claimed in that work that aramid polyanions were obtained in the organic solution [5]. Figure 4.6 shows the stress-strain curves of ANF LBL films with and without PA/GA treatment. The mechanical properties of the ANF films are further compared in Table 4.2 with those of commercial Kevlar mats and Kevlar films prepared by casting as reported in literature.

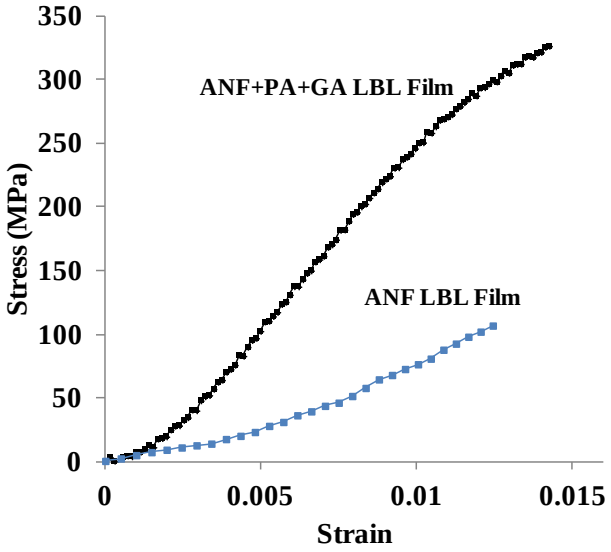

Figure 4.6 Stress strain curves of functionalized and crosslinked Kevlar LBL film (ANF/PA/GA) and ANF LBL film with no treatment.

Average Values from Measurements	Stiffness GPa	Strength MPa	Strain at failure %
ANF/PA/GA film	27 ± 2	300 ± 20	1.5 ± 0.2
Untreated ANF LBL film	11 ± 1	120 ± 15	1.3 ± 0.2
Kevlar Mat	21 ± 1	320 ± 18	3.0 ± 1.2
Kevlar fiber	85	4.0	4.5
2% alkylated Kevlar film (cast) [5]	3.7	76	3.0
Kevlar film (cast) [5]	5.5	165	5.0

Table 4.2 Mechanical properties of functionalized Kevlar LBL films (ANF/PA/GA) and a comparison with other Kevlar-based materials.

The microstructure of Kevlar fiber, ANF LBL films and ANF/PA/GA LBL films were examined by Raman scattering and Fourier transform infrared spectroscopy (FTIR). Raman scattering tests in Figure 4.7 showed that the major peaks of the three samples were very similar, which indicated the preservation of the chemical structure of the Kevlar chains in three different morphologies. There was no destruction of the major bonds owing to the LBL or the functionalization process. The major structural features were restored after the LBL or

the functionalization process from the deprotonated state of Kevlar in DMSO. Meanwhile, some of the peaks in the ANF LBL films shifted slightly compared with those of Kevlar fiber. Most peaks corresponding to the carbon double bonds on the benzene rings moved to lower wavenumbers, which indicated a more stretched state of the benzene rings [6-8]. This agrees with the hypothesis that the interactions between the Kevlar chains in LBL films comes from the aramid stacking interaction. The amide linkage was the only part of the LBL film that was more relaxed compared to Kevlar fiber, which was caused by the less intensive hydrogen bonding between the Kevlar chains in the LBL film compared with those between the highly aligned Kevlar chains in the fiber form.

a

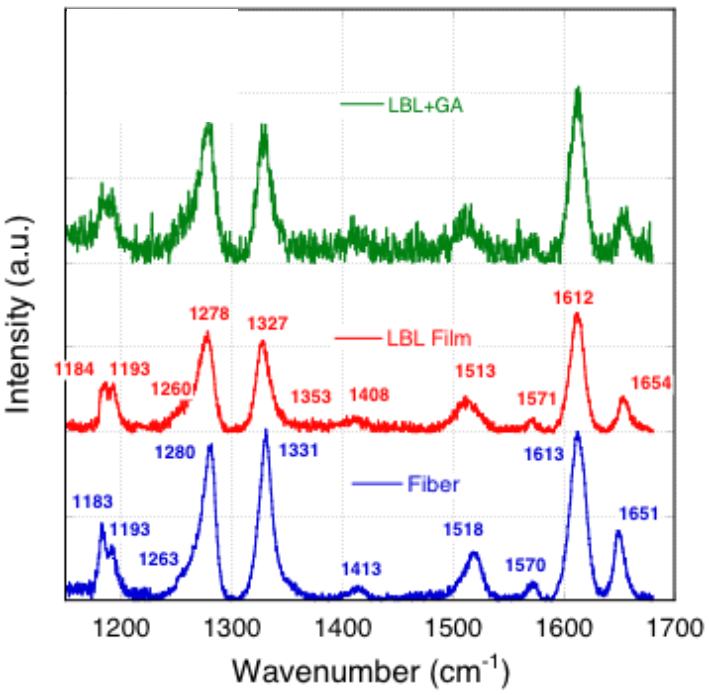

b

Wavenumber (cm^{-1})		Vibrational mode
Fiber	LBL	
790	790	Ring Vibrations
1183	1184	C-C ring stretch (c-ph-c)
1193	1193	C-C ring stretch (n-ph-n)
1263	**1260**	**C-C ring stretch (n-ph-n)**
1280	**1278**	**C-C ring stretch (n-ph-n)**
1331	**1327**	**C-C ring stretch (n-ph-n)**
1413	**1408**	**C-H bend**
1518	**1513 (Stretched)**	**C-C ring stretch (c-ph-c)**
1570	1571	60% N-H bend 40% C-N stretch
1613	1612	C-C ring stretch (along c-ph-c, n-ph-n backbone)
1651	1655 (Relaxed)	80% C=O stretch 10% C-N stretch 10% N-H bend

Figure 4.7 a) Raman scattering spectra comparing Kevlar fiber (bottom), ANF LBL film (middle) and ANF/PA/GA film (top). b) The peak assignments for the Kevlar fiber and the ANF LBL film. The peaks with bold fonts indicate a more stretched state of certain bonds in LBL films and the peak highlighted in green (the last row) indicates a more relaxed state of the LBL films. Those peak shifts can be explained by the change of morphology and interactions among the ANFs of the LBL film owing to the reconstruction of the macromolecules during the LBL process [6-8].

GA, however, is a very weak light scatterer, which makes it hard to probe the structural changes in the ANF/PA/GA film via Raman scattering [9-11]. The Raman scattering result (Figure 4.8) showed very similar peaks from the Kevlar fiber, ANF LBL films and ANF/PA/GA films. There was only one broad peak observed in the GA-crosslinked film, as shown in Figure Figure 4.8 (b). This "hump" was attributed to the effect of crosslinking from GA.

The microstructures of ANF LBL films and ANF/PA/GA LBL films were further compared by FTIR, as shown in Figure 4.9. A weak peak was observed in 3000-2800 cm^{-1} wave-numbers for the samples that contain GA. This peak is a good indicator of the presence of C-H bonds from sp^3 carbons and from aldehyde groups, thus indicating a crosslinking effect from GA. In addition, a peak at~ 1712 cm^{-1} wave-number emerged in the ANF/PA/GA LBL film. This additional peak was also possibly introduced by the PA/GA treatment.

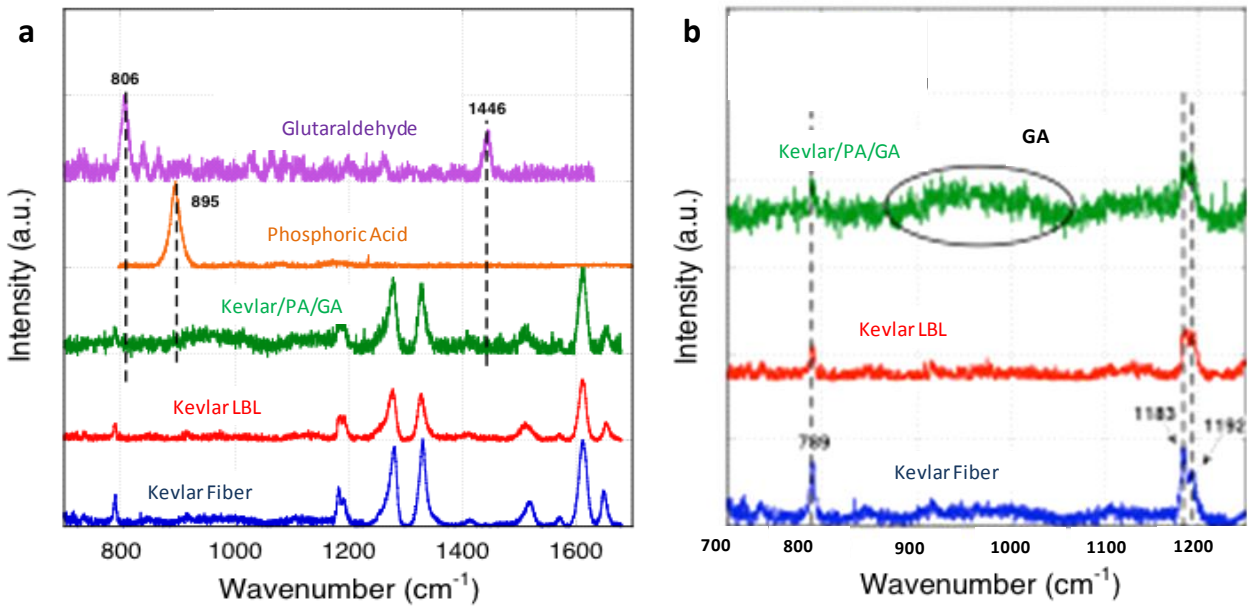

Figure 4.8 Raman scattering spectra probing the structural changes owing to the crosslinks in the ANF/PA/GA films. Since GA is a very weak scatterer, the samples with GA all showed noisier results. (a) Raman scattering spectra of glutaradehyde, phosphoric acid, ANF/PA/GA films, ANF LBL films and Kevlar fibers. (b) A unique broad peak was observed in the ANF/PA/GA film.

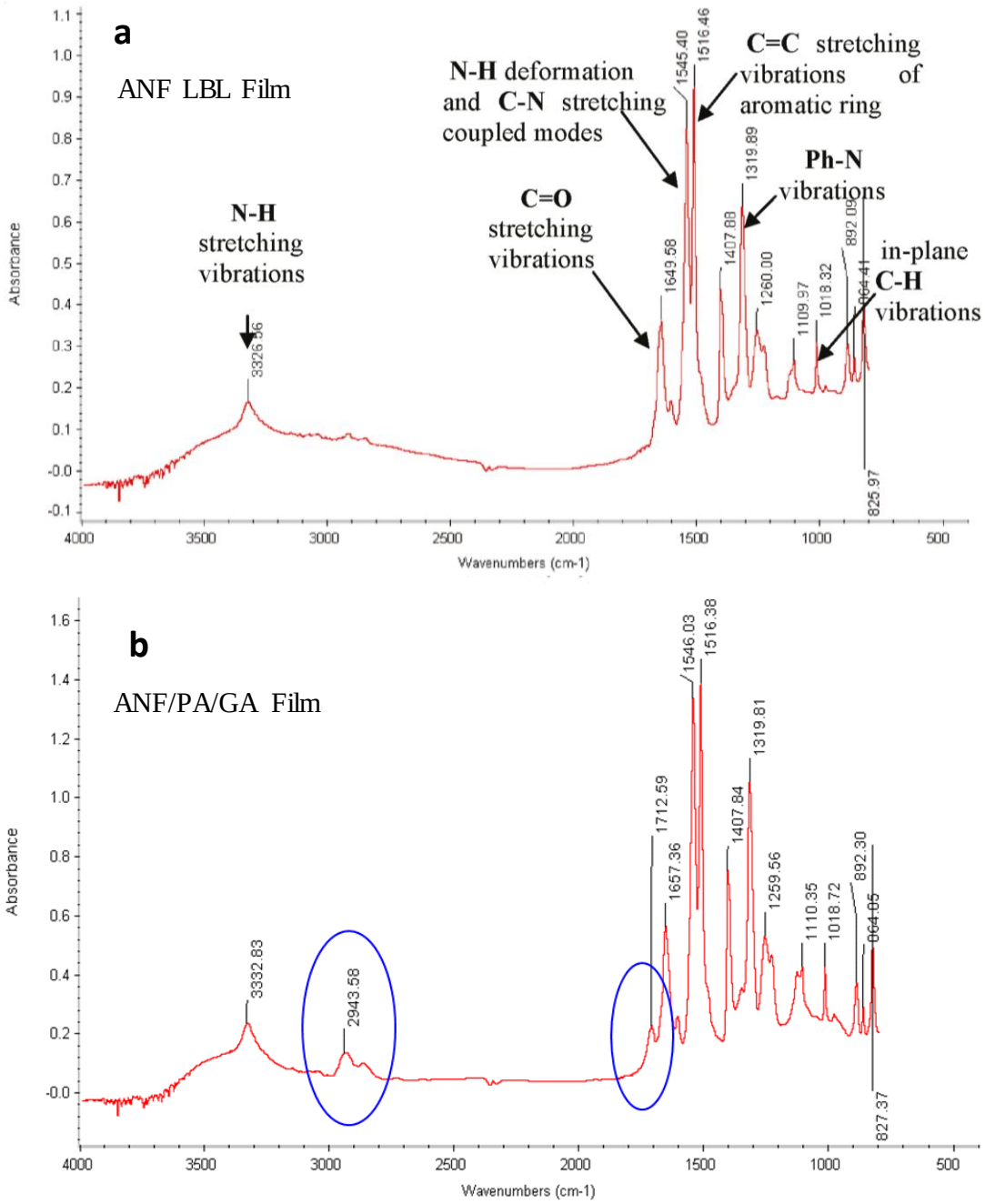

Figure 4.9 FTIR spectra comparing the ANF LBL film and the ANF/PA/GA LBL film. Additional peaks owing to the GA crosslinking were observed in the ANF/PA/GA LBL film.

4.4 The ANF LBL-Assembled Films with Hierarchical Structures

A hierarchical structure was created from the "hard" ANF/PA/GA LBL phase as building blocks embeded in a "soft" matrix for toughness improvements. Polyurethane (PU) and poly (acrylic acid) (PAA) LBL films studied in our group demonstrated highly ductile behavior of the PU/PAA system [12, 13]. Thus, PU/PAA was chosen to be the soft phase material bonding with ANF/PA/GA to create a hierarchical structure that possibly deflects crack propagation in the nanocomposite and prevents catastrophic failure of the brittle phase made of ANF/PA/GA. One hierarchical film was made as follows: after obtaining 25 layers of ANF/PA/GA (with a thickness of ~ 2.2 μm), the films were sequentially dipped in PU, PAA and PU solutions to get a thin tri-layer of PU/PAA/PU on one surface of the ANF/PA/GA film. Four films of this PU/PAA/PU coated ANF/PA/GA film were hotpressed under pressure of ~30 MPa at 230 °F for 30 minutes to bond the films. Figure 4.10 shows the schematic and optical pictures of this hierarchically structured nanocomposite.

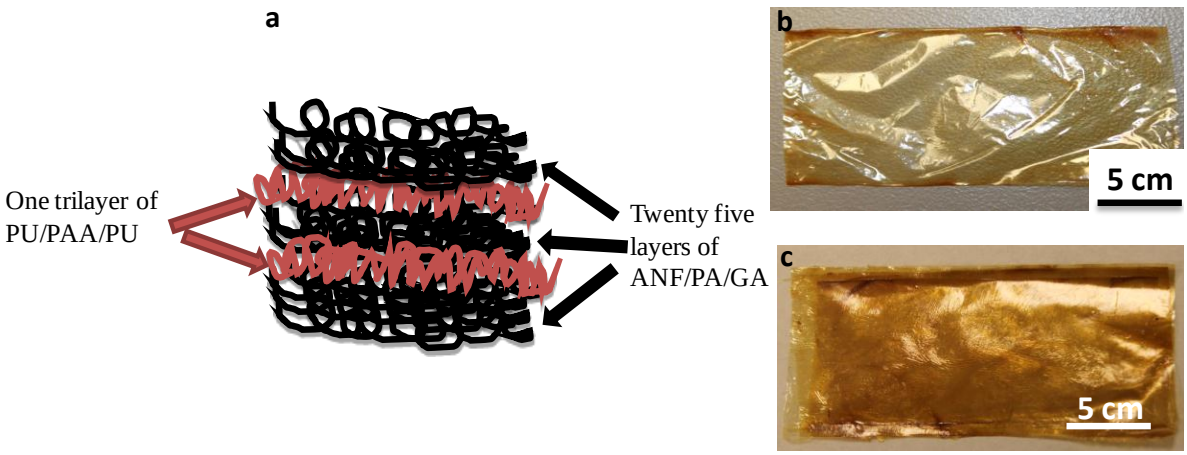

Figure 4.10 a) Schematic showing a hierarchical structure of an $(ANF/PA/GA)_{25}/(PU/PAA/PU)_1$ nanocomposite film. The PU/PAA/PU layers were implemented to improve the toughness of the nanocomposite by having ductile layers to deflect crack propagation. b) A picture of a single $(Kevlar/PA/GA)_{25}/(PU/PAA/PU)$ film vs. c) a hotpressed film made by hotpressing four films in b).

By tuning the thickness of the soft phase, that is the PU/PAA/PU tri-layer, a series of hierarchically structured Kevlar films was made. Different nanocomposite stiffness and ductility were obtained owing to different amounts of PU/PAA/PU in the films. The amount of the soft phase in the film can be measured via thermogravimetric analysis (TGA). Since the decomposition temperature of Kevlar is higher than that of PU/PAA, the soft phase in the nanocomposite starts to degrade first, and this degradation distinguishes the Kevlar phase from the soft phase. The stiffness and strength of the samples decrease with an increase in the amount of the soft phase, as indicated by the three samples with different loadings of the soft phase, shown in Figure 4.12.

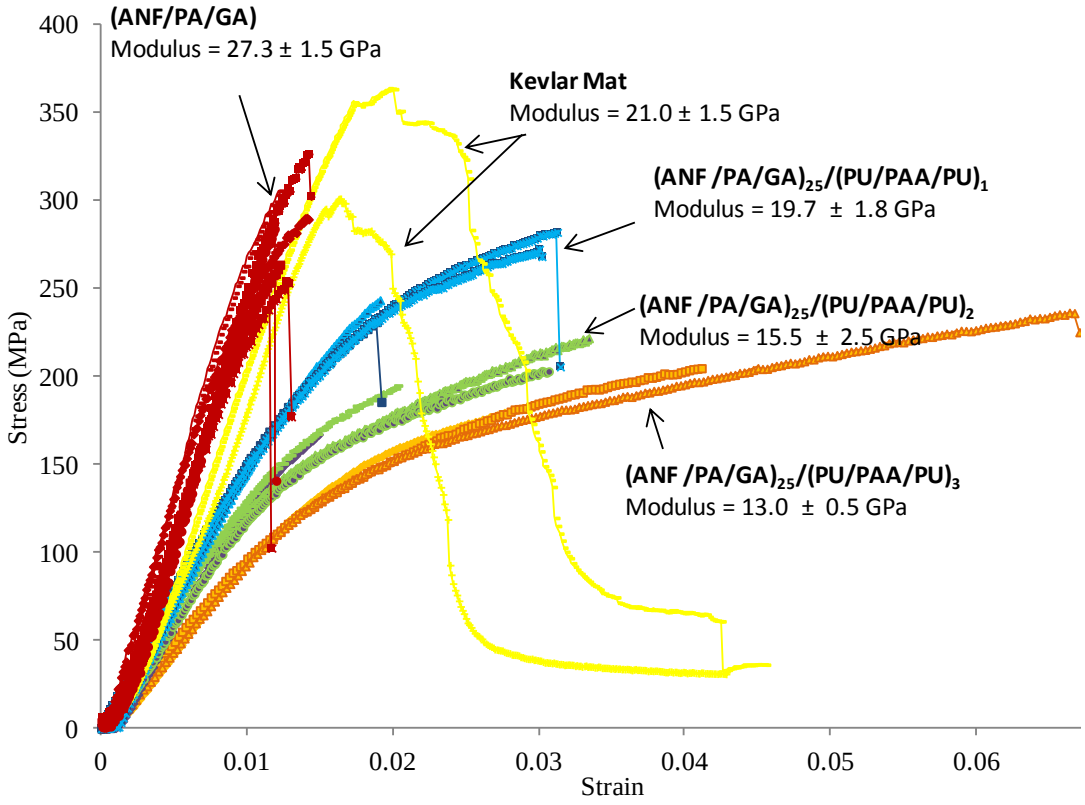

Figure 4.11 Stress-Strain curves of the ANF-based nanocomposites tested via uniaxial tensile tests at a low strain rate of 0.005/s.

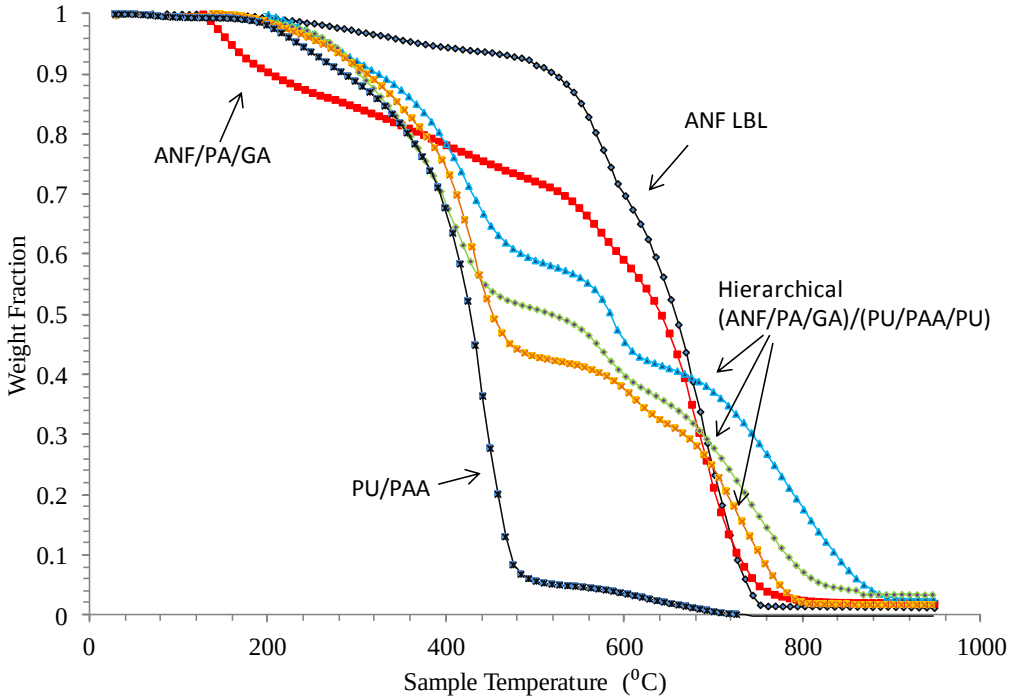

Figure 4.12 Thermogravimetric analyses of Kevlar-based hierarchical films compared with ANF LBL, ANF/PA/GA and PU/PAA/PU LBL films to probe the weight fraction of PU/PAA in the nanocomposites. The color of each film is the same as those in their corresponding stress-strain plot in Figure 4.11.

The hierarchical film $((ANF/PA/GA)_{25}/(PU/PAA/PU)_1$ in Figures 4.11 and 4.12 was further tested by dynamic mechanical analysis (DMA), where a frequency sweep from 0.01 Hz to 10 Hz was applied. Owing to the viscoelastic nature of polymers, the storage modulus and loss tangent (tanδ) of the polymeric materials are dependent on the strain rate (frequency) at a fixed temperature. The DMA tests were conducted under different static pre-loadings and strain oscillation amplitudes. A series of curves was generated, as shown in Figure 4.13, corresponding to each pre-loading and strain oscillation. The same test method was used on the ANF/PA/GA samples, as shown in Figure 4.14. The hierarchical Kevlar samples had larger tanδ than that of the ANF/PA/GA sample, especially at higher frequencies. This indicates that more mechanical energy applied to the hierarchical Kevlar samples was dissipated as heat. The higher damping in the hierarchical Kevlar samples is desired, as it could potentially provide more energy dissipation through materials at high frequency loading such as blast.

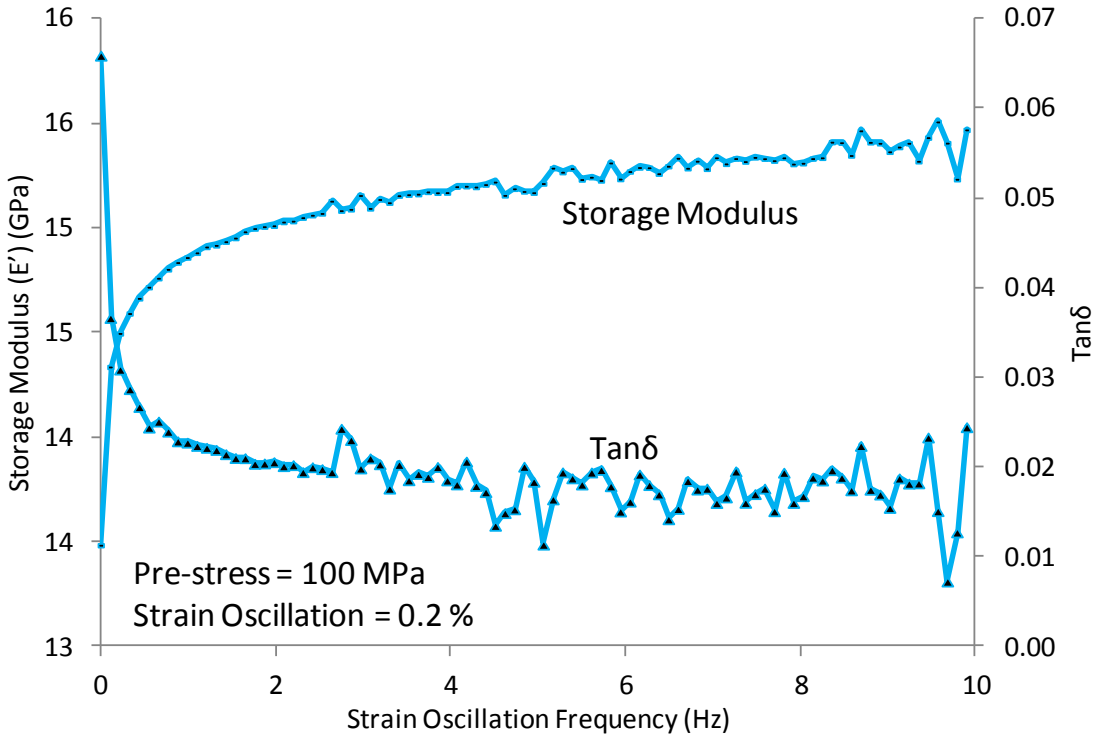

Figure 4.13 Frequency sweep dynamic mechanical analysis on hierarchical Kevlar nanocomposites $(ANF/PA/GA)_{25}/(PU/PAA/PU)_1$ in Figures 4.11 and 4.12 at room temperature. The stress levels in the figure legend indicate the preloading stress applied to the samples. The strain oscillation amplitudes are also provided in the legend. The top three curves are the storage modulus and the bottom three curves are the loss tangent of the samples.

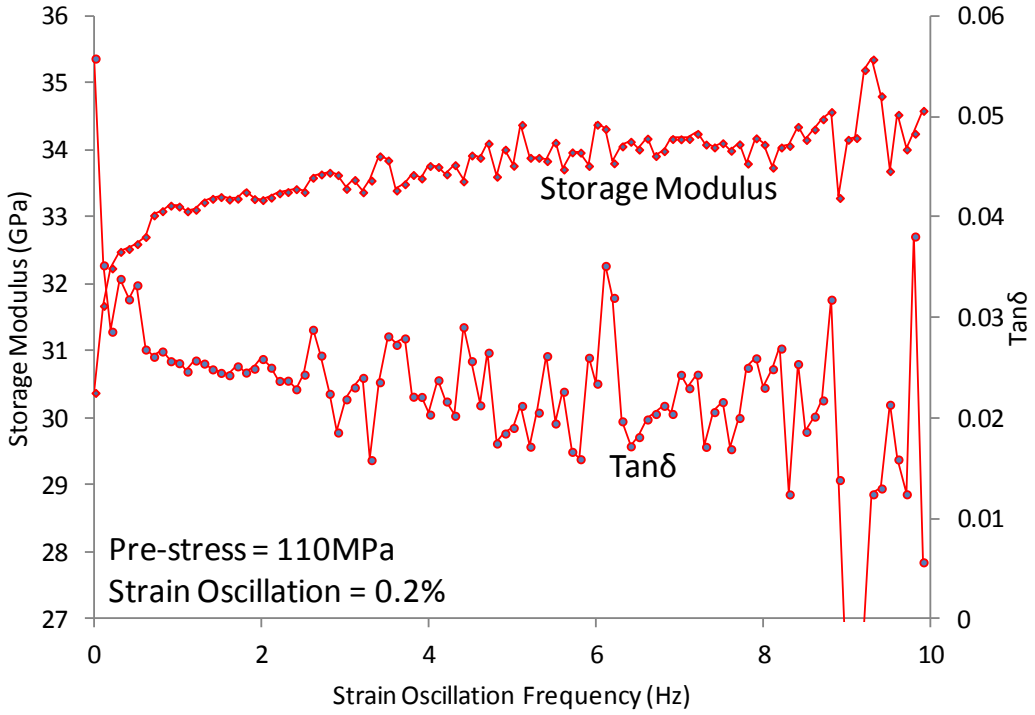

Figure 4.14 Frequency sweep dynamic mechanical analysis on the ANF/PA/GA films (ANF/PA/GA in Figures 4.11 and 12) at room temperature. The stress levels in the figure legend indicate the preloading stress applied to the samples. The strain oscillation amplitudes are provided in the legend. The top three curves are the storage modulus and the bottom three curves are the loss tangent of the samples. At higher frequencies, the tanδ data are near zero and therefore noisy.

The FTIR spectrum of the hierarchical films was compared with the FTIR spectra of PU/PAA LBL films, ANF LBL films and ANF/PA/GA LBL films in Figure 4.15. The additional FTIR peaks were assigned correspondingly with the chemical structure of PU and PAA in Figure 4.16. The hydroxyl peak (−OH) of PU/PAA in the hierarchical films didn't show up in the FTIR spectra of the hierarchical films; thus we proposed a reaction between the aramid polymer and PAA, which could potentially enhance the aramid macromolecules with PAA chains in Figure 4.17.

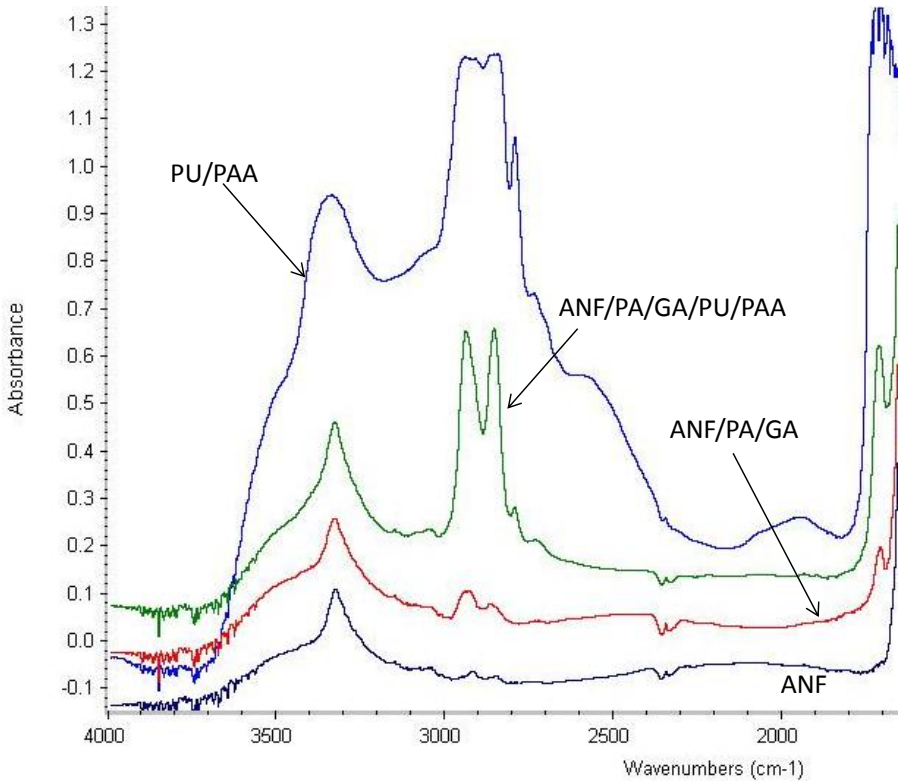

Figure 4.15 FTIR spectra comparing the hierarchical Kevlar film with ANF, ANF/ PA/GA and PU/PAA LBL films. The major suppressed peak is at wave-numbers from 2700-2500, which corresponds to the hydroxyl (-OH) group in PAA.

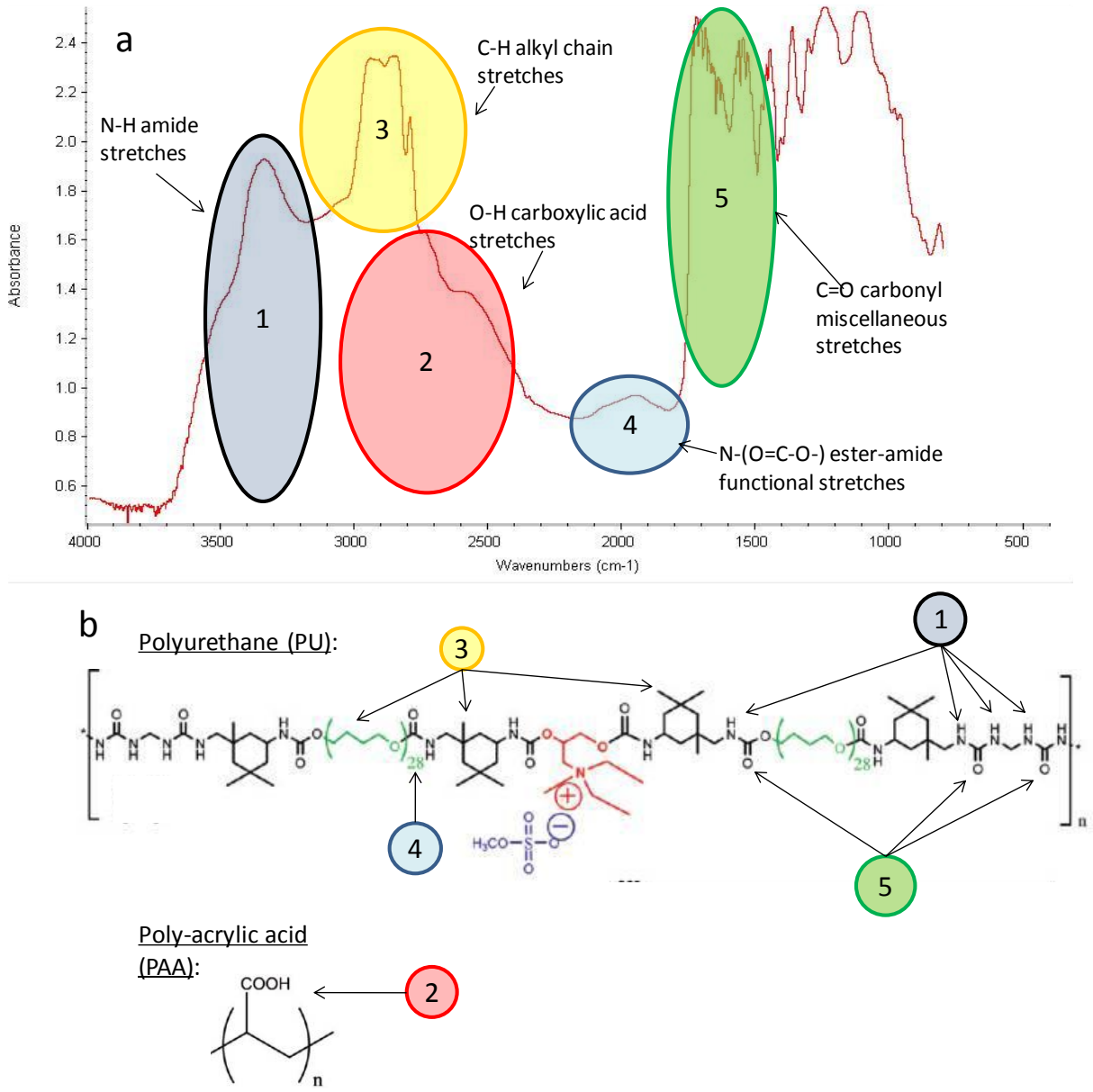

Figure 4.16 a) FTIR spectra of a PU/PAA LBL film with peak assignments and b) the chemical structures of PU and PAA. Kevlar and PU/PAA share some common chemical bonds that overlap at similar wave-numbers, but the suppression of –OH in the hierarchical film is apparent.

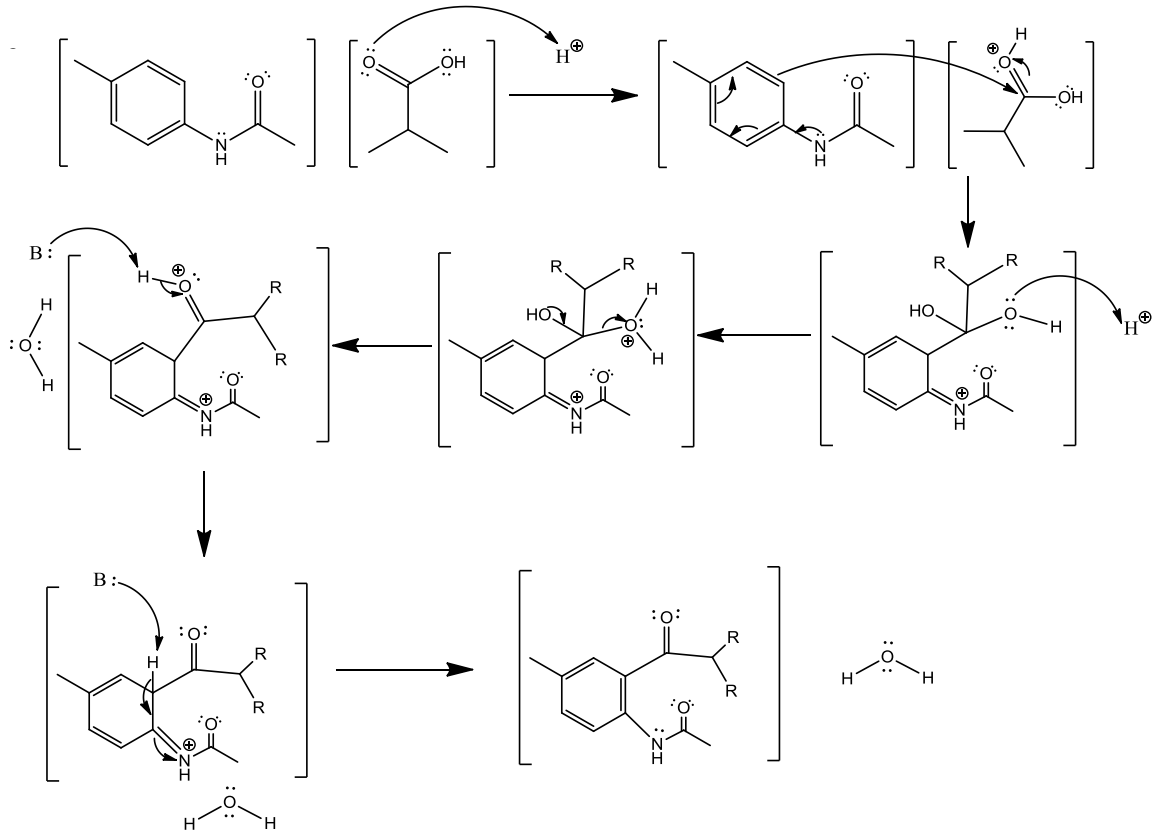

Figure 4.17 A proposed reaction mechanism between PAA and aramid polymer, which could potentially improve the interactions among the nanofibers for achieving better mechanical properties.

4.5 Summary and Conclusions

In order to fabricate a strong and stiff ANF-based film, different materials including polymers (PVA) and clay nanoparticles (MTM) were used via LBL assembly method to make nanocomposites with isotropic planar properties. However, owing to the lack of inter-macromolecular interactions, the initial ANF LBL films made were brittle and fragile. After carefully studying the nature of the Kevlar/DMSO solution and the effect of phosphoric acid and glutaraldehyde, an in-situ functionalization process was introduced to promote the bonding between the molecular chains. An improvement of both the stiffness and strength of the Kevlar LBL films was observed after the process. This ANF/PA/GA sample was also brittle, so it was used as building blocks with high stiffness and strength to bind with ductile PU/PAA layers. A hierarchical structure was created with “hard” and “soft” phases, and it yielded higher strain to failure. The mechanical properties of the ANF/PA/GA and the hierarchical ANF films were comparable to the ones of plain-woven Kevlar mat tested along the fiber axis.

Reference

[1] M. Yang, K. Cao, L. Sui,Y. Qi, J. Zhu, A. M. Waas, E. M. Arruda, J. Kieffer, M. D. Thouless, N. A. Kotov, "Dispersions of ANSs: A New Nanoscale Building Block," *ACS Nano* **2011**, Vol. 5, No. 9, pp. 6945–6954.

[2] Podsiadlo P. et al., "Can Nature's Design Be Improved Upon? High Strength, Transparent Nacre-Like Nanocomposites with Double Network of Sacrificial Cross Links ", *J. Phys. Chem.* **2008**, Vol. B112, pp. 14359-14363.

[3] G. Li, C. Zhang, Y. Wang, P. Li, Y. Yu, X. Jia, H. Liu, X. Yang, Z. Xue, S. Ryu, "Interface Correlation and Toughness Matching of Phosphoric Acid Functionalized Kevlar Fiber and Epoxy Matrix for Filament Winding Composites," *Compos. Sci. Technol.* **2008**, Vol. 68, pp. 3208-3214.

[4] S. Park, M. Seo, T. Ma, D. Lee, "Effect of Chemical Treatment of Kevlar Fibers on Mechanical Interfacial Properties of Composites," *J. Colloid Interface Sci.* **2002**, *Vol. 252,* pp. 249-255.

[5] R. R. Burch and L. E. Manring, "N-Alkylation and Hofmann Elimination from Thermal Decomposition of R4N+ Salts of Aromatic Polyamide Polyanions: Synthesis and Stereochemistry of N-Alkylated Aromatic Polyamides,"*Macromolecules* **1991**, Vol. 24, pp. 1731-1735.

[6] Andrews M. C. and Young R. J., "Analysis of the Deformation of Aramid Fibres and Composites Using Raman Spectroscopy," *J. Raman Spectrosc.* **1993**, Vol. 24, pp. 539-544.

[7] Washer G. et al, "Investigating the Effects of Aging on the Raman Scattering of Kevlar Strands," *Res. Nondestr. Eval.* **2008**, Vol. 19, pp. 144-163.

[8] Penn L. and Milanovich F., "Raman spectroscopy of Kevlar 49 fiber," *Polymer* **1979**, Vol. 20, pp. 31-36.

[9] Basiuk E. et al., "Poly (vinyl alcohol)/CNT composites: An effect of cross-linking with glutaraldehyde," *Superlattices Microstruct.* **2009**, Vol. 46, pp. 379-383.

[10] Jastrzebska M. et al., "Raman spectroscopic study of glutaraldehyde-stabilized collagen and pericardium tissue," *J. Biomater. Sci. Polymer Edn*, **2003**, Vol. 14, pp. 185-197.

[11] Martinelli A. et al., "Structural analysis of PVA-based proton conducting membranes," *Solid State Ionics* **2006**, Vol. 177, pp. 2431-2435.

[12**]** Podsiadlo P. et al., "LBL Assembled Laminates with Hierarchical Organization from Nano- to Microscale: High-Toughness Nanomaterials and Deformtaion Imagining," *ACS Nano* **2009**, Vol. 3, pp. 1564-1572.

[13] A. K. Kaushik , P. Podsiadlo, M. Qin, C. M. Shaw, A. M. Waas, N. A. Kotov, E. M. Arruda, "The Role of Nanoparticle Layer Separation in the Finite Deformation Response of Layered Polyurethane-Clay Nanocomposites," *Macromolecules* **2009**, Vol. 42, pp. 6588-6595.

Chapter 5

Reactive Aramid Nanostructures and PA/GA-Treated Aramid Networks

The field of advanced nanocomposite materials has had a fairly limited set of standard building blocks [1]. Many of them have low reactivity and limited variability. Stable dispersions of nanoscale aramid fibers with diameters between 3 and 30 nm were obtained by deprotonating macroscale, commercial Kevlar^{TM} yarns with potassium hydroxide in dimethyl sulfoxide, as discussed in Chapter 3. The aramid nanofibers (ANFs) were surface-treated with phosphoric acid (PA) to form two functionalized nanoscale aramid building block structures, depending on the extent of PA treatment, nanofibers and nanosheets. Next, the hydrolyzed nanostructures were crosslinked by glutaraldehyde (GA), and assembled into transversely isotropic networks in the form of thin films by vacuum-assisted filtration. The mechanical properties of the PA/GA treated nanostructured films, characterized by uniaxial tensile testing and dynamic mechanical analysis, were shown to be tuned by the amounts of PA and GA used during synthesis; and in some cases exceeded those of as-made ANF networks with no PA/GA treatment. Several complementary spectroscopy and microscopy tools were used to show that PA hydrolyzes aramid molecules to create useful functional groups for surface bonding and GA polymerizes the PA-hydrolyzed aramid nanostructures to tailor the network properties. By varying the PA/GA ratio and treatment extent, the nanostructures of the aramid building blocks, the morphologies of the networks and their macroscopic mechanical properties were all shown to vary in response. These results are the first demonstration of the possibility for aramid nanoscale fibers to form versatile nanosized building blocks that can then be crosslinked or conjugated to fabricate a wide variety of nanostructured aramid materials with tailorable mechanical properties [1].

5.1 Tuned Mechanical Properties of Aramid Nanostructured Networks

High surface-to-volume ratio aramid nanofibers (ANFs) obtained from macroscopic-scale Kevlar fibers after deprotonation of amide groups [2] can form the basis of a new generation of nanostructured materials. Here we demonstrate that the ANFs can be made chemically reactive with useful functional groups for bonding, and that these reactive aramid building blocks can be assembled into transversely isotropic networks with tailored nanostructures, morphologies and properties. Uniaxial tensile tests at room temperature and dynamic mechanical analyses (DMA) over a wide range of temperatures were used to characterize the mechanical properties of the aramid nanostructured networks. The reaction mechanisms during the phosphoric acid / glutaraldehyde (PA/GA) treatment of the Kevlar and the resultant bonding and morphology of the networks were explored using (i) Fourier-transform infrared spectroscopy (FTIR) to probe the chemical structures, (ii) transmission electron microscopy (TEM) to visualize the morphologies, and (iii) thermogravimetric analysis (TGA) to characterize the thermal properties of the nanostructured networks.

5.1.1 Synthesis

A family of aramid nanostructured films was prepared by reacting a Kevlar/potassium hydroxide (KOH)/dimethyl sulfoxide (DMSO) solution of ANFs with various amounts of PA and GA and PA/GA ratios. Also, an ANF network with no treatment was made as a comparison by adding water to the ANF solution, as discussed in Chapter 3. After chemical treatment, films were fabricated from the solution by vacuum-assisted filtration to obtain continuous and homogeneous structures. The nine different conditions used to prepare this family are shown in Table 5.1, along with optical micrographs of several of the resultant products shown in Figure 5.1. The surface and the cross-section of the filtered films with and without treatment were also observed in SEM, as shown in Figure 5.2. The surfaces of the films appeared smooth under 8000× magnification and at higher magnification, a densely packed structure was revealed. The cross section of the films showed a layered structure

created by the filtration process. The thickness of the films was uniform with a small variation of ~3%. It should be noted that it was not possible to form a continuous and homogeneous film with ANF solutions that had been exposed to PA but not to GA, or from solutions exposed to GA but not to PA, (Figure 2.a "No PA" and "No GA" samples).

100 mg of Kevlar in 100 mL DMSO	PA (mL)	GA (mL)	Thickness (μm)	Young's Modulus (GPa)	Yield Strength (MPa)	Strain Energy Density (MJ/m^3)
No Treatment	0	0	13 ± 0.7	7.1 ± 0.3	53 ± 2	8.0 ± 0.1
Sample A	0.25	1.5	20 ± 1.0	8.5 ± 0.3	83 ± 3	6.7 ± 1.8
Sample B	1.0	1.5	10 ± 0.6	7.4 ± 0.3	65 ± 3	6.9 ± 0.5
Sample C	1.0	1.0	25 ± 1.4	4.5 ± 0.1	34 ± 2	7.3 ± 0.4
Sample D	2.5	3.5	10 ± 0.7	2.2 ± 0.4	25 ± 4	5.1 ± 0.6
Sample E	2.5	3.0	20 ± 1.1	1.5 ± 0.4	13 ± 3	2.9 ± 0.4
No PA	0	1.5	-	-	-	-
No GA	0.25	0	-	-	-	-
Sample A+	0.25	3.5	10 ± 0.8	8.0 ± 0.9	82 ± 9	8.3 ± 1.9

Table 5.1 Aramid nanostructured networks assembled by vacuum-assisted filtration with varied PA and GA contents used in synthesis. ANF network with no treatment was made as a comparison. Continuous and homogenous networks were successfully obtained from each treatment, except for the samples made with just PA (No GA) or just GA (No PA).

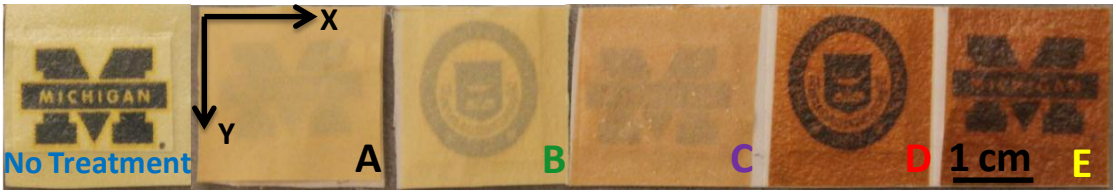

Figure 5.1 Optical pictures of aramid nanostructured networks assembled by vacuum-assisted filtration with varied PA and GA contents used in synthesis. The isotropy of the samples was checked by testing specimens in the X-Y plane with different orientations. The thickness of the samples refers to the out-of-plane dimension. The differences in the apparent transparency among samples may come from differences in the film thickness.

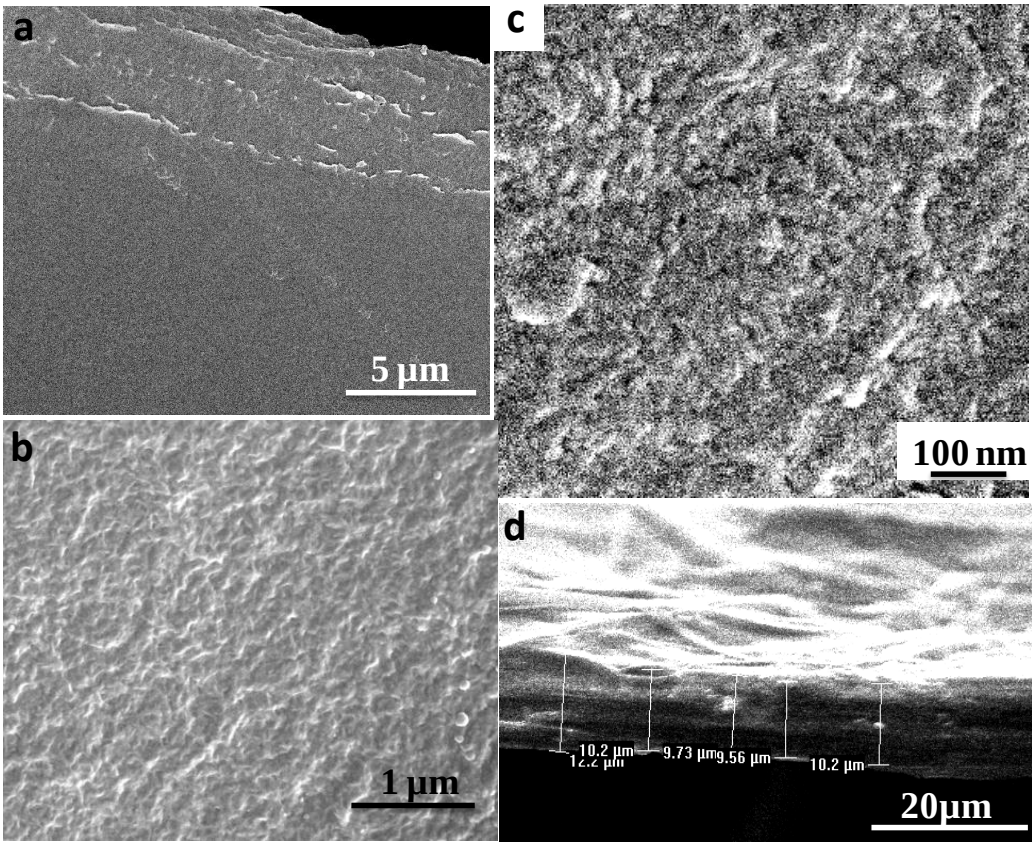

Figure 5.2 Scanning electron microscopy images of the filtered film with no treatment. The surface of the "No Treatment" film at different magnifications from small to large: a) a smooth surface away from the edge; b) and c) a densely bonded structure. d) The cross-section of the film. A layered structure was revealed. Similar surface and cross-sectional features of the PA/GA treated films were observed at these larger scales compared to TEM.

5.1.2 Unaixial Tensile Testing

The mechanical properties of the PA/GA treated films were tuned by varying the PA/GA ratio and the extent of the PA/GA treatment, as characterized by room-temperature uniaxial tensile testing at a strain rate of 0.005/s. Figure 5.3 illustrates how increased hydrolysis (more PA) tends to result in a more compliant material, while increased polymerization (more GA) tends to result in a stiffer material. A finite level of hydrolysis is required to provide active sites for the reaction with the GA, as the "No PA" sample does not form a continuous network. GA is not able to form bonds with the inert aramid unless water is used as in the "No Treatment" case, to re-protonate aramid macromolecules so that they form a film through hydrogen bonding. In particular, a limited amount of PA hydrolysis followed by reaction with GA (Samples A and B) produces networks that are stiffer than the untreated material. However, as can be seen by a comparison of the results for Samples A through E, increased levels of hydrolysis results in more compliant networks. This lower stiffness is not necessarily bad for design purposes, since it is also accompanied by an increase in damping properties, as discussed in the next section. While hydrolysis provides active sites for GA polymerization, these sites can also be saturated by adding excessive GA. Sample A+ had the same amount of hydrolysis as Sample A, but more GA, and the mechanical properties of the two samples were almost identical, which indicates that excess GA was not able to bond with the aramid nanostructures to further increase the network stiffness and strength. If the hydrolyzed sites are not saturated by GA, as for Sample C, the network is stiffened by the addition of GA (Sample B). A sample made with only PA but no GA ("No GA" sample in Figure 2.a) creates hydrolyzed aramid nanostructures but cannot form the continuous network required for characterization, without either water to form hydrogen bonding or GA to form covalent bonding.

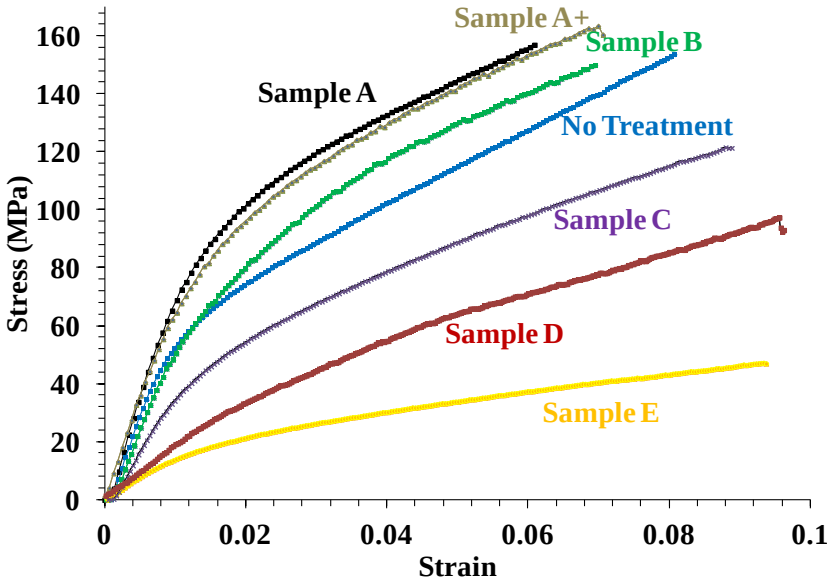

Figure 5.3 Stress-strain curves of aramid films, assembled by the filtration method, as functions of PA and GA contents characterized by uniaxial tensile tests at a strain rate of 0.005/s at room temperature. The mechanical properties of these nanostructured networks were tuned by the extent of PA/GA treatment. Multiple tests were performed on each sample until fracture, and consistent results were obtained.

The energy absorbing capability of the materials was estimated by calculating the strain-energy density at failure, i.e., the area under the stress-strain curve, for each sample. These values that are reported in Table 5.1 compare favorably with the strain-energy density of a traditional $0^0/90^0$ plain woven Kevlar mat. This mat had a strain to failure of less than 4.5%, and a strain energy density at a value of 5.7 ± 1.4 MJ/m^3.

5.1.3 Dynamic Mechanical Analysis

The storage modulus, a measure of the elasticity, and the loss tangent, a measure of the damping or energy dissipation, were determined as a function of temperature between −100 ºC and 180 ºC by measuring the stress response to a dynamic strain applied at 1 Hz (Figure 5.4a). Above about −70 ºC, the storage moduli of all the samples followed the same trend as in the tensile tests (Figure 5.3), with Sample A having the highest storage modulus and Sample E the lowest. Below this temperature, the untreated specimen had the lowest storage modulus and except for the most severely hydrolyzed specimen (Sample E), all treated specimens had storage moduli exceeding that of the untreated specimen at these low temperatures. The transition at −70 ºC is likely the critical temperature below which sliding motion between the smaller molecules from hydrolysis were frozen [3-5]. Many of the materials produced a pronounced peak in the loss tangent between −70 ºC and −50 ºC (Figure 5.4b), indicating a molecular transition and increased energy dissipation, which is useful for applications requiring damping such as blast loading. This loss tangent peak decreased from Sample E to the untreated specimen, with the largest peak corresponding to the specimen subjected to the greatest extent of hydrolysis (2.5 mL PA) and lower extent of GA treatment (3.0 mL of GA in Sample E vs. 3.5 mL of GA in Sample D). The drop in the peak of the loss tangent from Sample E to the untreated sample is consistent with the reduced hydrolysis and increased GA polymerization for a given amount of PA hydrolysis; both conditions that are consistent with a higher incidence of stiff, strong aramid backbone molecules.

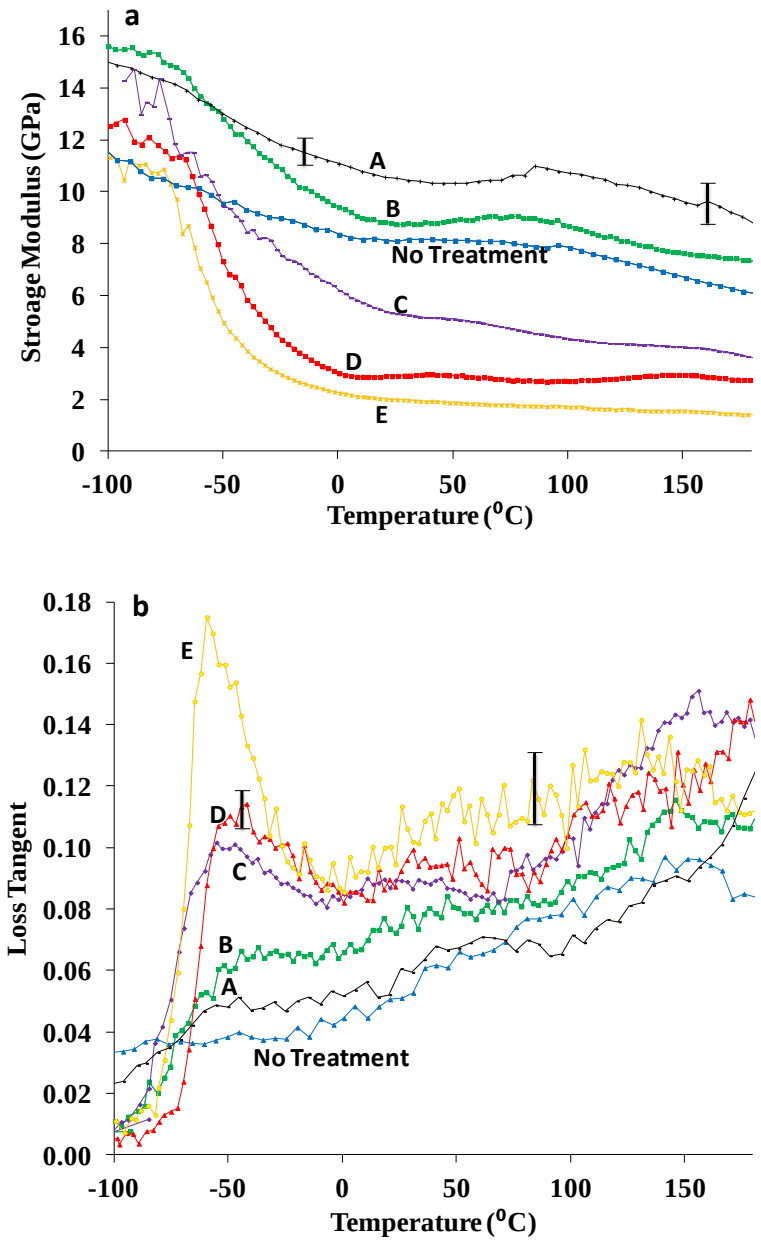

Figure 5.4 Storage modulus and loss tangent vs. temperature of the networks with and without PA/GA treatment at a frequency of 1Hz and a strain of 0.25 ± 0.10 %. At a given temperature above about −70 °C, the storage modulus increased with a reduced amount of PA or with an increased amount of GA, as also indicated by the uniaxial tension tests. The transition indicated by the peak in the loss-tangent curves at around −70 °C dropped from Sample E to the "No Treatment" sample.

5.2 Reaction Mechanisms of PA and GA

The nature of the functional groups created during the formation of the nanostructured networks by the PA/GA reaction was explored using various characterization techniques. This information was used to understand how the network properties might be tailored, and to develop a general strategy to modify the networks as a polymer matrix with different characteristics for use in nanocomposites. The chemical reactions with the PA and GA were first deduced by electron-pushing diagrams. FTIR was then used to verify the proposed changes by investigating the chemical structures of the network and of the liquid product left after vacuum filtration. The different network morphologies associated with different PA/GA treatments were observed using TEM. Finally, the thermal properties of the networks were characterized by TGA to provide additional insight into the treatment effects.

5.2.1 Proposed PA and GA Chemical Reactions

As aramid macromolecules are universally known for being inert, a mechanism was required to chemically modify them and allow them to react. Hydrolysis was chosen as a method to induce reactivity by the formation of amines and carboxylic acids. Figure 5.5 describes the hydrolysis reaction of aramid molecules in a Kevlar/KOH/DMSO solution. Hydrolysis involves the splitting of a chemical bond by the insertion of a water molecule. In the case of our work, an aramid-backbone amide N-C=O bond was split to create a primary amine ($-NH_2$) and a carboxylic acid (-COOH), as shown in the reaction mechanism (Figure 5.5), to allow for the subsequent condensation reaction with GA. The basic nature of the Kevlar/KOH/DMSO solution required a small amount of PA to first neutralize the base, which was a negligible amount, as just by a drop of acid, the solution changed color from red to yellow instantly and stayed yellow with more acid added. However, a stoichiometric excess of acid would be needed to have the forward reaction proceed at a higher rate than the reverse

one, and the hydrolyzed products are more stable in an acidic environment. Also, given that the hydrolysis reaction requires water, a small amount (5 ml) of water was added with PA to each sample. Initially, upon addition of acid and water to the Kevlar^{TM}/KOH/DMSO solution, some precipitates were observed to form owing to protonation of ANFs by water, as discussed in the companion paper.[17] However, as the reaction proceeded, the initial precipitates dissolved back into the DMSO owing to the increased polarity and smaller size of the hydrolyzed aramid chains.

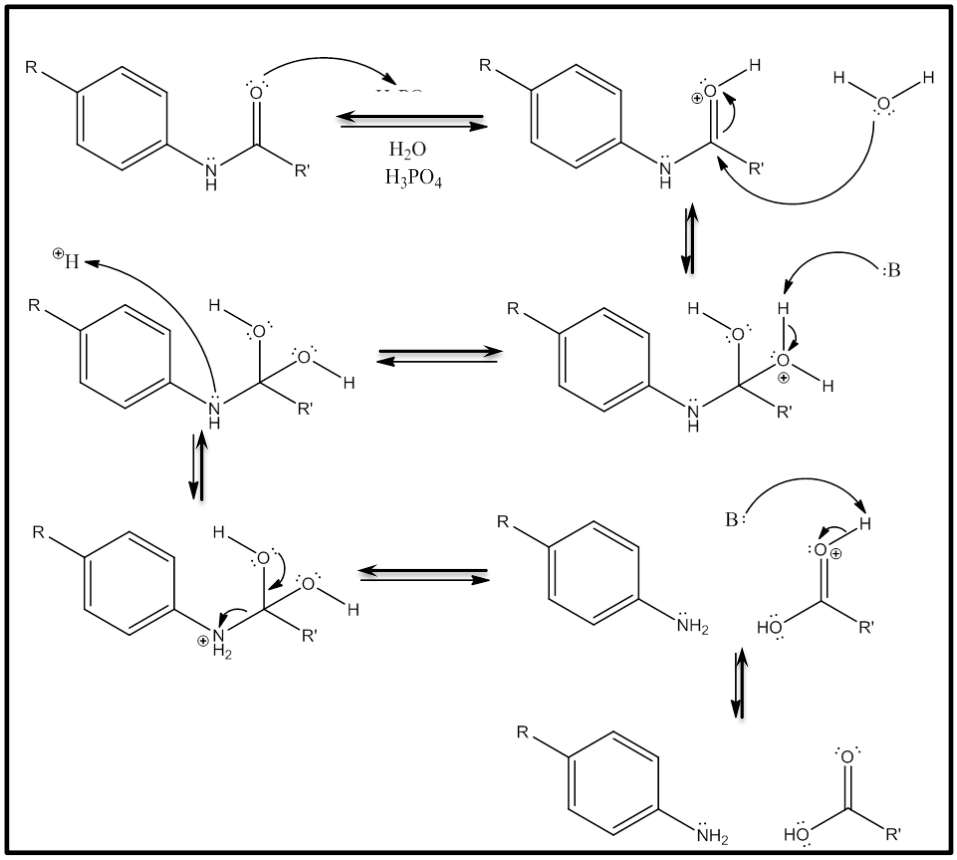

Figure 5.5 The proposed PA reaction mechanisms with aramid molecules: the acid-catalyzed hydrolysis of an aramid molecule using phosphoric acid. R and R'=aramid chain. B=any generic base.

Understanding the chemical process mechanism was of great interest to us to help in the development of a general strategy for modification and integration with other moieties to optimize stress transfer. The reactivity of the reaction products in Figure 5.5, a primary amine and a benzene-conjugated carboxylic acid per amide of the original aramid backbone molecule, is high. This is convenient for creating different types of covalent bonding to polymeric and inorganic components in nanocomposites. These two functional groups can then be reacted with crosslinking agents to connect the hydrolyzed aramid backbone molecules and to manipulate the polymer properties by adding new structures to the material: a synthetic strategy that, to our knowledge, has not been previously accomplished for aramids. In this work, we considered the specific example of GA as the crosslinking agent, although a di-aldehyde or di-ketone could be used to serve the same purpose. The GA that was added to the hydrolyzed solution was 50 wt% aqueous. Given that we only used a maximum of 3.5 ml of GA solution for 100 mL Kevlar/KOH/DMSO in any sample, very little water was added and thus its effect should be small. Furthermore, by the point GA was added, the aramid molecules should have already been hydrolyzed, making further hydrolysis less likely, especially as the GA condensation worked as a competing reaction. Figure 5.6 shows the reactive process responsible for the polymerization owing to the formation of di-imines as the primary amines from the hydrolytic product react with GA [6]. The reaction was heated to evaporate water to promote the forward reaction. The polymerization is complete as both aldehydes from each GA molecule undergo the reaction portrayed in Figure 5.6 and attach to an amine, joining two previously hydrolyzed aramid backbone molecules. GA was selected owing to its high reactivity and favorable structure, which provides two aldehydes to join two hydrolyzed aramid molecules.

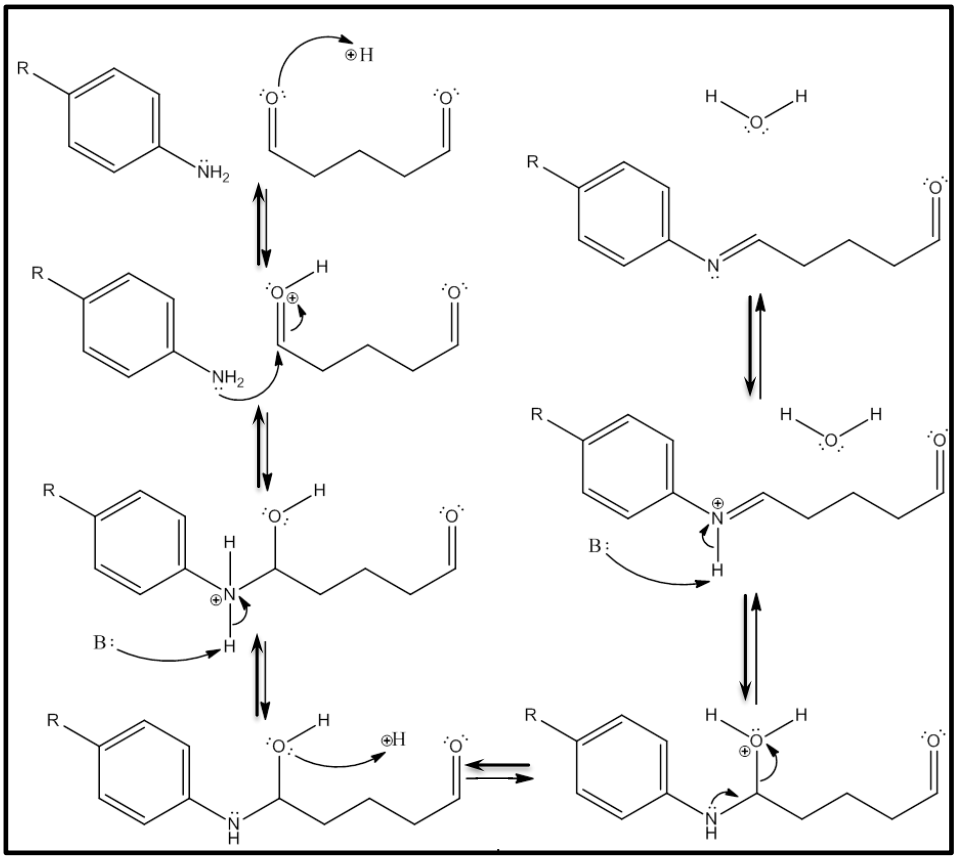

Figure 5.6 The proposed GA reaction mechanisms with aramid molecules: Condensation of a hydrolyzed aramid molecule with GA to produce di-imines. R and R'=aramid chain. B=any generic base.

Potassium cations from the Kevlar/KOH/DMSO solution for ANFs formation do not remain attached to aramid backbones, thus they will not affect the network properties. During the dissolution of Kevlar microfibers in KOH/DMSO solution, the amide N-H bonds of aramid backbones were deprotonated [2]. As a result, negatively charged nitrogen ions were formed. The positive potassium ions in KOH stabilize the N anions on aramid nanofibers in the red Kevlar/KOH/DMSO solution. Once acid was added to the solution to induce hydrolysis, and given how basic the nitrogen anions are in nature, potassium cations re-protonated almost immediately. The pH of the solution during the hydrolysis stage was measured and dropped from initially basic to neutral (pH was 7), a pH level at which aramid would not be deprotonated, hence no potassium cations remained attached to aramid

molecules. Furthermore, the water added during hydrolysis and GA polymerization or to make a “No Treatment” sample also immediately reprotonated aramids and washed potassium away from aramid backbone molecules.

5.2.2 Verification of PA and GA Chemical Reactions by FTIR

In order to verify the reaction mechanisms discussed above, FTIR was used to investigate both the solid and liquid products obtained after the vacuum filtration. The spectra performed on the networks showed clear changes associated with the PA/GA treatment when compared with the network that had no treatment, indicating that a reactive process had taken place. The results were in agreement with the mechanistic expectations discussed above, and confirmed the reactivity of the activated aramid nanostructures as convenient building blocks for nanocomposites.

FTIR spectroscopy of un-treated network shows the stretching frequency (3300 cm^{-1}, peak 1 in Figure 5.7a) of nitrogen-hydrogen bonds and the carboxyl groups (1650 cm^{-1}, peak 2 in Figure 4.a.1) in amides. Peaks 3 and 4 represent respectively the bending frequencies of the amides and the aromatic carbon-hydrogen bonds in the benzene rings [2, 7, 8]. The aramid chemical structure is shown schematically in Figure 5.8a.

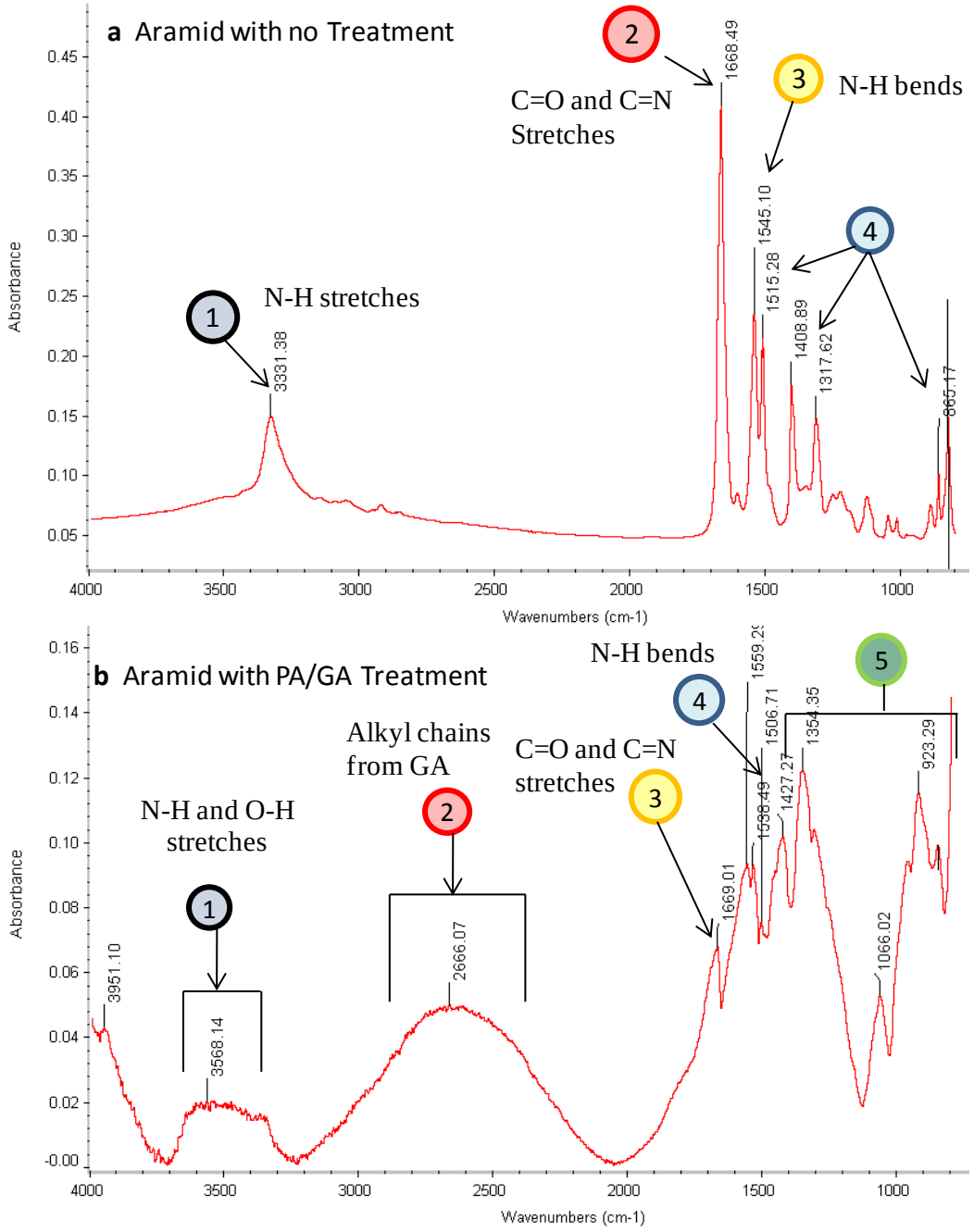

Figure 5.7 FTIR spectrum (a) of an ANF network (No Treatment), showing peaks at (1) 3331 cm^{-1}, (2) 1668 cm^{-1}, (3) 1545 cm^{-1} and (4) the fingerprint region. FTIR spectrum (b) of the synthetic products, nanostructured networks after PA/GA treatment (Samples A to E), showing peaks at (1) 3568 cm^{-1}, (2) 2666 cm^{-1}, (3) 1669 cm^{-1}, (4) 1559 cm^{-1}, and (5) the fingerprint region.

FTIR spectroscopy of the networks formed after PA/GA treatment (Figure 5.7b) was performed on Samples A to E following the chemical modification. The spectra showed splitting and broadening of the N-H and C=O stretches (peaks 1 and 2 in Figure 5.7a), and the appearance of a new alkyl peak in GA (peak 2 in Figure 5.7b). These verified that PA hydrolysis and GA condensation reactions occurred as proposed. The formation of many peaks around 3500 cm^{-1} (peak 1 in Figure 5.7b) can be rationalized by the presence of different oxygen-hydrogen and nitrogen-hydrogen bonds, such as those present in imines from a condensation reaction (Figure 5.6) and carboxylic acids from a hydrolysis reaction (Figure 5.5). The appearance of a broad peak around 2666 cm^{-1} (peak 2 in Figure 5.7b) is indicative of the presence of saturated alkyl chains from GA. The broadening and splitting of the signals around the carbonyl region (1700-1550 cm^{-1}, peaks 3 and 4 in Figure 5.7b) is a result of the presence of groups such as aldehydes, carboxylic acids and imines. Different extents of reaction, caused by adding different amount of PA and GA, yielded the same spectra, although variations in the peak absorbance and intensity could be observed in each sample. The relatively low wavenumbers of amide carboxyl stretching in the range 1700-1550 cm^{-1} can be rationalized partly by the expected high degree of conjugation due to the polymer structures: Carboxyl groups usually exhibit peaks in the range of 1850 – 1700 cm^{-1}, but as amides are naturally conjugated with relatively low frequencies, and as they were located next to aromatic rings in the aramid backbone molecules, there was increased electronic de-localization of the group that reduced the overall wavenumber of amide carboxyl stretching (peaks 3 in Figure 5.7b) [9].

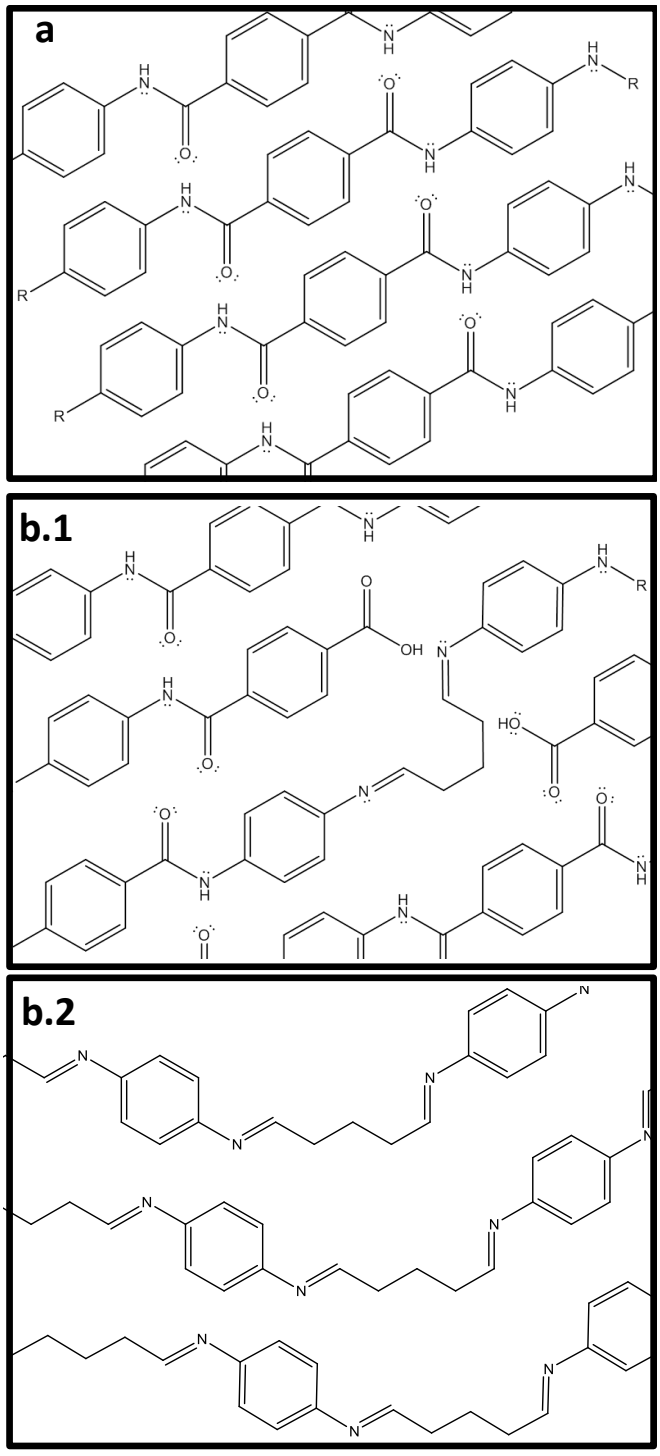

Figure 5.8 Chemical structures of (a) an ANF network (No Treatment) and (b) nanostructured networks after PA/GA treatment (Samples A to E). (b.1): Structure of an incompletely PA hydrolyzed network, as in Sample A. (b.2): Structure of fully hydrolyzed aramid backbone molecules subjected to a full condensation process with GA (Similar to Sample D).

From differences in the FTIR spectra between the specimens with and without treatment (Figures 5.7 a and b), especially the bands at ~3500 cm^{-1} (peak 1 in Figure 5.7b) for nitrogen-hydrogen bonds and at ~ 1700-1550 cm^{-1} (peak 3 in Figure 5.7b) for carboxylic acid, as well as the apparently high degree of peak overlap, it is clear that the solid product shares structural characteristics with aramids and the new alkyl group (peak 2 in Figure 5.7b) that formed in the reactive processes. Different levels of PA/GA treatment resulted in different degrees of the chemical-structural changes in the networks. The proposed structure (as in Sample A) after PA/GA treatment, using limited amounts of PA, is shown in Figure 5.8 b.2. Specimens (such as Sample D) subjected to an extensive PA hydrolysis and a full GA condensation reaction process would have the structure shown in Figure 4.b.3, where a large number of the aramid backbone molecules, including those in the surface and core regions of the nanofibers, have been hydrolyzed and substituted with C-C bonds. This difference in the level of structural changes of the solid products, *i.e*. Figure 5.8 b.1 and b.2, was difficult to discover via FTIR. Two distinct spectra, as shown in Figure 5.9, however, were observed for the liquid residues of the reactive processes after the solid parts had been filtered. They showed that reducing the amount of PA/GA reagents led to decreased hydrolysis, with correspondingly fewer carboxylic acids, i.e. the reaction product from hydrolyzation that can't be polymerized by GA remained in the liquid residues, as well as decreased GA polymerization, with larger amounts of the unreacted GA in the solution owing to fewer functional groups formed by hydrolysis for GA bonding. The FTIR analysis of the liquid residues also agreed well with the reaction mechanisms shown in Figures 5.5 and 5.6.

FTIR Spectroscopy of Liquid Products The extent of the PA/GA treatment affected the chemical-structural changes in the networks. The differences of the chemical structures in the solid products (Figure 5.8 b.1 and b.2) and intermediate structures were not strongly discoverable via FTIR. Two distinct spectra, however, were observed for the liquid residues of the reactive processes after the solid parts had been filtered. The spectrum in Figure 5.9a was consistently observed for reactive samples that had been prepared with a stoichiometric excess amount of PA and GA (Samples D and E, Figure 5.8 b.2). As a result, it is expected to represent a product solution with a large amount of terephthalic acid, formed due to extensive

hydrolysis of the aramid backbone molecules. This prediction is supported by a broad peak (peak 1 in Figure 5.9a, 3700-2500 cm^{-1}) which likely represents OH bonds and could arise from carboxylic acids and from water molecules that were formed during the condensation reaction. This result is consistent with the experimental condition of Samples D and E in which there were large amounts of excess GA and water in the liquid product. The set of peaks in the frequency range 1600-1400 cm^{-1} (peak 2 in Figure 5.9a) represents different resonance forms of the highly conjugated C=O bonds present within the liquid, corresponding to the C=O from carboxylic acid and excess aldehydes [9].

The second characteristic spectrum (Figure 5.9.b) was observed for the liquid residue from reactions produced with less than the stoichiometric amounts of the PA/GA reagents (Sample A, Figure 5.8.b.1). The broad frequency range 3700-2500 cm^{-1} (peak 1 in Figure 5.9.a) associated with OH bond stretching from carboxylic acid and water was not present; instead, there was a broad signal between 3500 and 2500 cm^{-1} (peak 1 in Figure 5.9.b), that can be explained as arising overlaps of several groups: 1) C-H alkyl bonds between the carbons in dissolved GA could produce the signal at around 3000 cm^{-1}; 2) OH bonds from carboxylic acid produced after hydrolysis in the range between 3000-2500 cm^{-1}; and 3) C-H bonds from the aldehydes in GA at 3023 and 2933 cm^{-1}. The signals at frequencies between 2500 and 2000 cm^{-1} (peak 2 in Figure 5.9.b) likely correspond to phosphine and phosphorous groups formed from phosphoric acid in the reactive medium [9]. This peak (peak 2 in Figure 5.9.b) was more distinct when less than stoichiometric amounts were used owing to the decreased amounts of carboxylic acids present in Samples A to C compared to previous examples (Samples D and E) that had an excess of the reagents.

It is clear that there were important differences between the FTIR spectra of the two types of liquid residue. Those differences indicate that reducing the amount of PA/GA reagents led to a decreased extent of hydrolysis, with correspondingly fewer OH groups being formed and larger amounts of unreacted GA remaining (Figure 5.9.b). Figure S4.b with less than stoichiometric amounts of PA/GA regents showed a larger amount of saturated carbon groups with signals around 3000 cm^{-1} and a considerably smaller amount of OH groups as evidenced by the peak shift away from 3500 cm^{-1} (peak 1 in Figure 5.9.b). In addition, the signal around 2350 cm^{-1} (peak 2 in Figure 5.9.b) indicated that the phosphine groups in the

second solution, produced with less than the stoichiometric quantities of the PA/GA reagents, were more prominent than in the first solution produced with excess reagents. This supports the claim that there were fewer OH groups present in the second solutions. Secondly, the C=O signal shifted to higher frequencies in the second solutions (peak 3 in Figure 5.9.b). This is an indication that the carboxylic groups were not as conjugated as those in the samples with excess reagents, so that the C=O groups probably came from GA rather than the aramid [9]. Those conclusions also support the proposed reaction mechanisms (Figures 5.5 and 5.6).

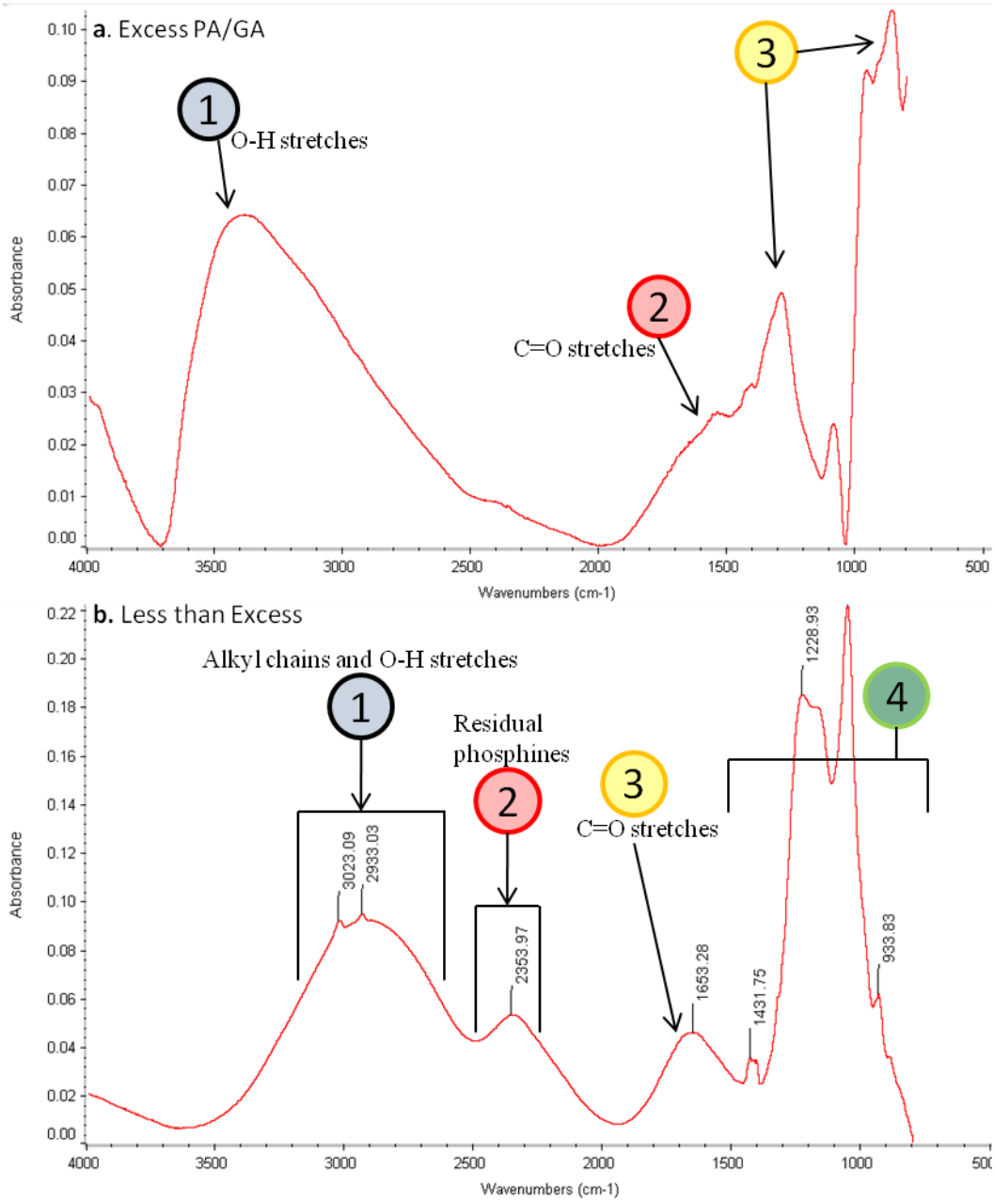

Figure 5.9 a) FTIR spectrum of the liquid product with extensive amounts of PA/GA reagents, showing peaks at 3350 cm^{-1}-(1), 1500 cm^{-1} (2), and the fingerprint region (3). b) FTIR spectrum of the liquid product with limited amounts of PA and GA, showing peaks at 3023 and 2993 cm^{-1}-(1), 2354 cm^{-1} (2), 1653 cm^{-1} (3), and the fingerprint region (4).

5.2.3 Effect of the PA/GA Treatment on the Aramid Building Block Morphology

The effect of the PA/GA treatments on the formation of the networks was visualized using TEM to observe the morphology of the solid product left behind after evaporation from a TEM grid (Figure 5.10). Figure 5.10.a shows the carbon-coated copper grid, and provides a reference for the subsequent images. Without any chemical treatment, the morphology in Figure 5.10.b consists of a randomly orientated network of nanofibers; the corresponding FTIR spectrum and chemical structure are shown in Figure 5.7a and 5.8a. The morphologies of Samples A and B after each treatment step are shown in Figure 5.10 (c to f). Figure 5.10.c shows that the nanofibers swelled in the presence of a limited amount of PA (*i.e.*, 0.25 mL of 85 wt% PA for 100 mg Kevlar). After PA-treatment, the hydrolyzed aramid molecules on nanofibers were polymerized by adding 1.5 mL of 50 wt% GA. This resulted in the morphology shown in Figure 5.10.d, with the corresponding chemical structure and FTIR spectrum shown in Figures 5.7b and 5.8 (b.1). Figure 5.10.e shows that when a larger amount of PA was used, as in Samples B and C (*e.g.*, 1 mL PA added to 100 mg Kevlar), nanosheets rather than nanofibers were formed after evaporation. These nanosheets were formed because the length of the nanofibers was reduced by extensive hydrolysis that broke down their aramid backbones. However, the addition of 1.5 mL 50 wt% GA to the solution resulted the restoration of a continuous network (Figure 5.10.f), as in Sample B, owing to the condensation reaction with GA which links the aramid building blocks and forms a network, as proposed in Figure 5.6. This process produced a chemical structure close to the one shown in Figure 5.8 (b.2).

This variation in morphology provides insight into the different mechanical properties of the PA/GA treated samples. The samples prepared with less PA (Samples A through C) and, hence, with less hydrolysis (*i.e.*, with more of the stiff aramid backbone molecules preserved), were stiffer than those that underwent more hydrolysis (Samples D and E). For the same extent of hydrolysis, the samples prepared with more GA (B and D), that underwent more polymerization of hydrolyzed chains, were stiffer than their counterparts (C and E). When the hydrolysis extent was low and GA content was high (*e.g.* Sample A), the GA polymerization served a crosslinking purpose to enhance the interactions between the ANFs. Although GA only has two functional groups per molecule, since hydrogen bonding keeps the rest of the

hydrolyzed molecules attached to the core of the nanofiber, the polymerization between the hydrolyzed molecules from two different ANFs can be treated as a crosslinker. The ideal mechanism for obtaining a higher stiffness or strength of a network would be to limit the extent of hydrolysis to the surfaces of the nanofibers to generate reactive functional groups for GA polymerization, but without reducing the stiffness of the nanofibers. Moreover, a crosslinking agent with more than two functional groups will be more effective than GA as it can crosslink hydrolyzed molecules from multiple ANFs together. The interactions between the nanofibers would be partially covalent with these treatment processes, compared with only secondary bonding between the nanofibers in the sample that undergoes no treatment.

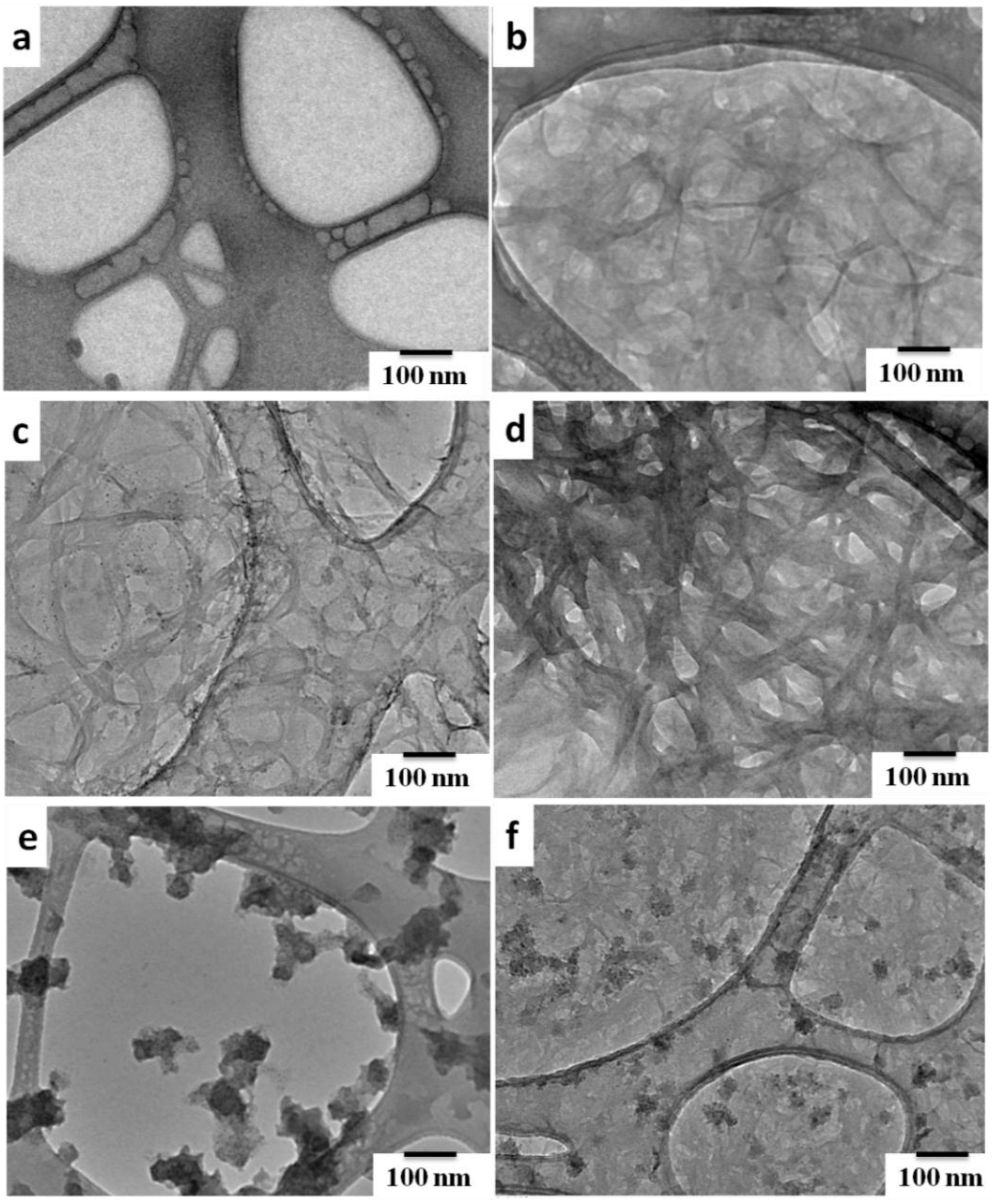

Figure 5.10 TEM images showing a) a carbon-coated copper grid used as the support for the TEM characterization of the networks, and the solid left after evaporation of the aramids dispersed in a DMSO solution b) with no treatment; c) after treatment of 0.25 mL PA for 100 mg Kevlar (as in Sample A but without GA treatment); d) after a further treatment with 1.5 mL GA (as in Sample A); e) after treatment of 1.0 mL PA for 100 mg Kevlar^{TM} (as in Samples B and C but without GA treatment): PA-catalyzed hydrolysis turning nanofibers into reactive nanoscale sheets; f) restored aramid network from nanosheets in (e) after a further treatment of 1.5 mL GA (as in Sample B).

DCE-Crosslinked ANF Network A DCE-crosslinked ANF Network was made by slowly adding 10 mL of 1, 2-Dichloroethene (anhydrous, 99.8%, Sigma-Aldrich) into the Kevlar/KOH/DMSO solution containing 100 mg Kevlar^{TM} while stirring over a period of two hours. The solid formed during this process was consolidated by the vacuum-assisted filtration method as discussed in Chapter 3. DCE has a similar molecular structure to GA, but owing to its functional groups, DCE can react with aramid molecules without hydrolysis, the reaction mechanism and the TEM image of which are shown in Figure 5.11 a and b. Figure 5.11c shows that the stiffness and yield strength of the DCE-crosslinked ANF network were slightly higher than those of Sample A. The similarity of the stiffness and yield strength between the two samples indicates that the DCE sample had a similar structure (Figure 5.11.e) as Sample A (Figure 5.8.b.1), although the DCE sample had a higher ultimate strength and strain at failure probably owing to fewer defects introduced during synthesis without the hydrolysis step. FTIR spectrum of the DCE-crosslinked sample shown in Figure 5.11d verified the reaction mechanism in Figure 5.11a, which results in a structure shown in Figure 5.11e. A DCE sample with 20 mL DCE (DCE-Kevlar+) was also made to insure that ANFs were crosslinked to the maximum amount, and this sample yielded identical mechanical properties as the sample with 10 mL DCE.

With this PA/GA treatment, Sample A is essentially the optimal condition for a high stiffness and yield strength, since the network consisted of all ANFs without nanosheets, and the amount of GA used was an excess (based on Sample A+), ensuring that the hydrolyzed sites on the ANFs were polymerized to the maximum extent. That Sample A is optimal in terms of stiffness and yield strength is also supported by the fact that its response is similar to that of an 1,2-Dichloroethene (DCE)-crosslinked ANF network, prepared by reacting DCE with ANFs in the Kevlar/KOH/DMSO solution at room temperature and consolidated by vacuum-assisted filtration. DCE is a crosslinker with a similar molecular structure to GA and it can crosslink aramid molecules without hydrolysis. Thus a DCE-crosslinked ANF network should be similar to the upper bound on the stiffness and yield strength that PA/GA treated samples can reach. DCE was not the focus in this work since it doesn't offer as much tailorability of the sample properties as PA/GA treatment does.

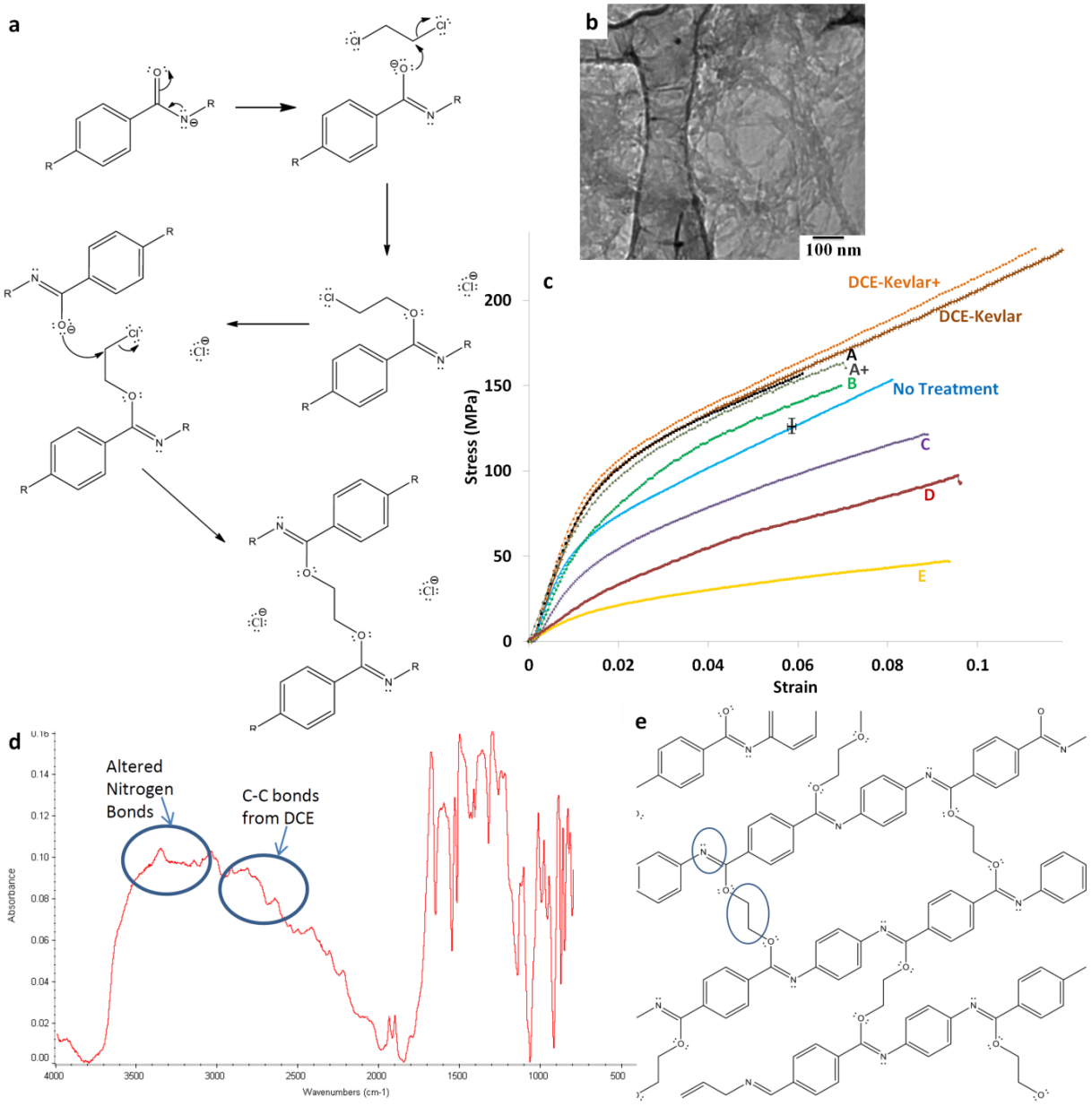

Figure 5.11. a) Reaction mechanism of DCE with aramid molecules. DCE crosslinks two aramid molecules with no hydrolysis. b) TEM image of the solid left after evaporation of the DCE-crosslinked ANF network dispersed in a DMSO solution. c) Stress strain curves of the PA/GA treated samples and the "No Treatment" sample from Figure 2.a compared with the DCE-crosslinked ANF networks, which have slightly higher stiffness and strength and greater ultimate strength and extensibility than those of Sample A. d) FTIR spectrum of the DCE-crosslinked networks and their corresponding structure (e).

5.3 Thermal Properties of Aramid Nanostructured Networks

TGA yielded two characteristic decomposition phenomena associated with the changes in the aramid nanostructured networks caused by PA hydrolysis and GA condensation. As indicated in Figure 5.12, between 5 and 20 wt % of the PA/GA-treated samples decomposed at ~ 150 ^{0}C. This decomposition came from the easily combustible aramid molecules with amide and carboxylic acid termination that resulted from hydrolysis (Figure 5.5), or from the dangling aliphatic chains that resulted from incomplete GA condensation (Figure 5.6). These were the smaller molecules introduced by the treatment, which resulted in a decrease of the network stiffness and strength but an increase in the damping. On the other hand, the PA/GA-treated networks showed significant improvements in high-temperature stability over the untreated one; for example, approximately 65 wt% of Sample A remained at the end of a temperature ramp test from 25 ^{0}C to 900 ^{0}C, while the sample with no treatment decomposed completely at ~ 800 ^{0}C with the same sample weight, heating rate and air purge rate. The high-temperature stability of the PA/GA-treated samples is anomalous. It may come from aliphatic chains of GA with both ends connected to aramid backbone molecules (Figure 5.8 4 b.1 and b.2), i.e. from a complete GA polymerization process. The treated networks were harder to decompose possibly owing to a stronger interaction between the aramid building blocks. These two decomposition phenomena are also supported by the differential weight fraction plots in Figure 5.12.b. Faster decreases in weight fraction at ~ 150 ^{0}C and slower decreases at ~ 560 ^{0}C were observed in the samples with more PA and less GA. This corresponds to an increase in the decomposition of the small PA-hydrolyzed molecules at ~ 150 ^{0}C and a decrease in the decomposition of GA-polymerized aramid backbone molecules at ~ 560 ^{0}C.

The thermal stability of the treated networks followed the same trend of their mechanical properties. It was observed that Samples D and E had decreased thermal stability compared to Samples A through C. It is conjectured that this was the result of a higher degree of hydrolysis in Sample D and E, which resulted in a higher content of easily decomposable amide and carboxylic acid terminated aramid molecules with smaller molecular sizes that

decomposed at ~ 150 ^{0}C (Figures 5.4, 5.5 and 5.10.e). The sample with no treatment had no hydrolyzation and thus had no apparent drop at ~ 150 ^{0}C. In addition, given the same amount of hydrolysis, Samples B and D had higher thermal stability than Samples C and E respectively, owing to a higher extent of GA polymerization in each pair, as complete GA polymerization promotes interaction between the nanostructures which was assumed to enhance thermal stability.

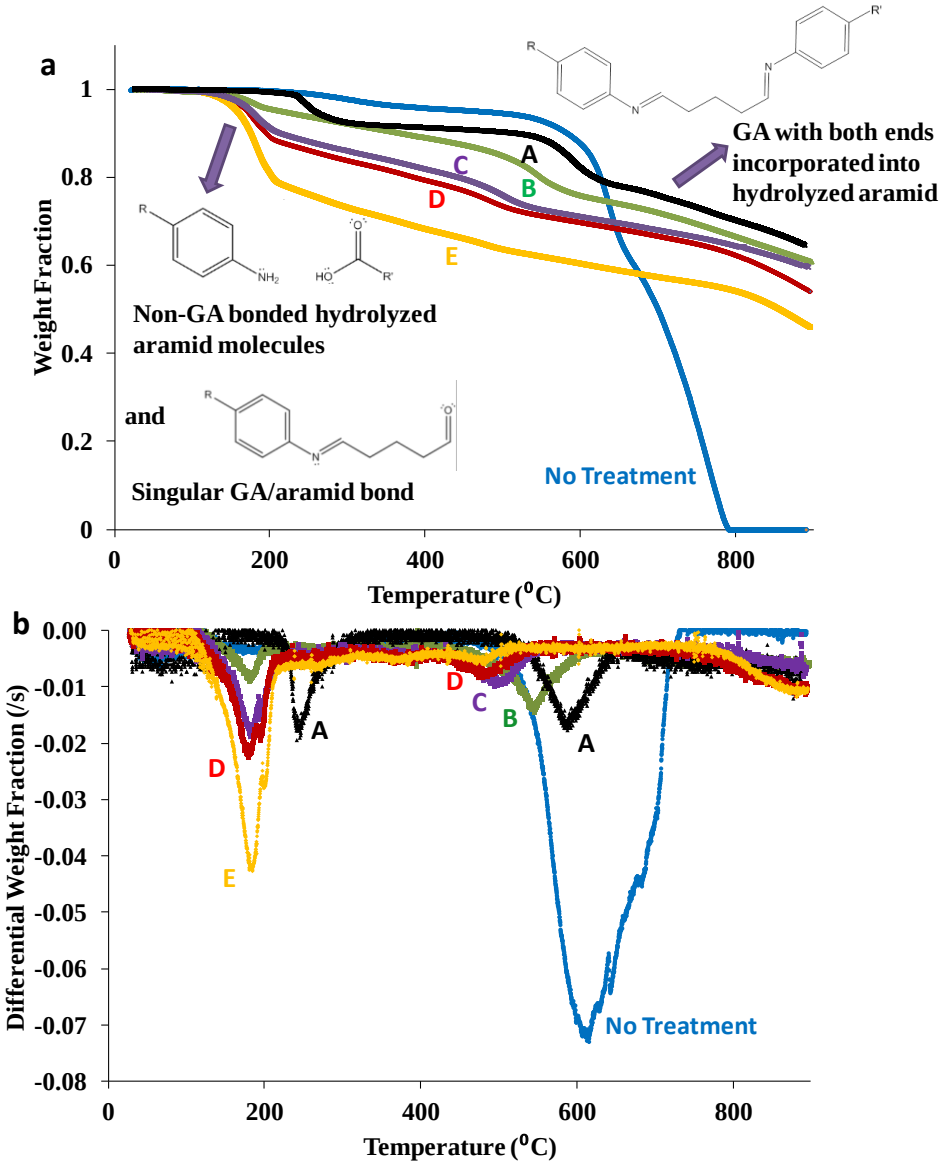

Figure 5.12 Characterization of the network thermal properties. a) Thermogravimetric response in air of the networks (with and without PA/GA treatment) at a temperature rise of 10 ^{o}C/min. The decomposition at ~150 ^{o}C was proposed to be smaller aramid nanostructures created by hydrolysis but without GA polymerization. The higher thermal stability at high

temperatures of the treated networks came from complete GA polymerization reactions, which improved the interactions between the aramid nanostructures in the networks. b) Rate of weight fraction decrease vs. temperature from the same TGA tests in (a). In the treated samples, more PA combined with less GA resulted in faster decomposition at ~150 ^{o}C and slower decomposition at ~560 ^{o}C. These results support the proposed reaction mechanisms and their effects on the network structures and properties.

Given the reaction mechanisms that occur, this PA/GA treatment method should also be effective for larger-scale aramid systems, and could be potentially used to increase the interactions between Kevlar microfibers or yarns and other materials, perhaps as a solution to the previous efforts for Kevlar fibers [10-16]. However, based on previous success at the nanoscale [17, 18], the control over the aramid nanoscale building blocks, through tailoring interfacial bonding of aramid nanostructures with a high surface to volume ratio, can be used to achieve even a higher goal of making superior nanocomposites, as one approach to make nanocomposites may start with a well-tailored nanostructured matrix with good properties. The PA/GA reaction mechanisms with aramids and the tailorability of the resultant nanostructured networks shown in this work provide possibilities for the subsequent design of a nanostructured polymer nanocomposite with excellent mechanical properties to resist extreme loading. In our on-going work, we have been incorporating inorganic materials as reinforcement phases, and have achieved good interfacial bonding with the matrices with treatment, indicating promises for prospective applications of the modified aramid nanomaterials in composites.

5.4 Summary and Conclusions

In this work, we functionalized Kevlar with PA/GA treatment to make reactive, nanoscale aramid building blocks of different morphologies, which were assembled into transversely isotropic films with controlled macroscopic properties. PA was used to hydrolyze high-aspect-ratio ANFs dispersed in a DMSO solution, and to make them chemically reactive. The acid-catalyzed hydrolysis produced functional groups available for surface bonding after breaking up some of the aramid backbone molecules. These hydrolyzed aramid nanostructures were then re-polymerized by a condensation reaction with GA. The PA-hydrolysis and GA-condensation steps were used to control the properties of the resultant networks by varying the extent of the reaction at each step. When a finite but limited amount of hydrolysis and a sufficient GA condensation were applied, we obtained aramid nanostructured networks with higher stiffness, yield strength and thermal stability than those of the ANF network with no treatment. Over-hydrolysis without GA condensation rendered ANFs into discrete nanosheets, which, after being re-polymerized by GA, yielded higher network damping for energy dissipation owing to sliding between the smaller molecules, but reduced the network stiffness and strength. Moreover, the transversely isotropic properties of the aramid nanostructured films extended the anisotropy of Kevlar microfiber, with its attractive properties only along one dimension, to a planar structure, which expanded its previous use as a reinforcement phase to a matrix structure. Understanding the important effects of the PA/GA treatment and how it affects the resultant nanostructures, network morphologies and macroscopic properties, is expected to provide a basis for future work on the optimization of high-performance aramid-based structures for advanced composites.

Reference

[1] K. Cao, C. Pons Siepermann, M. Yang, A. M. Waas, N. A. Kotov, M. D. Thouless, and E. M. Arruda, "Reactive Aramid Nanostructures as High-Performance Polymeric Building Blocks for Advanced Composites," *Adv. Funct. Mater.* **2013**, Vol. 23, pp. 2072–2080.

[2] M. Yang, K. Cao, L. Sui,Y. Qi, J. Zhu, A. M. Waas, E. M. Arruda, J. Kieffer, M. D. Thouless, N. A. Kotov, "Dispersions of ANSs: A New Nanoscale Building Block," *ACS Nano* **2011**, Vol. 5, No. 9, pp. 6945–6954.

[3] G. Williams, D. C. Watts, "Molecular motion in the glassy state. The effect of temperature and pressure on the dielectric β relaxation of polyvinyl chloride," *Trans. Faraday Soc.* **1971**, Vol. 67, pp.1971-1979.

[4] C. F. Hammer, "Cooperative Molecular Motion in Blends of Poly (vinyl chloride) with Ethylene-Vinyl Acetate Copolymers," *Macromolecules* **1971**, Vol. 4, No. 1, pp. 127-129.

[5] T. Kajiyama, K. Tanaka, A. Takahara, "Surface molecular motion of the monodisperse polystyrene films," *Macromolecules* **1997**, Vol. 30, pp. 280-285.

[6] H. S. Mansur, C. M. Sadahira, A. N. Souza, A. A.P. Mansur, "FTIR Spectroscopy Characterization of Poly(vinyl alcohol) Hydrogel with Different Hydrolysis Degree and Chemically Crosslinked with Glutaraldehyde," *Mater. Sci. Eng.* **2008**, Vol. C28, pp. 539-548.

[7] L. Penn, F. Milanovich, "Raman Spectroscopy of Kevlar 49 Fiber," *Polymer* **1979**, Vol. 20, 31-36.

[8] M. C. Andrews, R. J. Young, "Analysis of the Deformation of Aramid Fibres and Composites Using Raman Spectroscopy," *J. Raman Spectrosc.* **1993**, Vol. 24, pp. 539-544.

[9] C.P. Sherman Hsu, in: F. Settle (Ed.), Handbook of Instrumental Techniques for Analytical Chemistry, Prentice-Hall, NJ, **1997**, pp. 254.

[10] T. K. Lin, S. J. Wu, J. G. Lai, S. S. Shyu, "The Effect of Chemical Treatment on Reinforcement/Matrix Interaction in Kevlar-fiber/Bismaleimide Composites," *Compos. Sci. Technol.* **2000**, Vol. 60, pp. 1873-1878.

[11] F. Guo, Z. Zhang, W. Liu, F. Su, H. Zhang, "Effect of Plasma Treatment of Kevlar Fabric on the Tribological Behavior of Kevlar Fabric/Phenolic Composites," *Tribol. Int.* **2009**, Vol. 42, pp. 243-249.

[12] S. Saikrasun, T. Amornsakchai, C. Sirisinha, W. Meesiri, S. Bualek-Limcharoe, "Kevlar reinforcement of polyolefin-based thermoplastic elastomer," *Polymer* **1999**, Vol. 40, pp. 6437-6442.

[13] Z. Yu, A. Ait-Kadi, J. Brisson, "Nylon/Kevlar Composites. I: Mechanical Properties," *Polym. Eng. Sci.* **1991**, Vol. 31, No. 16.

[14] G. Li, C. Zhang, Y. Wang, P. Li, Y. Yu, X. Jia, H. Liu, X. Yang, Z. Xue, S. Ryu, "Interface Correlation and Toughness Matching of Phosphoric Acid Functionalized Kevlar Fiber and Epoxy Matrix for Filament Winding Composites," *Compos. Sci. Technol.* **2008**, Vol. 68, pp. 3208-3214.

[15] S. Park, M. Seo, T. Ma, D. Lee, "Effect of Chemical Treatment of Kevlar Fibers on Mechanical Interfacial Properties of Composites," *J. Colloid Interface Sci.* **2002**, Vol. 252, pp. 249-255.

[16] M. Rajabian, C. Dubois, "Polymerization Compounding of HDPE/Kevlar Composites. I. Morphology and Mechanical Properties," *Polym. Compos.* **2006**, Vol. 27, Issue 2, pp. 129-137.

[17] P. Podsiadlo, A. K. Kaushik, E. M. Arruda, A. M. Waas, B. S. Shim, J. Xu, H. Nandivada, B. G. Pumplin, J. Lahann, A. Ramamoorthy, N. A. Kotov, "Ultrastrong and Stiff Layered Polymer Nanocomposite," *Science* **2007**, Vol. 318, pp. 80-83.

[18] A. K. Kaushik , P. Podsiadlo, M. Qin, C. M. Shaw, A. M. Waas, N. A. Kotov, E. M. Arruda, "The Role of Nanoparticle Layer Separation in the Finite Deformation Response of Layered Polyurethane-Clay Nanocomposites," *Macromolecules* **2009**, Vol. 42, pp. 6588-6595.

Chapter 6

The Elasticity of Plain-Woven Kevlar Mat and ANF Networks at Low Strain Rates

Commercial Kevlar mats with 0° & 90° woven fibers, aramid nanofiber (ANF) films assembled by layer-by-layer (LBL) method, and ANF films assembled by vacuum-assisted filtration method are all aramid-fiber-based networks without any chemical treatment to change the bonding among fibers. Their mechanical properties characterized by low-strain-rate uniaxial tensile testing, however, differ from each other owing to the differences in fiber morphologies resulting from processing methods. In order to show how fiber geometry and orientation affect the elasticity (i.e. stiffness) of the aramid fiber based networks, the effective stiffness of a two dimensional planar network of Kevlar fibers were modeled through Mori-Tanaka methods.

Several analytical models of planar fiber networks exist. Wu and Dzenis [1] devised an analytical model that predicts effective stiffnesses of 2D straight fiber planar networks. The basic scheme of their analysis involved calculating the elastic moduli of fiber segments bounded by fiber-to-fiber contact. As a boundary condition, they assumed perfectly rigid bonding at fiber contacts. The effective stiffness of the network was determined by superposing the contributions of all the fiber segments while applying appropriate distribution functions to fiber segment orientation and length. They made several simplifying assumptions in their model; of note, they assumed uniform dispersion and orientation of fibers in space, linear elastic deformation and a matrix comprised of void space. Our analysis incorporates the added complexity that individual fibers are no longer straight, but markedly curved. Therefore, we have further simplified the overall analysis by neglecting fiber-to-fiber interactions.

In our analysis of random planar curved-fiber Kevlar networks, two approaches are pursued: In the first approach the fiber network is modeled in the fashion of Mori and Tanaka (M-T) [2]. For a composite with randomly orientated inclusions, the M-T model predicts the in-plane stiffness based on the aspect ratio of the inclusions, the volume fraction of the inclusions and the elastic properties of the matrix and the inclusions. The aspect ratio and the volume fraction of the nanofibers were determined experimentally in this work. The elastic properties of the matrix were chosen to be small so that the effect of the matrix was negligible. The effective stiffness of the inclusions was evaluated by calculating the effective stiffness of an axially-loaded misaligned fiber to account for the waviness of the nanofibers. An aramid nanofiber network with a 3D random fiber orientation is also modeled using the M-T model. A second modeling approach involves making an assumption regarding the collective geometry of the curved fibers. It is assumed that each fiber in the planar network has a sinusoidal geometry with an average ratio of amplitude to length derived from experimental SEM imagery. Following the technique of Christensen and Waals [3] to calculate the stiffness of blended bars with clamped boundary condition, the effective 2D elastic modulus is calculated for a distribution of randomly oriented curved fibers for two cases: one case in which the effective curved fiber elastic constants are assumed isotropic and another case in which they are assumed transversely isotropic.

6.1 The Mechanical Properties of Plain-Woven Kevlar Mat at a Low Strain Rate

The mechanical properties of commercial Kevlar mats with 0^{o} & 90^{o} plain woven fibers were characterized as a benchmark to compare with those of aramid networks. Both uniaxial tensile testing and biaxial tensile testing were conducted along the fiber axes of the mat at a displacement rate of 1 mm/s under room temperature. Figure 6.1 shows the stress-strain curves of two Kevlar samples from the uniaxial testing, conducted by applying tension

along the 90° fibers and with free ends for the 0° fibers. An average stiffness of 20.5 GPa was measured by this test. Figure 6.2 shows the stress-strain curves of one Kevlar sample from the plane strain testing, obtained by applying tension along the 90° fibers and constraining the 0° fibers. Although the fibers in the two directions were woven together and were in good contact during the testing, limited stress was measured along the 0° fibers direction, as shown in Figure 6.2b, indicating a stress condition similar to that of the uniaxial tensile testing.

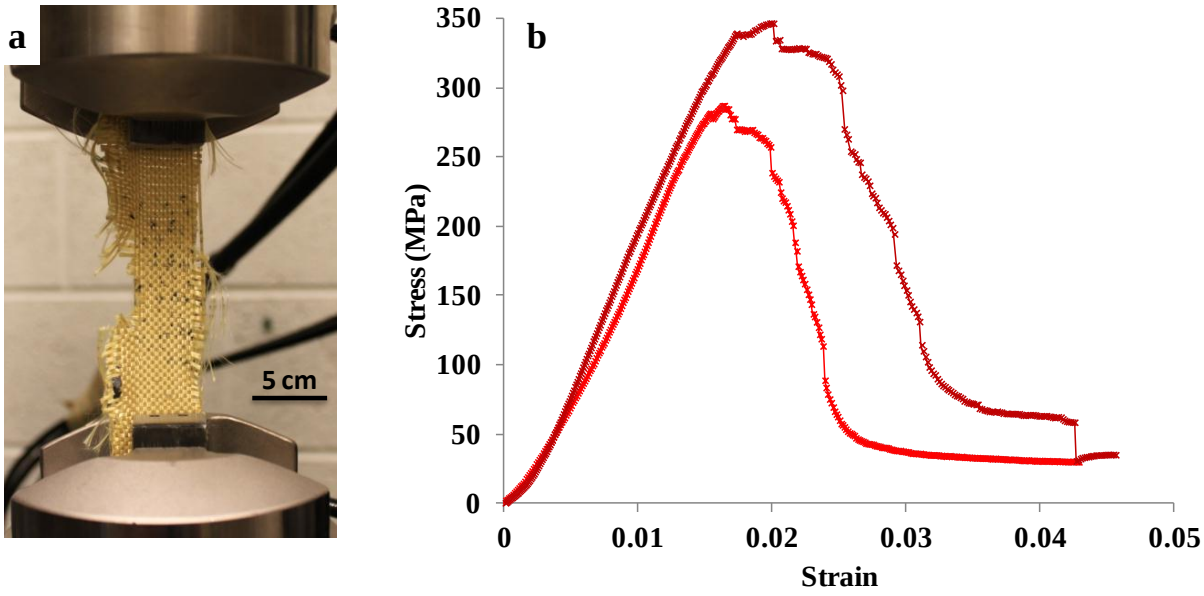

Figure 6.1 (a) Low strain rate uniaxial tensile testing on commercial Kevlar mats with 0° & 90° plain woven fibers. The tensile force was applied along the 90° fibers and the 0° fibers were free of external forces. (b) Stress-strain curves from the uniaxial testing on two Kevlar mat samples.

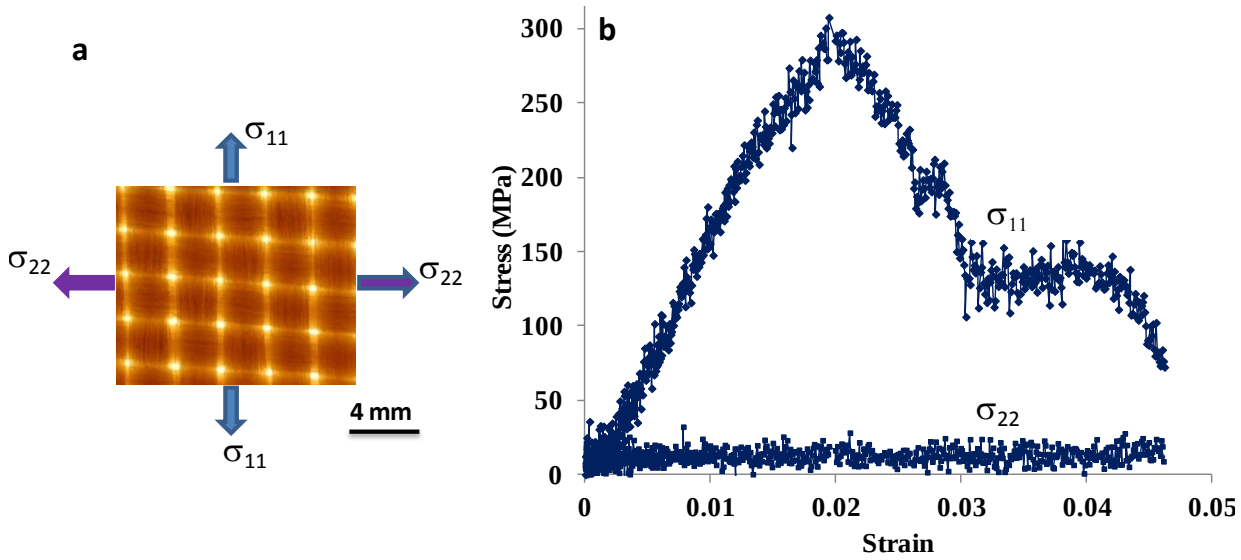

Figure 6.2 (a) Low strain rate tensile testing with a plane strain condition on commercial Kevlar mats with 0° & 90° plain woven fibers. The tensile force was applied along the 90° fiber direction and the 0° fibers were held in plane by grips. (b) Stress-strain curves of one Kevlar mat sample from the biaxial testing. The stress in the 0° (σ_{22}) fiber direction was negligible compared to that along the 90° fibers.

The mechanical properties characterized by the two testing methods revealed similar results, as shown in Figure 6.3. The measured high stiffness and strength of the mat come from the stretching along the fiber axis, and microscopically, the stretching of highly-aligned aramid macromolecules, as shown in Figure 6.4. The tests conducted on the samples, in this orientation, measured the strongest mechanical properties of the mat, compared to the stiffness and strength measured in any other direction. The anisotropy of the mechanical properties of the woven Kevlar mat compares unfavorably with the isotropy of the synthesized aramid nanostructured networks. Figure 6.4 also shows the failure mode of the Kevlar mat during the biaxial testing. Breaking of individual fibers occurred, which caused a gradual decrease of stress upon the initiation of fiber fracture.

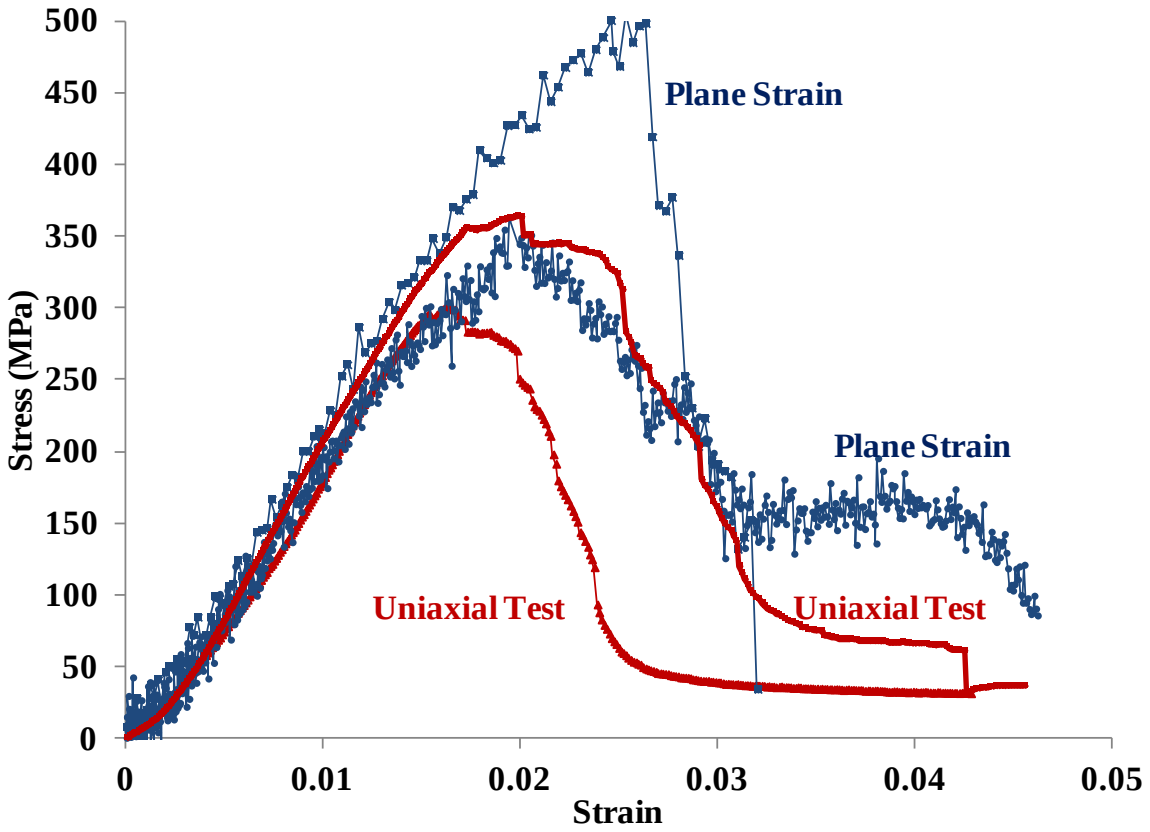

Figure 6.3 Stress strain curves from four Kevlar samples characterized by both plane strain and uniaxial tensile testing, showing similar results obtained from the two different testing methods.

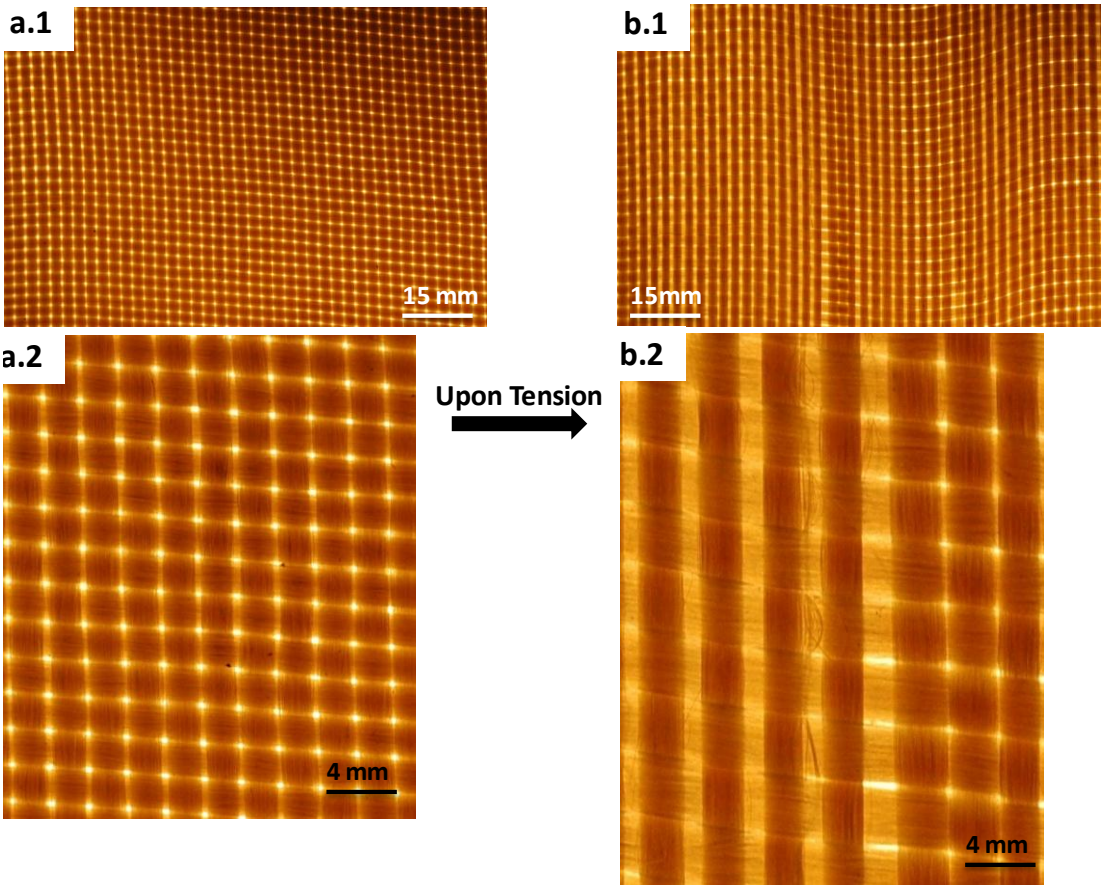

Figure 6.4 Optical images showing the failure mode of Kevlar mats during plane strain testing. (a) The Kevlar mat before any tension was applied. (a.2) is a close-up version of (a.1). (b) Upon applying tension on the 90^{o} fiber axis, the breaking of individual fibers occurred, resulting in a gradual decrease of stress until final failure of the mat.

6.2 Elasticity of a 2-D Randomly Oriented Nanofiber Network

A random network of Kevlar nanofibers is assembled via layer-by-layer assembly, (i.e. the ANF LBL film discussed in Chapter 4), which produces an amorphous dispersion of fibers in each layer. Investigation of the network microstructure indicates that it is composed of densely packed, curved nanofibers. Through scanning electronic microscopy (SEM) and transmission electronic microscopy (TEM), it is observed that the dispersion of nanofibers contains length distributions in the range of 5-10 μm and diameter distributions in the range of 3-30 nm. Results obtained from atomistic force microscopy (AFM) indicate similar fiber diameter distribution and morphology.

Here a micromechanics approach was adopted to determine the effective elastic moduli of a random network of ANFs in which the fibers assume a curved geometry. We investigate two methods of modeling effective representative volume elements (RVE) of the amorphous structure. In one method, we adopt an M-T model with large fiber aspect ratios. In another method, we define a single fiber RVE in which the fiber geometry is represented by a sinusoidal wave function. Constitutive relations are derived for the individual RVEs and, from these, an effective constitutive relation for the entire network. Where applicable, experimental data collected from tension tests of Kevlar network material is used as input for calculations of elastic properties. In both methods, simplifying assumptions have been made: (1) deformations of the fibers as well as of the random network are linear elastic and (2) interfacial effects of fibers in direct contact are neglected.

6.2.1 Mori-Tanaka Model

The M-T model is a proven means of analyzing micromechanical behavior in composite structures that contain inclusions of various geometries as illustrated in Figure 6.5. It provides a method of calculating the average internal stress in the matrix of a material containing inclusions with different aspect ratios [2]. The model was modified by Tandon and Weng by combining Eshelby's solution with Mori-Tanaka's average stress to obtain a closed

form solution for finite concentrations of ellipsoidal inclusions over a large range of aspect ratios [4, 5]. Through Tandon and Weng's method, the five independent elastic constants for an inclusion-reinforced transversely isotropic composite in terms of the inclusion concentration, inclusion properties and matrix properties can be obtained [5]. In this work, the M-T model is implemented through the method provided by Tandon and Weng to predict the elastic properties of aramid nanofiber networks with curled fiber geometries [6].

The fundamental idea of the M-T model is to consider the variation of average stress in the matrix due to the presence of inclusions [4]. To determine the effect of the introduction of inclusions, an identically shaped matrix is considered for comparison, as shown in Figure 6.5 and Equation 6.1 [6]. A uniform stress $\overline{\sigma_{ij}}$ is prescribed as a surface traction on the boundary of the composite and the matrix. Denote the elastic moduli tensor of the composite by C_{ijkl} and strains of the composite $\overline{\varepsilon_{kl}}$ and of the comparison matrix $C^{\circ}_{ijkl}$and ε°_{kl}. The presence of inclusions introduces a perturbation strain $\widetilde{\varepsilon_{kl}}$ in the matrix to redistribute the stress, $\overline{\sigma_{ij}} + \widetilde{\sigma_{ij}}$ (Eqn. 6.2). The perturbation strain can be calculated by Eshelby's S_{ijkl} tensor, which is dependent on the matrix's Poisson's ratio and the aspect ratio of the inclusion (length/diameter) [6].

$$\overline{\sigma_{ij}} = C_{ijkl}\,\overline{\varepsilon_{kl}} \qquad \overline{\sigma_{ij}} = C^{\circ}_{ijkl}\varepsilon^{\circ}_{kl} \qquad \textbf{(Eqn. 6.1)}$$

$$\overline{\sigma_{ij}} + \widetilde{\sigma_{ij}} = C^{\circ}_{ijkl}(\varepsilon^{\circ}_{kl} + \widetilde{\varepsilon_{kl}}) \qquad \textbf{(Eqn. 6.2)}$$

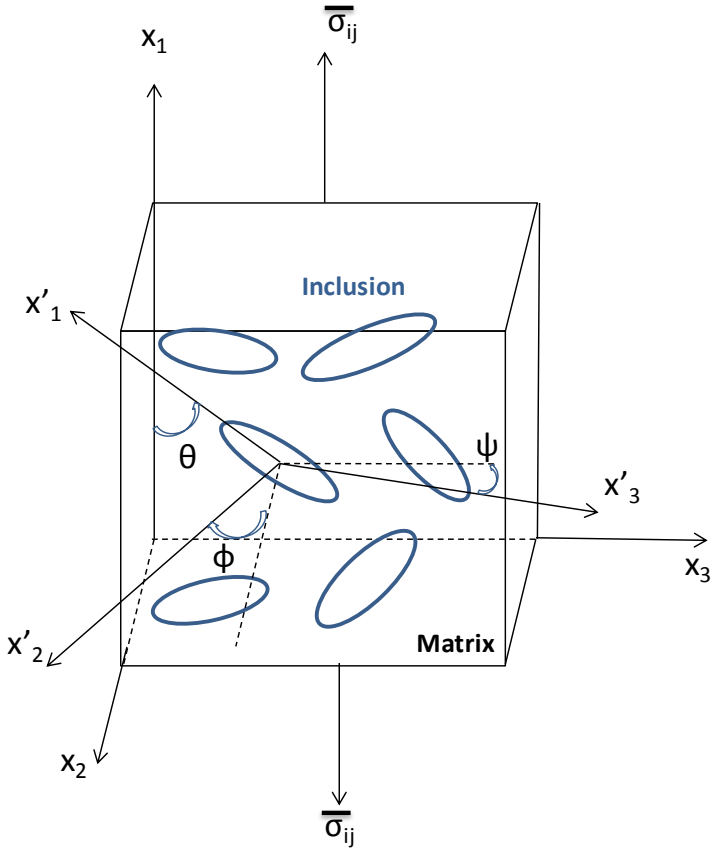

Figure 6.5 The composite with randomly oriented inclusions in a matrix under a stress field. Figure reproduced from Tandon et al., 1986 [6**].**

6.2.2 Microstructure

The microstructure of the Kevlar nanofiber network was studied via atomic force microscopy (AFM), scanning electron microscopy (SEM) and transmission electron microscopy (TEM). The microstructure of the network is comprised of curved nanofibers with a two-dimensional random orientation.

Figure 6.6 shows SEM images of three Kevlar nanofiber networks; the networks vary in initial concentration of Kevlar fibers suspended in solution prior to deposition on a glass substrate. The design of experiment focused on characterizing the curviness and dimension of the Kevlar nanofibers comprising each network. At high fiber concentrations (Figure 6.6c) it is difficult to observe single fiber geometries due to extensive agglomeration. Thus a diluted

sample (Figure 6.6a) was prepared. SEM images indicate that there is a variation of the fiber waviness (or curvature) in the network; the overall structure of the fiber network is amorphous.

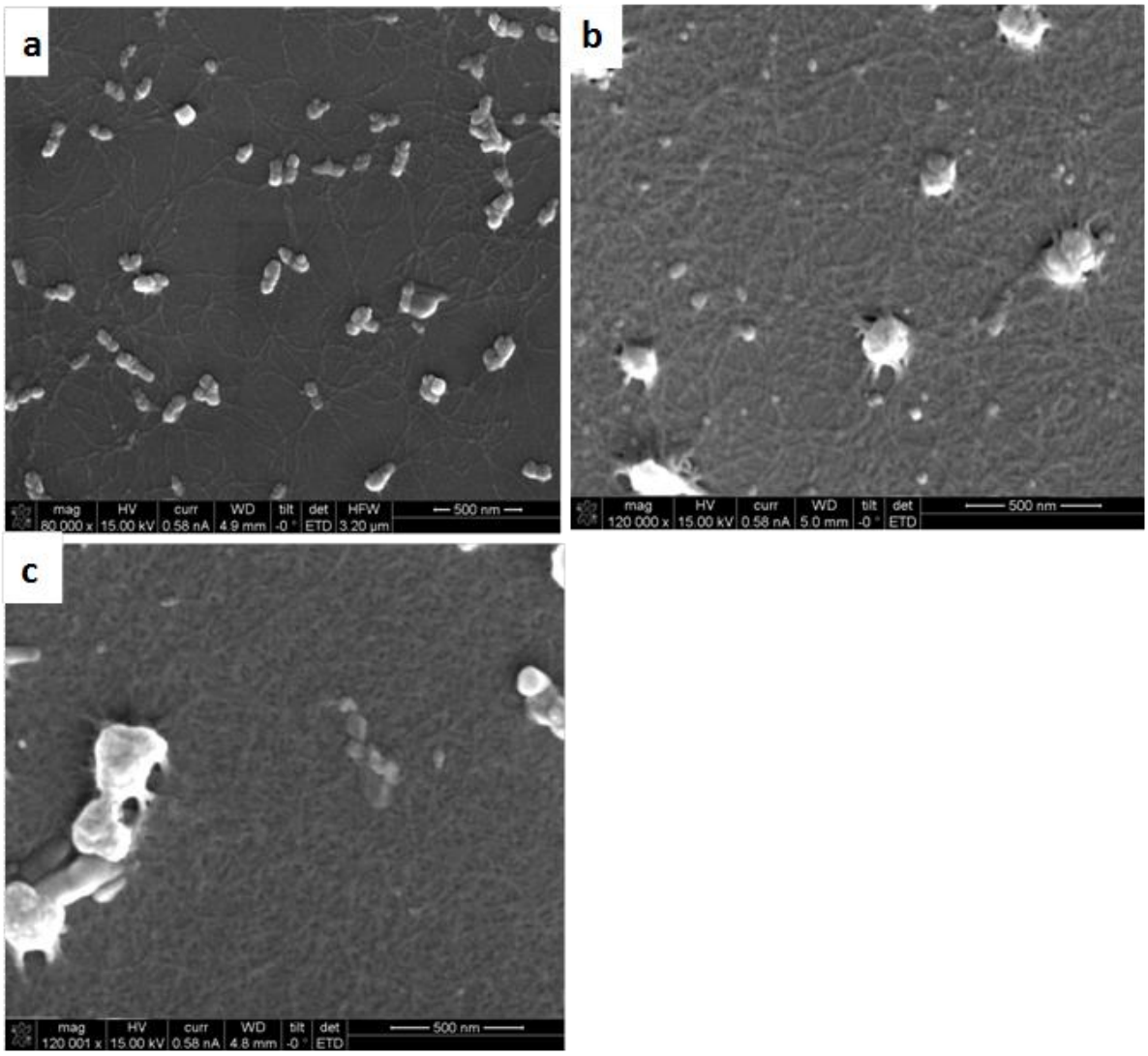

Figure 6.6 SEM images of Kevlar nanofiber networks of varying concentration. The concentration increases from image a) to c) with image a) being the most dilute. It can be observed that there exists a variation in the nanofiber waviness (shape). The amorphous distribution of the nanofibers can also be observed, which is an indication of a 2-D random orientation of the nanofibers. Figures adapted from Yang et al., 2011 [7].

Similar features were observed via TEM (Figure 6.7), where a variation of nanofiber waviness was observed for a random 2D orientation of the nanofibers. Through analysis of TEM imagery, it was determined that the Kevlar network contained length distributions in the range of 5-10 μm and diameter distributions in the range of 3-30 nm. This result was further supported by measurements via AFM, where similar fiber dimensions and morphology were observed (Figure 6.8).

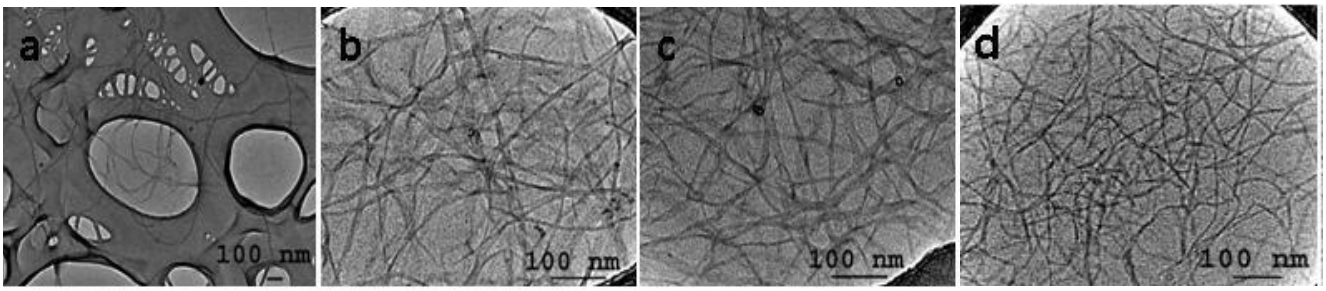

Figure 6.7 TEM images of nanofibers with concentration increasing from a) to d). Figures adapted from Yang et al 2011 [7].

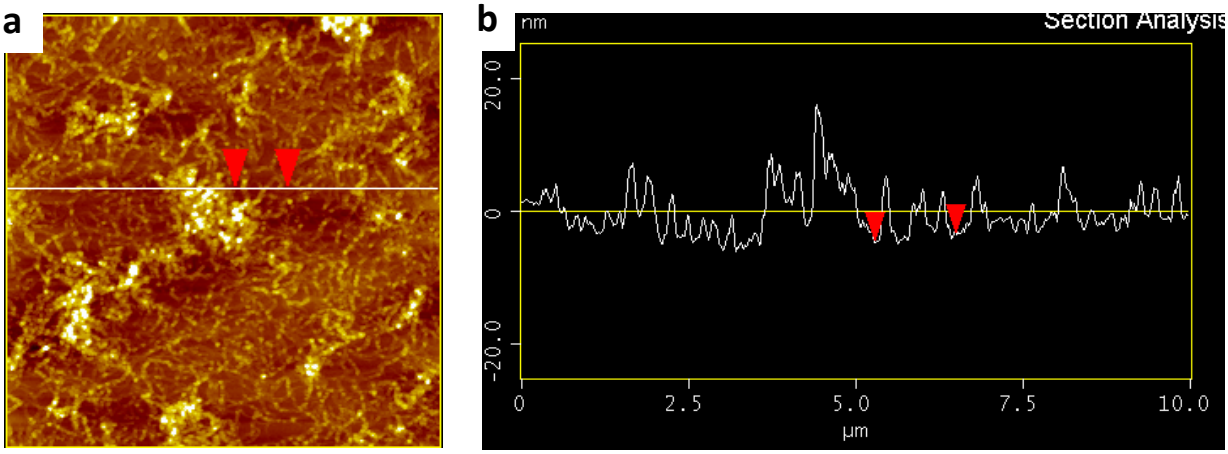

Figure 6.8 AFM image (a) and its corresponding dimension profile (b) on nanofibers.The dimension profile (b) is a plot of the height measured along a selected line in (a). The two arrows in (a) correspond to the same arrows in (b).

As will be further discussed in the next section, in constructing an analytical micromechanics model of sinusoidal curved fibers it is necessary to characterize the relationship between fiber length and amplitude. In Figure 6.9, length-to-amplitude measurements were calculated for several randomly sampled fibers. The average fiber length and amplitude attained from this data are used in computations of effective curved fiber elastic properties.

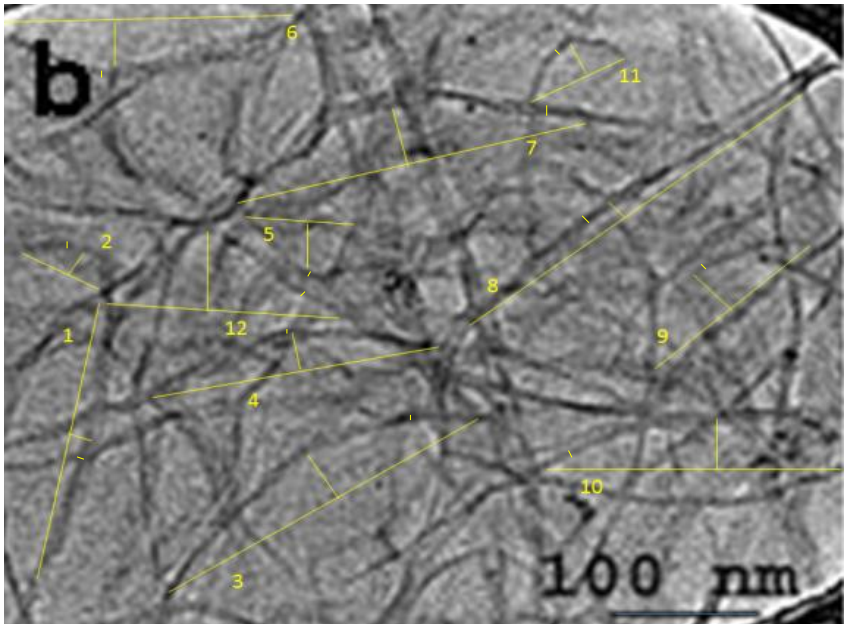

Fiber	Length (nm)	Amplitude (nm)	Diameter (nm)
1	422.7	16.7	4.8
2	110.7	16.7	4.8
3	444.0	33.3	3.6
4	433.3	28.0	3.1
5	156.0	33.3	3.8
6	433.3	33.3	4.7
7	133.3	22.0	7.1
8	477.3	11.3	6.4
9	222.7	38.7	4.7
10	422.7	28.0	5.3
11	500.0	44.7	4.7
12	333.3	65.3	4.3
Average	340.8	30.9	4.8

Figure 6.9 TEM micrograph of a random Kevlar nanofiber network. The amplitudes, wavelengths (half wavelength of a sinusoidal shape) and diameters of the nanofibers were measured for the twelve randomly sampled fibers indicated in the micrograph. Numerical data and averages are included in the table. Figure adapted from Yang et al., 2011 [7].

6.2.3 Density

The density of the LBL film was determined from the sample weight measured on a microbalance scale and volume obtained from dimension measurements in SEM. The density of the Kevlar nanofiber network was determined to be 1.23 g/cm^3, which is less than that of a fiber (1.44 g/cm^3). This gives an idea of void fraction or effective volume percent of the nanofiber due to the LBL assembly process. Here the volume fraction of the Kevlar nanofiber was chosen to be 85% from the density ratio (=1.23/1.44).

6.2.4 Elasticity of ANF LBL Network: Mori-Tanaka Method

In order to use the M-T model to calculate the in-plane stiffness (E_{11}) of the nanofiber network, several material parameters were chosen carefully to obtain the prediction for a microstructure described above. The aspect ratio was chosen to be 1000 for a length/diameter ratio of 5μm/5nm. The inclusion (ANFs) and the matrix (not present in ANF networks) are assumed to be linearly isotropic and perfectly bonded for the derivation of effective moduli by the M-T model; thus only two material elastic properties, Young's modulus and Poisson's ratio, were considered. The matrix modulus was set low, E_0=0.0005 GPa, to minimize the matrix effect. It can be shown that Poisson's ratio of the inclusion or the matrix doesn't have a large effect on the in-plane stiffness (E_{11}) by comparing E_{11} obtained from two sets of Poisson's ratio for E_i=85 GPa and E_0=0.0005 GPa (Figure 6.10). Thus, the parameters of interest are the matrix stiffness and the Young's Modulus of the effective nanofibers.

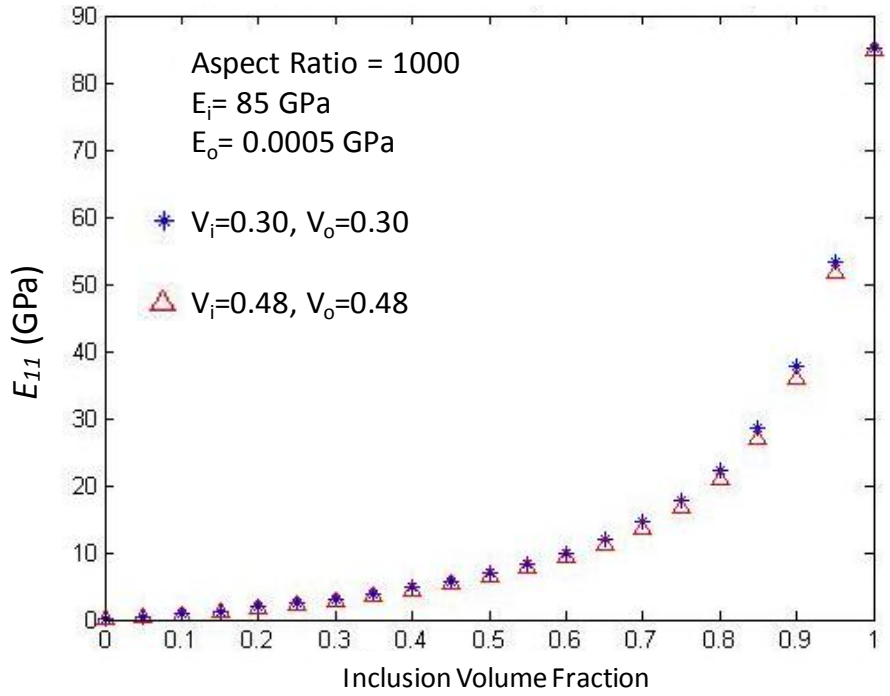

Figure 6.10 The effect of Poisson's ratio proved to be small by comparing E_{11} from two different sets of Poisson's ratios.

The effective stiffness of the curved Kevlar nanofibers was determined by considering the response of an axially loaded misaligned fiber of uniform cross sectional area with original stiffness E_f (without the curvature). The axial compliance of the misaligned fiber was derived for a clamped-clamped boundary condition at the two free ends [8], which is simplified and shown in Eqn. 6.3, where A_0 is the amplitude of the curvature and r is the radius of the nanofibers.

$$\frac{E_{effective}}{E_f} = \frac{1}{1+\frac{2A_0^2}{r^2}} \qquad \textbf{(Eqn. 6.3)}$$

From the study of microstructure, A_0/r=1.27 which yields a ratio $E_{effective}/E_f$ of 23.53%. This results in $E_{effective}$= 20 GPa for E_f= 85 GPa. For any value of Poisson's ratio and using this stiffness in the M-T model and an effective fiber volume fraction of 0.85, the resulting stiffness obtained was 13 GPa, as shown in Figure 6.11.

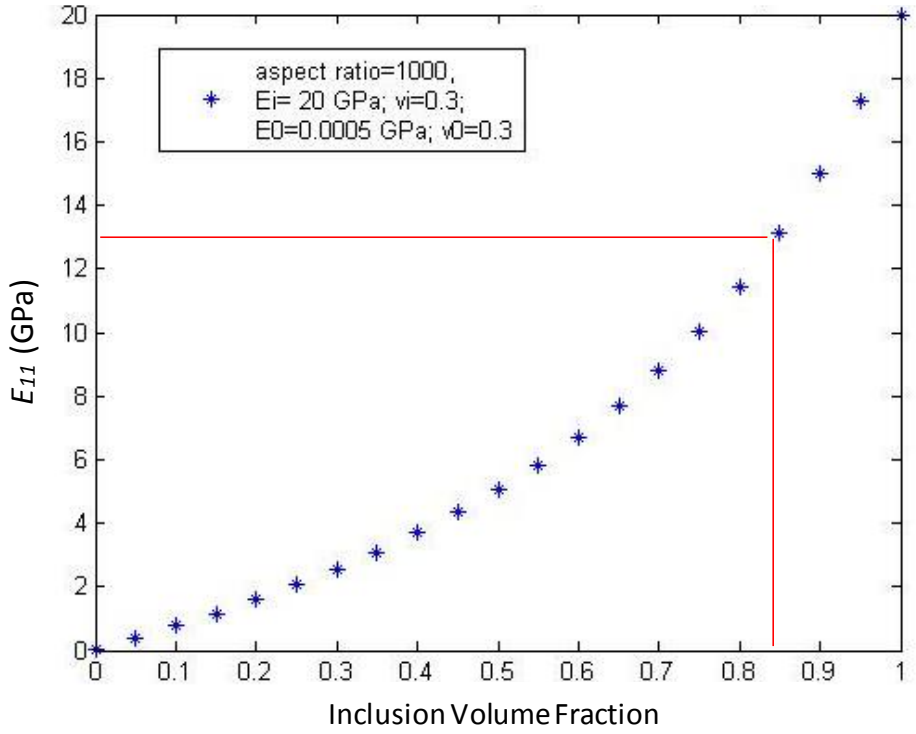

Figure 6.11 For any value of Poisson's ratio and based on $E_{effective}$ of 20 GPa and an effective density of 85 %, E_{11} was predicted to be 13 GPa by M-T model for Kevlar nanofiber LBL network.

6.2.5 Elasticity of ANF LBL Network: Single Sinusoidal Fiber Representative Volume Element

Rai, Rogers and Crane [9] devised an analytical model to determine the effective axial stiffness of a curved fiber composite by defining a function that represents the tangential orientation of each segment of sinusoidal fiber geometry over the course of its length. In our analyses of Kevlar fiber networks, we adopted this curved fiber model under the assumption that, on average, individual fibers assumed sinusoidal geometries, as shown in Figure 6.12. The fiber geometry is governed by Equation 6.4:

$$y = A \sin\left(\frac{2\pi x}{L}\right) \qquad \textbf{(Eqn. 6.4)}$$

where $\boldsymbol{A}$ is the wave amplitude and $\boldsymbol{L}$ is the wavelength. By taking the derivative y with respect to x and equating it to $\tan\theta$, the angle of deflection of a sinusoidal fiber is expressed as a function of distance along the length of the fiber:

$$\theta(x) = \tan^{-1}\left[\left(\frac{2\pi A}{L}\right)\cos\left(\frac{2\pi x}{L}\right)\right] \qquad \textbf{(Eqn. 6.5)}$$

Since the values of $\theta(x)$ change for changes in the ratio $\frac{A}{L}$, *it* is necessary to identify an amplitude/length ratio that best characterizes the curvature of the Kevlar fiber constituents of our random fiber network. Recall that average fiber lengths and amplitudes were calculated from random measurements taken on an SEM micrograph of a 2D planar Kevlar network as depicted (Figure 6.9). Half wavelengths and wave amplitudes were measured for a random sampling of sinusoidal geometry Kevlar fibers, from which an average full wavelength of 341 nm and average amplitude of 40 nm were calculated.

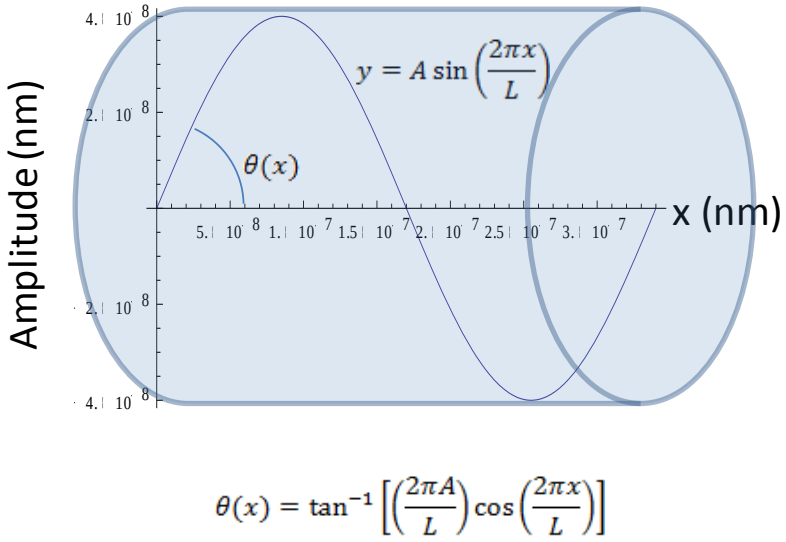

Figure 6.12 Sinusoidal geometry assumed for an individual aramid nanofiber.

The effective elastic constants of a curved Kevlar fiber are deduced from the elastic constants of a straight Kevlar fiber by executing the following series of operations:

1) Define the transversely isotropic compliance matrix, S_{ij}, of a straight Kevlar fiber using the elastic constants from the literature [10] as follows:

$$S_{ij} = \begin{bmatrix} \frac{1}{E_{11}} & -\frac{\nu_{12}}{E_{11}} & 0 \\ -\frac{\nu_{12}}{E_{11}} & \frac{1}{E_{22}} & 0 \\ 0 & 0 & \frac{1}{G_{12}} \end{bmatrix} \qquad \textbf{(Eqn. 6.6)}$$

where $E_{11} = 84.6\ \text{GPa}, E_{22} = 1.34\ \text{GPa}, \nu_{12} = 0.36, G_{12} = 16.2\ \text{GPa}$

2) Define a transformed compliance matrix, $\bar{S}_{ij}$, which transforms the straight fiber compliance values from a material coordinate system oriented in accordance with the function $\theta(x)$ to a global coordinate system:

$$\bar{S}_{ij} = \begin{bmatrix} \bar{S}_{11} & \bar{S}_{12} & \bar{S}_{16} \\ \bar{S}_{21} & \bar{S}_{22} & \bar{S}_{26} \\ \bar{S}_{16} & \bar{S}_{26} & \bar{S}_{66} \end{bmatrix} \quad \textbf{(Eqn. 6.7)}$$

where

$$\bar{S}_{11} = S_{11}\cos^4(\theta) + (2S_{12} + S_{66})\cos^2(\theta)\sin^2(\theta) + S_{22}\sin^4(\theta)$$
$$\bar{S}_{22} = S_{11}\sin^4(\theta) + (2S_{12} + S_{66})\cos^2(\theta)\sin^2(\theta) + S_{22}\cos^4(\theta)$$
$$\bar{S}_{12} = (S_{11} + S_{66} + S_{22})\cos^2(\theta)\sin^2(\theta) + S_{12}(\cos^4(\theta) + \sin^4(\theta))$$
$$\bar{S}_{66} = 4(S_{11} - S_{12})\cos^2(\theta)\sin^2(\theta) - 4(S_{12} - S_{22})\cos^2(\theta)\sin^2(\theta) - S_{66}(\cos^2(\theta) - \sin^2(\theta))^2$$

3) Effective elastic properties of the curved fiber are then calculated by assuming application of a single stress in the global reference frame and integrating the appropriate transformed compliance expression over the length of the fiber:

$$E_{xx} = \frac{L}{\int_0^L \bar{S}_{11}\,dx} \quad \textbf{(Eqn. 6.8)}$$

$$E_{yy} = \frac{L}{\int_0^L \bar{S}_{22}\,dx} \quad \textbf{(Eqn. 6.9)}$$

$$G_{xy} = \frac{L}{\int_0^L \bar{S}_{66}\,dx} \quad \textbf{(Eqn. 6.10)}$$

$$\nu_{xy} = \frac{L}{\int_0^L \bar{S}_{12}/\bar{S}_{11}\,dx} \quad \textbf{(Eqn. 6.11)}$$

Note that the transformed compliances are functions of θ, which in turn is a function of distance along the length of the curved fiber, x. Hence, the integration is taken over the length of the fiber. Furthermore, as θ varies with the ratio of amplitude to length, so do the

transformed compliance values and effective elastic properties. Using the average amplitude and length values previously discussed, the calculated effective elastic properties of a curved Kevlar fiber with sinusoidal geometry are:

$$E_{xx} = 18.0 \text{ GPa}$$
$$E_{yy} = 1.99 \text{ GPa}$$
$$G_{xy} = 2.45 \text{ GPa}$$
$$\nu_{xy} = 0.49$$

The tensile modulus and shear modulus are greatly reduced from that of a straight fiber; however, the transverse modulus slightly increases.

It should be noted that for the two dimensional curved fiber network being modeled there is no matrix material and fiber contact is neglected. If the effective fiber elastic properties were to be represented by a concentric cylinder model, only fiber properties would need to be taken into consideration.

4) To determine the effective elastic moduli of a random distribution of curved Kevlar fibers we follow a transformation procedure similar to that previously discussed. A new compliance matrix is defined in the curved fiber material coordinate system. Now the effective elastic constants of the curved fiber become inputs into the compliance matrix:

$$S_{ij}^{eff} = \begin{bmatrix} \frac{1}{E_{xx}} & -\frac{\nu_{xy}}{E_{xx}} & 0 \\ -\frac{\nu_{xy}}{E_{xx}} & \frac{1}{E_{yy}} & 0 \\ 0 & 0 & \frac{1}{G_{xy}} \end{bmatrix} \quad \textbf{(Eqn. 6.12)}$$

Once again, the compliance matrix is transformed from the material coordinate system to the global coordinate system, where φ is the angle of orientation of an ANF with respect to the global coordinates, resulting in the following transformed axial compliance constant:

$$\bar{S}_{11}^{eff} = S_{11}^{eff}\cos^4(\varphi) + \left(2S_{12}^{eff} + S_{66}^{eff}\right)\cos^2(\varphi)\sin^2(\varphi) + S_{22}^{eff}\sin^4(\varphi) \quad \textbf{(Eqn. 6.13)}$$

Assuming a uniform distribution of randomly oriented fibers, the effective two dimensional elastic modulus of the planar fiber network is calculated:

$$\frac{1}{E_{2D}^{eff}} = \int_0^{\pi} f(\varphi)\bar{S}_{11}^{eff} d\varphi \quad \textbf{(Eqn. 6.14)}$$

$$f(\varphi) = \frac{1}{\pi} \quad \textbf{(Eqn. 6.15)}$$

In this analysis a number of assumptions were made: The fiber orientation distribution is assumed to be perfectly random, allowing us to utilize the function $f(\varphi)$ defined above. Furthemore, it was assumed that the effective elastic properties of each curved fiber are indeed transversely isotropic and the fiber volume fraction is 0.85. The calculation yields an effective tensile modulus of 3.35 GPa. If, however, the fibers are assumed to be isotropic, then $E_{xx} = E_{yy} = E$ and $G_{xy} = \frac{E}{2(1+\nu_{xy})} = G$. The effective 2D modulus then increases to 15.3 GPa.

6.2.6 Discussion and Summary

The M-T model predicts an in-plane modulus (E_{11}) of 13 GPa for a 2D random Kevlar nanofiber network, which is close to the 11 GPa measured from uniaxial tensile testing. The effective nanofiber stiffness used to obtain this result was 20 GPa, which is close to the stiffness (18.0 GPa) obtained using the transversely isotropic sinusoidal fiber RVE method discussed. As the ANF LBL network doesn't have a matrix as other composites usually have, a matrix stiffness of 0.0005 GPa was assumed for the computation of E_{11}. In Figure 6.13, we demonstrate that this matrix stiffness used is an ideal value by comparing the E_{11} values

computed using a matrix stiffness of 5, 5×10^{-1}, 5×10^{-2}, 5×10^{-3}, 5×10^{-7}, 5×10^{-9}, 5×10^{-11} and 0 GPa. A matrix stiffness of 0, 5×10^{-11} or 5 GPa yields extreme E_{11} values that deviate greatly from those computed using other values. As extremely small matrix stiffness means no nanofiber to nanofiber interaction, E_{11} obtained is close to zero. On the other hand, for a matrix stiffness on the order of that of the ANF (i.e. 5 GPa), it becomes a major factor contributing to the composite stiffness. For a matrix stiffness of 5×10^{-1}, 5×10^{-2}, 5×10^{-3}, 5×10^{-7} or 5×10^{-9} GPa, the plots of E_{11} for any v_f (Poisson's ratio) are similar. The effect of the ANF volume fraction (i.e. the relative density of the ANF network) on the resultant E_{11} is shown in Figure 6.14. A change of the ANF volume fraction from 0.75 to 0.85 and from 0.85 to 0.95 promotes E_{11} by ~30 %, corresponding to more ANFs under loading.

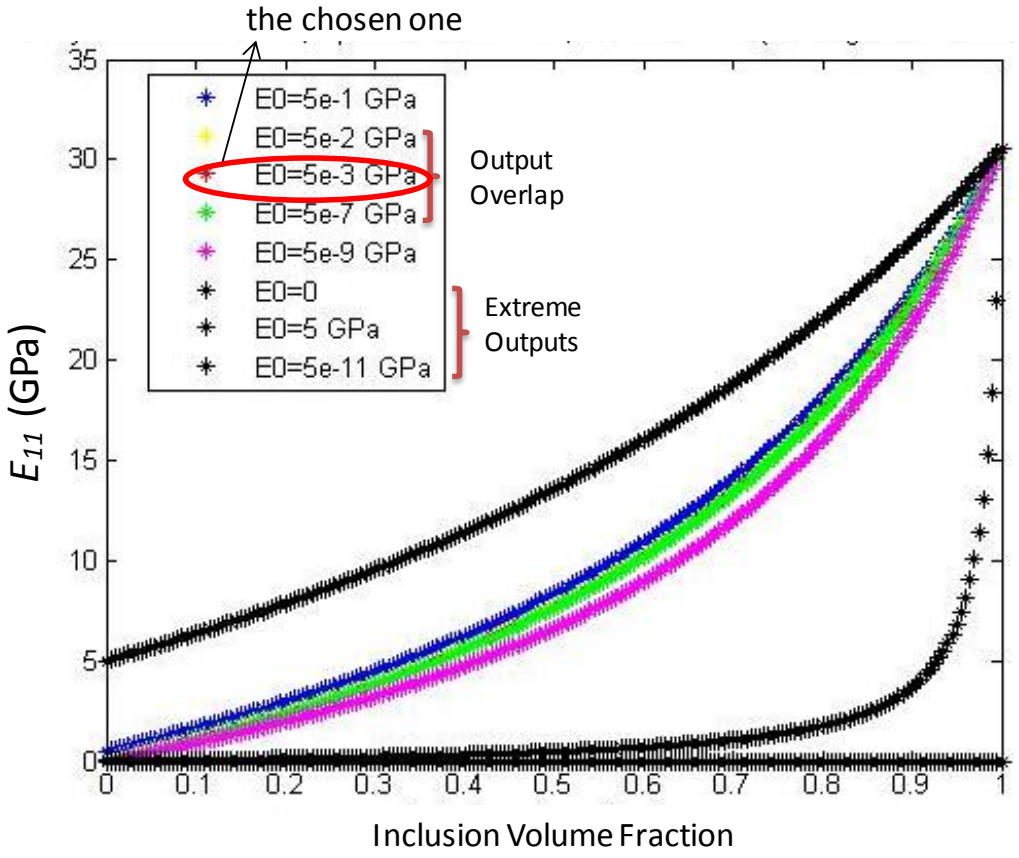

Figure 6.13 In-plane stiffness E_{11} of the ANF LBL network (with 2D random orientation of the ANFs), as a function of matrix stiffness and inclusion (ANF) volume fraction, computed from M-T model. The matrix stiffness of 5, 5×10^{-1}, 5×10^{-2}, 5×10^{-3}, 5×10^{-7}, 5×10^{-9}, 5×10^{-11} and 0 GPa were used to illustrate the effect of the matrix stiffness to E_{11}.

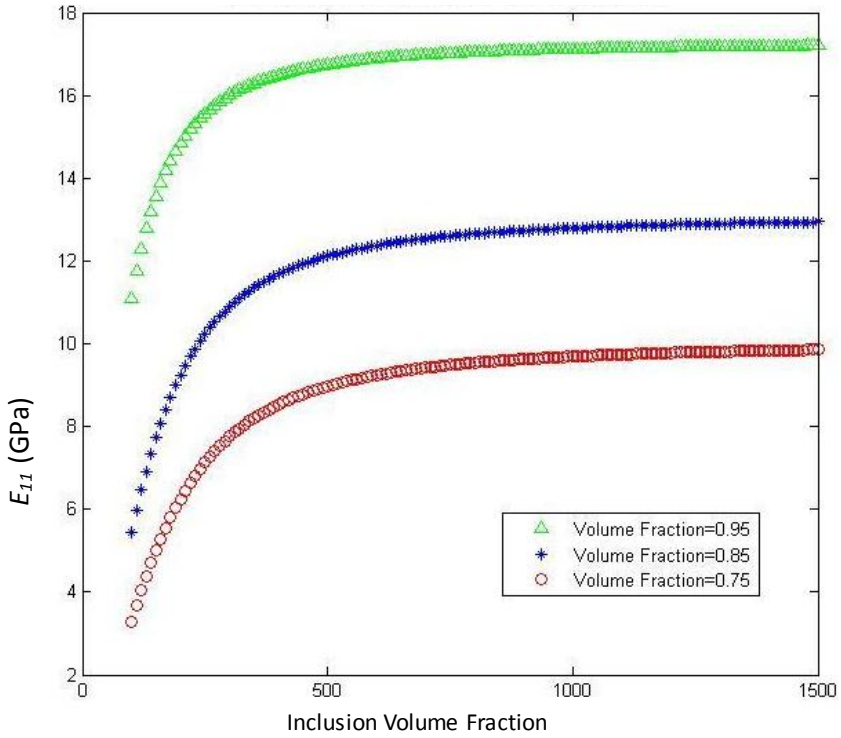

Figure 6.14 In-plane stiffness E_{11} of the ANF LBL network (with 2D random orientation of the ANFs), as a function of inclusion (ANF) volume fraction and inclusion aspect ratio, computed from M-T model. Three ANF volume fractions, 0.75, 0.85 and 0.95, were used.

However, since application of the M-T model in concert with Tandom and Weng's method is based on the assumption that both inclusion and matrix are isotropic, error is introduced; Kevlar nanofibers should exhibit transversely isotropic behavior per findings in relevant literature [10]. Further investigation should incorporate transversely isotropic inclusions into the M-T model. Moreover, although the pure Kevlar network investigated is not immersed in a matrix material, high fiber concentrations introduce nanofiber interactions that may induce matrix-like effects. Thus, quantification of these interaction effects should be analyzed and incorporated into the model.

In reference to Table 6.1, effective fiber properties and the corresponding 2D random planar network elastic moduli were investigated for several variations of the amplitude/length ratio. With respect to the effective elastic moduli of a single sinusoidal fiber, it is seen that as the amplitude approaches zero, the effective properties of the curved fiber revert back to those of the straight fiber. Furthermore, if the amplitude is defined as a measure of fiber curviness, it

is seen that greater curviness reduces the effective axial and shear moduli but increases the effective transverse modulus. If it is assumed that the fibers do in fact exhibit transversely isotropic behavior, then the effective tensile modulus of a 2D random planar network increases as fiber curviness increases. However, if it is assumed that the curved fibers actually exhibit isotropic behavior, then the effective tensile modulus of the network decreases as curviness increases.

Using the above method, elastic properties of individual sinusoidal fibers and a random planar network were calculated. Cases in which the effective fiber properties were considered isotropic and transversely isotropic were both considered. Findings are presented in Table 6.1.

Fiber Aspect Ratio (Amplitude/Length)	Effective Fiber Modulus, Axial (GPa)	Effective Fiber Modulus, Transverse (GPa)	Effective Fiber Modulus, Shear (GPa)	Effective Youngs's Modulus, Random Planar Network, Trans. Iso. Fiber (GPa)	Effective Youngs's Modulus, Random Planar Network,Iso. Fiber (GPa)
0.003 (A = 1 nm)	84.6	1.34	16.3	2.98	71.8
0.029 (A = 10 nm)	79.3	1.38	12.6	3.14	67.4
0.117 (A = 40 nm)	**18**	**1.99**	**2.45**	**3.35**	**15.3**
0.294 (A = 100 nm)	3.75	4.32	1.82	4.56	3.18
0.500 (A = 170 nm)	2.35	7.27	2.53	11.1	1.99
1.000 (A = 340 nm)	1.73	13.7	5.2	N/A	1.47

Table 6.1 Elastic properties of curved Kevlar fiber and random planar network of isotropic and transversely isotropic Kevlar fibers.

When the single sinusoidal fiber RVE approach is compared with the Mori-Tanaka approach, it is seen that both methods yield similar effective tensile moduli for a random planar network of curved fibers that individually exhibit isotropic behavior. The RVE predicts a tensile modulus of 15.3 GPa while the Mori-Tanaka approach predicts 13 GPa. It should be noted that the sinusoidal fiber approach introduces several sources of error. The overall analysis assumed that each fiber is free of contact from its neighbor when, in fact, this is likely not true. Furthermore, a single sinusoidal fiber model assumes that there is negligible variation in geometry from fiber to fiber. As seen in the micrographs in Section 6.2.2, there is clearly a great deal of variation in fiber curvature. Lastly, this analysis assumes a perfectly random distribution of fibers in space and orientation. Further analysis of fiber network imagery should be conducted to more accurately characterize the degree of spatial randomness.

In conclusion, due to the advanced mechanical properties exhibited by Kevlar nanofibers and the benefits composite Kevlar structures can provide in structural applications, there is a clear need to understand the mechanical behavior of random planar Kevlar fiber networks. Two analytical approaches to determine the effective tensile modulus of a random planar network of curved Kevlar fibers were presented. Both approaches make simplifying assumptions: The network is comprised exclusively of fibers, none of which come in contact with each other. The fibers are distributed uniformly in orientation and space. The M-T method incorporated in its calculation with the experimental data collected from uniaxial tensile tests of a 2D random planar Kevlar network. The sinusoidal fiber method incorporated experimental data from SEM and TEM imagery to identify a fiber geometry that represents the overall network. When compared, it was seen that both models predict a similar effective tensile modulus for the 2D planar fiber network. However the simplifying assumptions introduce error; future models may investigate the effects of fiber-to-fiber interface interactions, fiber-matrix interactions for the case of multi-material composite networks, or distribution functions that more realistically depict the degree of fiber randomness in space and orientation.

6.3 Elasticity of 3-D Randomly Oriented Nanofiber Network

The in-plane stiffness (E_{11}) of the ANF network with a 3D random orientation of the nanofibers was also computed using the M-T model. Lower in-plane stiffness was obtained for the network with a 3-D random orientation of the nanofibers, compared with that of the network with a 2-D random fiber orientation, as shown in Figure 6.15. This lower in-plane stiffness results from more of nanofibers oriented out of plane, compared to the 2-D case, as shown in Figure 6.16.

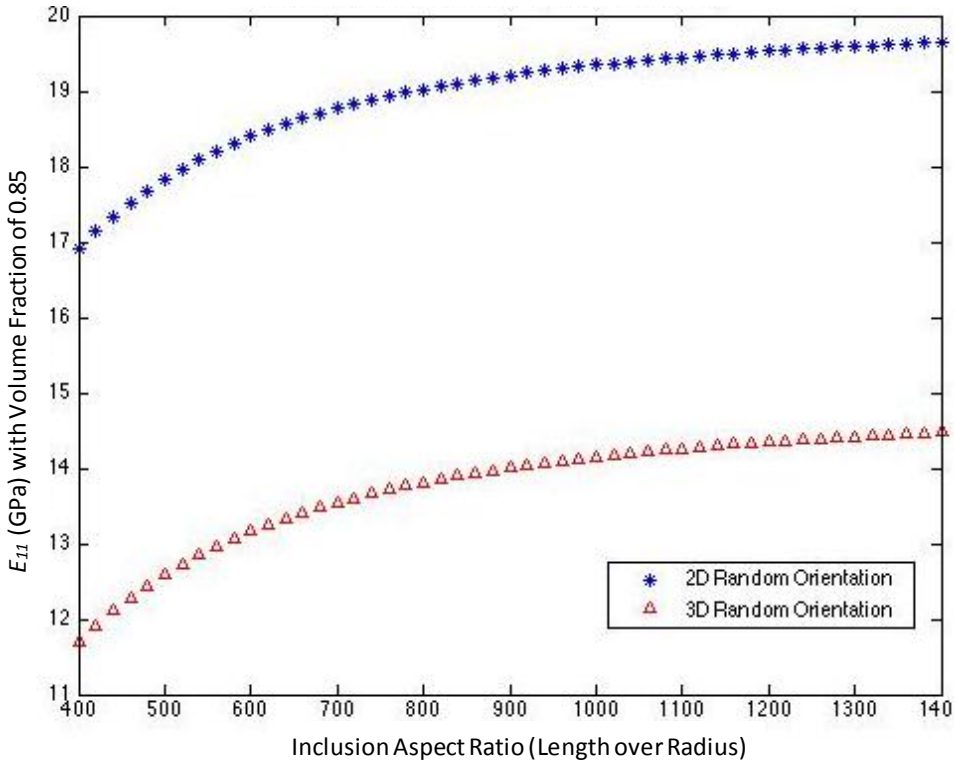

Figure 6.15 In-plane stiffness E_{11} of the ANF LBL networks. The network with a 2D random orientation of the ANFs has higher stiffness than that of the network with a 3D orientation. The inputs for the M-T model are listed on the left.

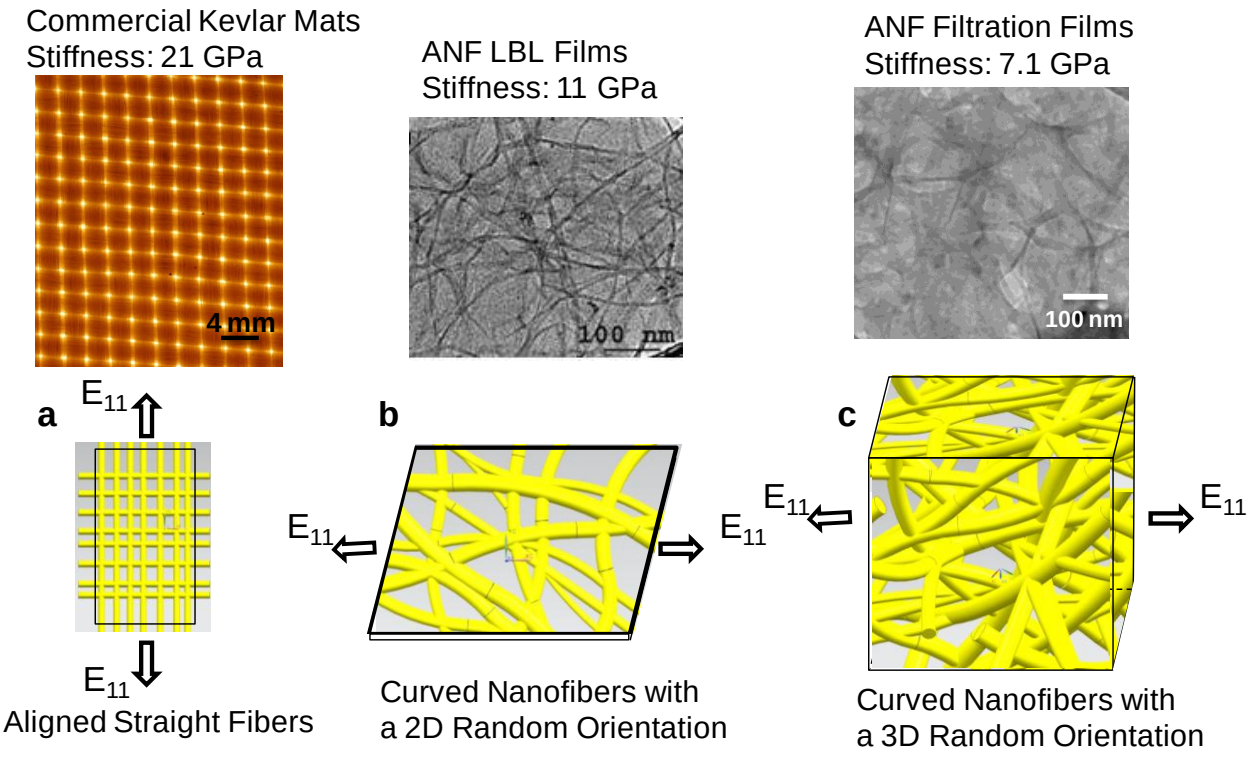

Figure 6.16 Schematic showing fiber orientations with respect to the stiffness measurement. (a) Kevlar plain-woven mats have all the straight Kevlar microfibers perfectly aligned in the 0° and 90°. (b) Layer-by-layer assembled ANF networks have all the nanofibers oriented in the plane which yields higher in-plane stiffness. (c) A 3-D random fiber orientation has nanofiber orientation in different directions (i.e. fewer nanofibers aligned in the plane), resulting in lower in-plane stiffness.

The modeling of the nanofiber networks based on ANF orientation explains the network stiffness difference resulting from two assembly methods. The LBL assembled ANF networks corresponds to the network with a 2D random orientation of nanofibers. The LBL process assembles the network by depositing nanofibers layer-by-layer, ensuring that all the ANFs are oriented in the plane parallel to the substrate. The vacuum-assisted filtration method assembles the network by filtering the solvent and leaving the nanofiber network on the filter paper for drying, which creates a network with a 3D random orientation of ANFs. Table 2 shows a comparison of the experimental stiffness with the computational stiffness of the two ANF networks. The computed stiffnesses are ~ 25 % higher than those measured from experiments, as the modeling neglects any effect from defects in the networks. The computational results well characterize the trend of stiffness change based on the fiber orientation and serve as a good demonstration of the morphology difference obtained from the two assembly methods.

In-plane Stiffness (E_{11})	**Uniaxial Tensile Testing (Experiment Result)**	**Mori-Tanaka (Analytical Result)**
ANF LBL Network (2D Random Orientation)	**11 GPa**	**13 GPa**
ANF Filtration Network (3D Random Orientation)	**7.1 GPa**	**9.3 GPa**

Table 6.2 Elastic properties of the nanofiber networks. The analytical results are close to the experimental results, which revealed the effect of nanofiber orientation on the network stiffness.

6.4 Summary and Conclusions

Three Kevlar-fiber based networks, commercial Kevlar mats, ANF LBL films and ANF filtration films, were experimentally characterized for their mechanical properties via low-strain-rate uniaxial tensile testing. Although the three networks are made of aramid fibers without any chemical treatment such as the PA/GA treatment to enhance bonding among fibers, their mechanical properties differ from each other owing to the alignment and geometry of the fibers. For commercial 0^o & 90^o woven Kevlar fibers mat with anisotropic in-plane properties, the stiffness along the fiber axis is measured as 21 GPa. For ANF LBL films and ANF filtration films with isotropic in-plane mechanical properties, the in-plane stiffnesses are measured to be 11 GPa and 7.1 GPa respectively.

This difference in the stiffness of the LBL and filtered films comes from the fiber orientation and fiber waviness, as shown in Figure 6.16. As the Kevlar mat was tested with straight aramid fibers highly aligned in the loading direction, direct stretching on the polymer backbones occurred, resulting in the highest stiffness measured among the three. For the ANF LBL film, the LBL process yielded a network with 2D randomly oriented nanofibers in the plane of loading. The nanofibers also had a waviness that can be modeled as a sinusoidal shape. This curled shape of nanofibers reduced their stiffness compared to that of straight fibers, as straightening of the curved fibers instead of stretching the polymer backbones occurred upon loading. The random fiber distribution and curved fiber geometry resulted in lower network stiffness of ANF LBL films compared to the Kevlar mat. For ANF filtration films, more nanofibers were oriented out of plane with a 3D randomness of the fiber orientation, which further reduced the network in-plane stiffness.

Reference

[1] Wu X. F. and Dzenis Y. A., "Elasticity of Planar Fiber Networks," *Jpn. J. Appl. Phys.* **2005**, Vol. 98, pp. 1-9.

[2] Christensten R. M. and Waals, F. M., "Effective Stiffness of Randomly Oriented Fiber Composites," *J. Compos. Mater.* **1975**, Vol. 6, pp. 519-532.

[3] Mori T. and Tanaka K., "Average Stress in Matrix and Average Elastic Energy of Materials with Misfitting Inclusions," *ACTA Metallurgical* **1973**, Vol. 21, pp. 571-574.

[4] Tandon G. P. and Weng G. J., "The Effect of Aspect Ration of Inclusions on the Elastic Properties of Unidirectionally Aligned Composites," *Polym. Compos.* **1984**, Vol. 5, No. 4, pp. 327-333.

[5] Li Y. et al, "A closed-form, hierarchical, multi-interphase model for composites-derivation, verification and application to nanocomposites," *J. Mech. Phys. Solids* **2010**, Vol. 59, pp. 43–63.

[6] Tandon G. P. and Weng G. J., "Average Stress in the Matrix and Effective Moduli of Randomly Oriented Composites," *Compos. Sci. Technol.* **1986**, Vol. 27, pp. 111-132.

[7] M. Yang, K. Cao, L. Sui,Y. Qi, J. Zhu, A. M. Waas, E. M. Arruda, J. Kieffer, M. D. Thouless, N. A. Kotov, "Dispersions of ANSs: A New Nanoscale Building Block," *ACS Nano* **2011**, Vol. 5, No. 9, pp. 6945–6954.

[8] Lee S. H. and Waas A. M., "Compressive response and failure of fiber reinforced unidirectional composites," *Int. J. Fract.Mech.* **1999**, Vol. 100, pp.275-306.

[9] Rai H. G., Rogers C. W. and Crane D. A., "Mechanics of Curved Fiber Composites," *J. Reinf. Plast. Compos.* **1992**, Vol. 2, pp. 552-566.

[10] Cheng M., Chen W. and Weerasooriya T., "Experimental Investigation of the Transverse Mechanical Properties of a Single Kevlar KM2 Fiber," *Int. J. Solids Struct.* **2004**, Vol. 41, pp. 6215-6232.

Chapter 7

Aramid Nanocomposites with Gold Nanoparticles

The two aramid building block nanostructures: nanofibers or nanosheets, controlled by the extent of the PA hydrolysis treatment, can bond with various moieties to form aramid networks with tailored nanostructures, morphologies, and mechanical properties [1]. In this chapter, these aramid nanostructures are used as high performance polymeric building blocks that form interactions with citrate-stabilized gold nanoparticles (AuNPs) that are strong enough to influence the mechanical properties. The networks are assembled through a vacuum-assisted filtration method to form nanostructured 60 mm diameter × 5-15 μm thick films. The structure-property relationships were thoroughly investigated to develop strategies to systematically optimize the mechanical properties of the aramid nanostructure/gold nanoparticle composites. These results are the first demonstration of the use of aramid nanoscale fibers to form versatile nanosized building blocks that can then be conjugated to fabricate composite structures involving materials previously thought to be impossible to use in such applications, and thus creating a new generation of nanostructured aramid materials. The combination of aramid nanostructures with novel materials such as AuNPs opens doors for the exploration of other properties, such as light-absorption or electrical conductivity, which can potentially provide other applications for these aramid nanostructure networks with sufficient mechanical properties to resist loading and fracture, such as future solar cell or energy harvesting materials [2,3].

7.1 Tuned Mechanical Properties of Aramid Nanostructured Networks

High surface-to-volume ratio aramid nanofibers (ANFs) obtained from macroscopic-scale Kevlar fibers **[**1, 4**]** and gold nanoparticles (AuNPs) stabilized by sodium citrate [5] form the basis of a new generation of nanostructured materials. Here we demonstrate that the ANFs can be made chemically reactive with useful functional groups [1] for bonding with a ligand (e.g. citrate), and that these reactive aramid building blocks can be assembled with citrate and AuNPs into transversely isotropic networks with tailored nanostructures, morphologies and properties. Uniaxial tensile tests at room temperature were used to characterize the mechanical properties of the aramid nanostructured networks. The reaction mechanisms during the phosphoric acid /citrate + gold nanoparticles (PA/citrate+AuNPs) treatment of the Kevlar and the resultant bonding and morphology of the networks were explored using (i) Fourier-transform infrared spectroscopy (FTIR) to probe the chemical structures, (ii) transmission electron microscopy (TEM) to visualize the morphologies, (iii) ultraviolet–visible spectroscopy (UV-Vis) to investigate the interaction between aramid nanostructures and AuNPs, and (iv) thermogravimetric analysis (TGA) to characterize the thermal stability and composition of the nanostructured networks.

7.1.1 Synthesis

Three families of aramid nanostructured films were prepared to study the effect of using different amounts of phosphoric acid (PA), citrate and citrate-AuNPs on the mechanical properties of the films. Synthesis consisted reacting a Kevlar/potassium hydroxide (KOH)/dimethyl sulfoxide (DMSO) solution of ANFs with 1) various amounts of PA, followed by adding a fixed amount of a citrate/AuNP solution; 2) a fixed amount of PA, followed by two amounts of citrate powder; and 3) a fixed amount of PA, followed by adding various amounts of the citrate/AuNP solution. Also, an ANF network with no treatment (the ANF filtration film) was made as a comparison by adding water to the ANF solution. After chemical treatment, films were fabricated from the solution by vacuum-assisted filtration to obtain continuous and homogeneous structures. The twelve different conditions used to

prepare the three families of aramid networks are shown in Table 7.1, along with optical micrographs of several of the resultant products shown in Figure 7.1. The AuNPs used to prepare these samples had diameters of 13 nm, controlled by the weight ratio of citrate to AuNPs during the citrate/AuNP solution preparation, which was ~3.7 for 13 nm particles [5].

It should be noted that it was not possible to form a continuous and homogeneous film of sufficient strength for testing with ANF solutions that had been exposed to PA but not to citrate or citrate+AuNPs (Figure 2.a "No Citrate/Gold" sample). This result indicates that citrate and citrate+AuNPs exposures improve the interactions among the aramid nanofibers to provide sufficient mechanical integrity for tensile testing. It was also not possible to form a testable network from solutions exposing to citrate and AuNPs but not to PA (Figure 2.a "No PA" sample), demonstrating that hydrolysis is first needed for the citrate-based exposure to have an effect. A sample made by adding chloroauric acid ($HAuCl_4$), a precursor to make the citrate/AuNP solution, in the Kevlar/KOH/DMSO solution and exposed to the same synthesis conditions also resulted in a very brittle film without sufficient strength for mechanical testing. This also reflects that PA hydrolysis is essential to have ANFs reactive for bonding.

Samples containing 40 mg Kevlar and 13 nm AuNPs	**PA** (85 wt%)	**Citrate**	**AuNP** (13 nm)	**Young's Modulus**
Sample Name	(mL)	(mg)	(mg)	(GPa)
No Treatment	0	0	0	7.1 ± 0.3
PA-0.1	**0.1**	13	3.6	7.8 ± 0.8
PA-0.2	**0.2**	13	3.6	9.0 ± 0.6
PA-0.3	**0.3**	13	3.6	9.3 ± 0.9
PA-0.4	**0.4**	13	3.6	8.4 ± 0.7
PA-0.5	**0.5**	13	3.6	6.0 ± 0.6
Cit-4	0.3	**4**	0	5.0 ± 0.7
Cit-13	0.3	**13**	0	5.8 ± 0.9
Au-Cit-1	0.3	**4**	**1**	6.2 ± 0.9
Au-Cit-3.6	0.3	**13**	**3.6**	9.3 ± 0.9
Au-Cit-7.2	0.3	**26**	**7.2**	9.9 ± 1.0
Au-Cit-3.6-0.5	0.5	**13**	**3.6**	6.0 ± 0.6
Au-Cit-7.2-0.5	0.5	**26**	**7.2**	6.4 ± 0.7
No PA	0	13	3.6	-
No Citrate/Gold	0.3	0	0	-

Table 7.1 Aramid networks manufactured by vacuum-assisted filtration with various PA, citrate and citrate+AuNP (13 nm diameter) contents during synthesis. An ANF network with no treatment was made as a comparison. A parameter study of each constituent was made by varying its quantity to understand its effect on the resulting mechanical properties. Continuous and homogenous networks were successfully obtained from all treatments, except for the samples made with just PA ("No Citrate/Gold") or just Citrate ("No PA"). For each composition, at least two batches of samples were made and four specimens from each batch were tested. Samples PA-0.3 and Au-Cit-3.6 are the same sample, similarly Samples PA-0.5 and Au-Cit-3.6-0.5 are the same.

Figure 7.1 Optical micrographs of three aramid network samples showing the change of color through the addition of gold nanoparticles. The samples change from transparent and yellow ("No Treatment"), to translucent and yellow ("Cit-13" with PA and citrate treatment), to translucent and purple ("Au-Cit-3.6" with PA, citrate and AuNPs). The isotropy of the samples was checked by testing specimens at different orientations in the X-Y plane and from nano-indentation testing on the thickness direction [4].

Table 7.2 describes another family of aramid nanostructured films that were synthesized using a larger AuNP size (60nm diameter), to study the effect of the AuNP size on the mechanical properties of the nanocomposites. For a valid comparison between samples with two AuNP sizes, Sample Au(60)-Cit-Extra was made with equal weight fractions of PA, citrate and AuNPs as those of Sample Au-Cit-3.6 with the 13 nm AuNPs. In order to generate a 60nm Au Films with a citrate to Au ratio of 1.1, more citrate must be added before the citrate/ 60nm AuNP solutions. As the citrate-Au ratio is fixed for a given AuNP size, the citrate/AuNP solution with 60 nm diameter particles was prepared using a citrate-AuNP ratio of ~ 1.1, compared to ~ 3.7 for a 13 nm diameter solution [5]. Sample Au(60)-Cit-Extra was made for this comparison, by adding an extra 9 mg citrate prior to the addition of the citrate/AuNP (60 nm) solution.

Samples containing 40 mg Kevlar and 60 nm AuNPs	**PA**	**Citrate**	**AuNP**	**AuNP** diameter	**Young's Modulus**
Sample	(mL)	(mg)	(mg)	(nm)	(GPa)
Au-Cit-3.6	0.3	**13**	3.6	**13**	9.3 ± 0.9
Au(60)-Cit	0.3	**4**	3.6	**60**	7.4 ± 0.7
Au(60)-Cit-Extra	0.3	**4 + 9**	3.6	**60**	7.6 ± 0.7

Table 7.2 Aramid nanostructured networks assembled by vacuum-assisted filtration with AuNPs of 60 nm diameter for comparison with the 13 nm AuNPs sample. For a valid comparison between samples with two AuNP sizes, Sample Au(60)-Cit-Extra was made by adding extra 9 mg of citrate, to obtain equal weight fractions of PA, citrate and AuNPs as those of Sample Au-Cit-3.6 with the 13 nm AuNPs. For each composition, at least two batches of samples were made and four specimens from each batch were tested.

7.1.2 The Effect of PA Hydrolysis: Functionalization of ANFs

Hydrolyzing ANFs by using phosphoric acid is a proven method to create more functional groups on aramid molecules, which improves the surface bonding of ANFs with other constituents [1]. However, extensive hydrolysis induced by PA changes the morphology of the ANFs into nanosheets, which reduces the network stiffness, as discussed in Chapter 5 [1].The mechanical properties of the PA/citrate+AuNP treated films were also tuned by the

amount of PA used during synthesis. As characterized by room-temperature uniaxial tensile testing at a strain rate of 0.005/s, Figure 7.2 illustrates how an increased amount of PA hydrolysis tends to result in a stiffer material from 0.1 mL to 0.3 mL PA at constant weight fraction of Kevlar, while further increasing PA hydrolysis from 0.3 mL to 0.5 mL tends to result in a more compliant material. A finite level of hydrolysis is required to provide active sites for the subsequent reaction with the citrate and gold, as the "No PA" sample does not form a continuous network [1]. Citrate and AuNPs are not able to form bonds with the inert aramid molecules, unless water is used as in the "No Treatment" case, which re-protonates aramid macromolecules so that they form a film through hydrogen bonding of aramid fibers with one another [1].

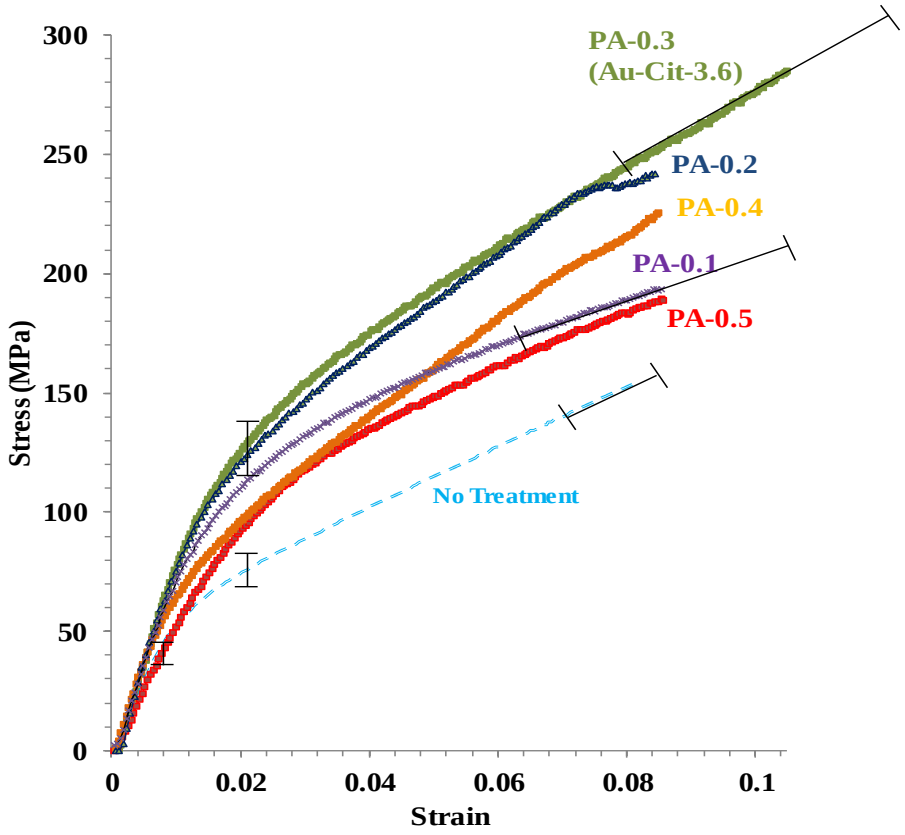

Figure 7.2 Stress-strain curves of aramid films as functions of PA content characterized by uniaxial tensile tests at a strain rate of 0.005/s at room temperature. The mechanical properties of these nanostructured networks were tuned by the extent of the PA treatment. Initially upon an increase in PA, the stiffness and strength increased owing to more available functional groups for bonding aramid/citrate+AuNP. A further increase in the amount of PA dyfrolysis resulted in a decrease in these mechanical properties, much as it did in Chapter 5.

At least four tests were performed on each sample until fracture and each sample was repeated to ensure the batch variance. Consistent results were obtained. The uncertainty of the strain to failure is relatively large owing to the relatively brittle nature of the samples.

Sample PA-0.3 (which is also Au-Cit-3.6) had the highest stiffness and strength, as the PA functionalization provided sufficient bonding sites for citrate, without over-hydrolyzing the ANFs. The effect of PA hydrolysis on the morphology and the resultant mechanical and thermal properties of the aramid networks was thoroughly discussed in Chapter 5 [1].

7.1.3 The Effect of Citrate: Bonding of Hydrolyzed ANFs

The mechanical properties of the PA/citrate+AuNP treated films were also tuned by the amount of citrate used during synthesis. As shown in Figure 7.3, two samples were synthesized with the addition of citrate powder after PA hydrolysis (i.e. without AuNPs) to examine its effect. For a fixed level of hydrolysis, a higher citrate level promotes the stiffness, yield strength and ultimate strength of the networks (Sample Cit-4 with 0.3 mL PA and 4 mg citrate compared with Sample Cit-13 with 0.3 mL PA and 13 mg citrate). This increase is provided by a higher level of bonding with the hydrolyzed aramid nanostructures, leading to a stronger interaction among them. This effect will saturate however, by having excess amount of citrate, which will be future discussed in Figure 7.6. More information on how the level of bonding among hydrolyzed aramid nanostructures affects the network mechanical properties was given in Chapter 5, where glutaraldehyde was used as a crosslinker [1].

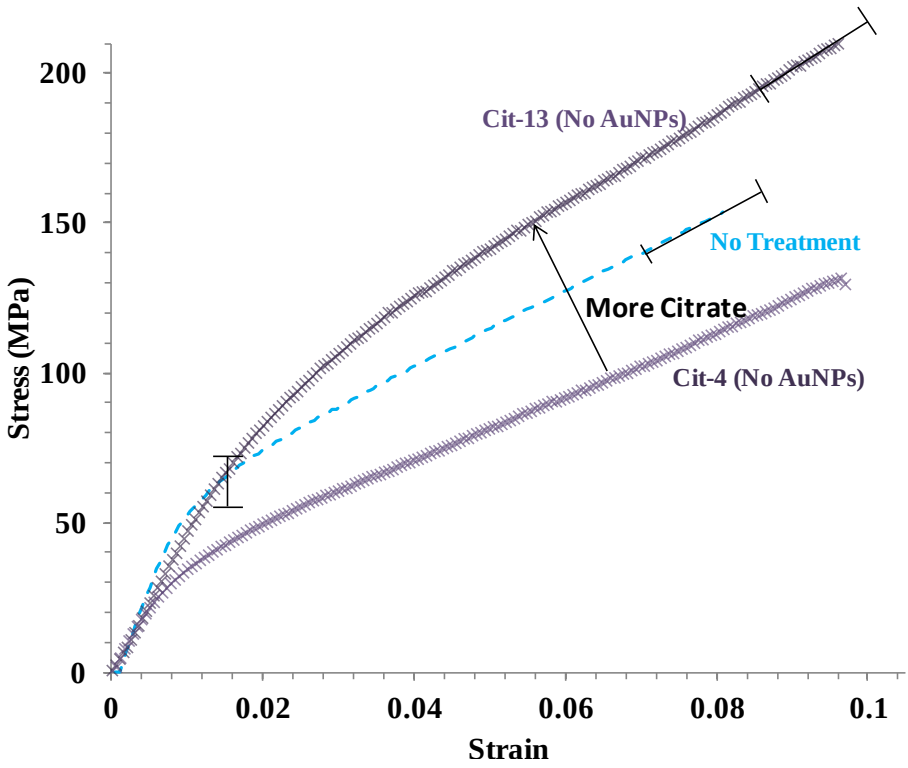

Figure 7.3 Stress-strain curves of aramid films as a function of citrate content characterized by uniaxial tensile tests at 0.005/s. Citrate forms bonds with hydrolyzed aramid molecules [1]. The higher citrate content improves the network stiffness and strength, as more functional groups created by hydrolysis are bonded to the ANFs. At least four tests were performed on each sample until fracture and each sample were repeated to ensure the batch variance. Consistent results were obtained.

7.1.4 The Effect of AuNPs: Reinforcement in Aramid Networks

Figures 7.4 and 7.7 show that by adding gold nanoparticles the stiffness and strength of the networks can be further enhanced. For a fixed level of PA hydrolysis and citrate bonding, as shown in Figure 7.4, addition of 3.6 mg of AuNPs in Sample Au-Cit-3.6 (i.e. PA-0.3) compared to Sample Cit-13 without gold reinforced the network to result in a higher modulus, yield strength and ultimate strength. Similarly the addition of 1 mg of AuNPs in Sample Au-Cit-1 compared to Sample Cit-4 without gold reinforced the networkto also result in a higher stiffness, yield strength and ultimate strength. Figure 7.5 is another indication that

AuNPs serve as a reinforcement phase to promote the mechanical properties of the networks. The comparison made in Figure 7.5 is between Sample Cit-13 (with 0.3 mL PA and 13 mg citrate but no AuNPs) and the samples with various amounts of PA and fixed amounts of citrate and AuNPs shown in Figure 7.2. Although Samples PA-0.4 (with 0.4 mL PA, 3.6 mg AuNPs and13 mg citrate) and PA-0.5 (with 0.5 mL PA, 3.6 mg AuNPs and13 mg citrate) both have higher levels of PA hydrolysis than Sample Cit-13 (with 0.3 mL PA and 13 mg citrate), they also both contain AuNPs whereas Cit-13 does not, and they both have higher stiffness and yield strength than Cit-13.

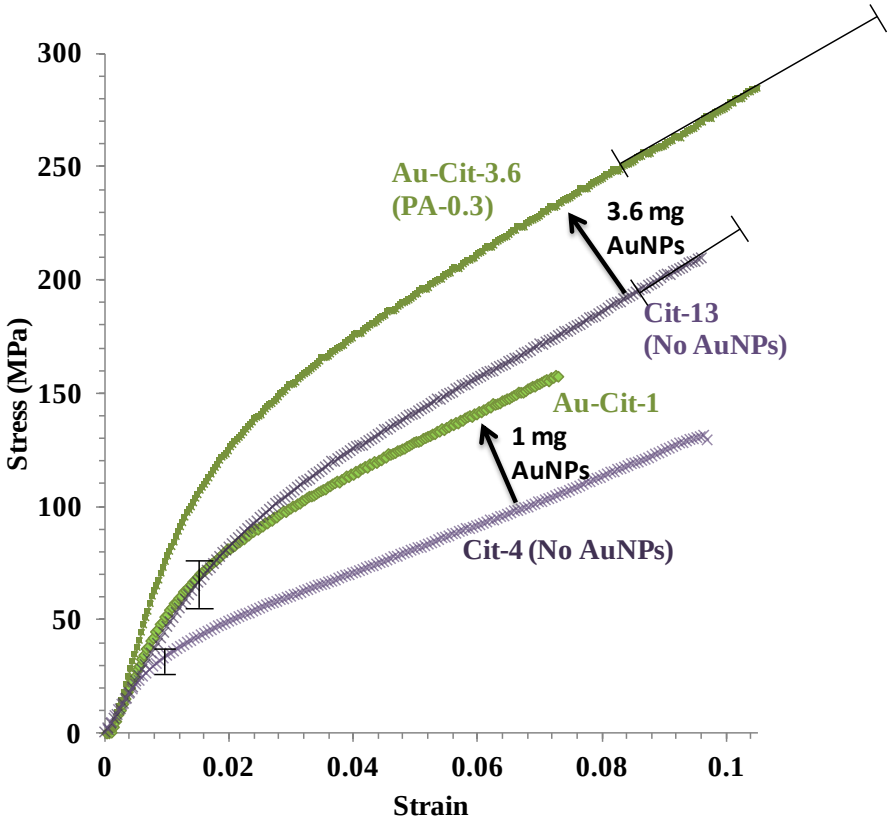

Figure 7.4 Stress-strain curves of aramid films with and without AuNPs characterized by uniaxial tensile tests at 0.005/s. Sample Au-Cit-3.6 (with 0.3 mL PA, 13 mg citrate and 3.6 mg AuNPs) and Sample Au-Cit-1 (with 0.3 mL PA, 4 mg citrate and 1 mg AuNPs) have AuNPs. Samples Cit-13 and Cit-4 without AuNPs do not have AuNPs but do have the same levels of PA and citrate as Au-Cit-3.6 and Au-Cit-1 respectively. The stiffnesses and strengths of the samples with AuNPs are better than those of the samples without AuNPs owing to the reinforcement effect of AuNPs. At least four tests were performed on each sample until fracture and each sample was repeated to ensure the batch variance. Consistent results were obtained. The uncertainty of the strain to failure is relatively large owing to the relatively brittle nature of the samples.

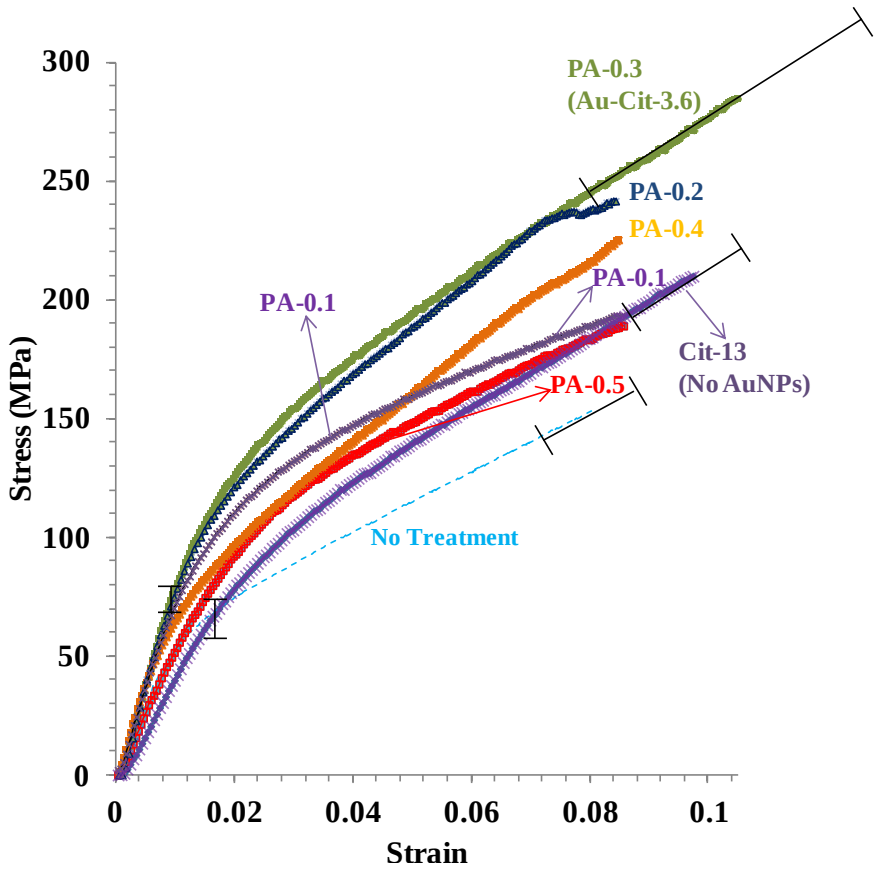

Figure 7.5 Comparison between the stress-strain curves of aramid films with AuNPs (the curves from Figure 7.2) and that of Sample Cit-13 without AuNPs characterized by uniaxial tensile tests at 0.005/s. The samples with AuNPs all had higher stiffness and yield strength, even with a higher PA content, than those of the sample without AuNPs, which is another indication of the reinforcement effect of AuNPs. At least four tests were performed on each sample until fracture and each sample was repeated to ensure the batch variance. Consistent results were obtained. The uncertainty of the strain to failure is relatively large owing to the relatively brittle nature of the samples.

Citrate and AuNPs both contribute to increases in the modulus, yield strength and ultimate strength of PA/citrate-AuNP-treated aramid networks provided there is sufficient PA hydrolysis to functionalize ANFs. These increases saturate, however, as an excess of citrate/AuNP solution beyond that used in Au-Cit-3.6 provides no further improvement in mechanical properties. Figure 7.6 shows that the mechanical properties of Samples Au-Cit-3.6 (PA-0.3, with 0.3 mL PA, 13 mg citrate and 3.6 mg AuNPs) and Au-Cit-7.2 (with 0.3 mL PA,

26 mg citrate and 7.2 mg AuNPs) were probably identical, despite the higher amounts of citrate and AuNPs in Au-Cit-7.2. This result indicates that the excess citrate/AuNPs in Sample Au-Cit-7.2 were effective in bonding with the hydrolyzed aramid nanostructures to further increase the network stiffness and strength. Increasing hydrolysis to 0.5 mL to increase the number of potential bonding sites for the citrate+AuNPs, also did not improve mechanical properties of the nanocomposites beyond what is achieved for Sample Au-Cit-3.6-0.5. Figure 7.6b indicates that doubling the amount of citrate/AuNPs as Sample Au-Cit-7.2-0.5 yielded almost identical mechanical properties. This result further confirms that Sample Au-Cit-3.6 has saturated amounts of citrate and AuNPs. (An additional check, which was not done, is FTIR analysis of the filtered solution for the presence of the excess citrate.) If the hydrolyzed sites are not saturated, as is the case for Sample Au-Cit-1(with 0.3 mL PA, 1 mg AuNPs and 4.2 mg citrate), the network modulus and strength increases with an addition of the citrate/AuNP solution (Sample Au-Cit-3.6).

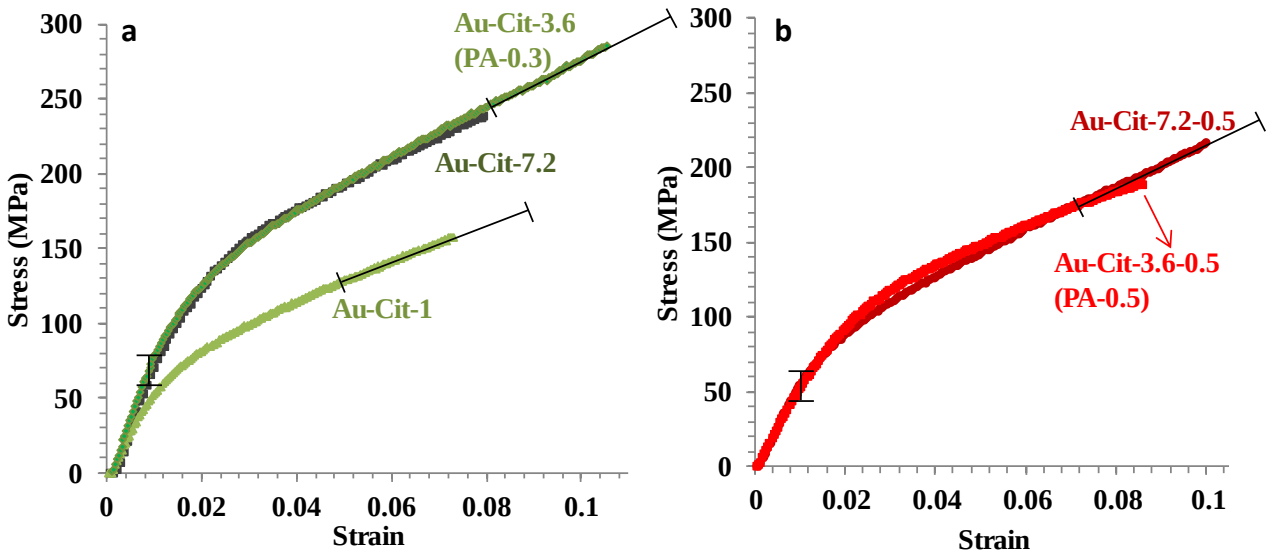

Figure 7.6 Stress-strain curves of aramid films with different levels of citrate+AuNPs characterized by uniaxial tensile tests at 0.005/s. As the citrate+AuNP content increases from 4 mg citrate + 1 mg AuNPs in Au-Cit-1 to 13 mg citrate + 3.6 mg AuNPs in Au-Cit-3.6, the modulus and strength both improve. This reinforcement effect is limited, dependent on the availability of PA hydrolysis induced bonding sites, as a further increase in citrate + AuNPs to 26 mg citrate + 7.2 mg AuNPs in Au-Cit-7.2 does not lead to further improvements in these mechanical properties. For a higher PA hydrolysis level with 0.5 mL PA in (b), a further increase in citrate+ AuNPs from 13 mg citrate + 3.6 mg AuNPs to 26 mg citrate + 7.2 mg AuNPs in Au-Cit-7.2 does not lead to improvement in mechanical properties. This suggests that for a 0.3 mL PA level in (a), 13 mg citrate + 3.6 mg AuNPs exceed the amounts needed to ensure the functional sites from PA hydrolysis are bonded to the maximum exten possible with this system. At least four tests were performed on each sample until fracture and each sample was repeated to ensure the batch variance. Consistent results were obtained. The uncertainty of the strain to failure is relatively large owing to the relatively brittle nature of the samples.

Figure 7.7a shows a comparison between the aramid/citrate+AuNP samples with different AuNP size. At small strains, the amount of total particle surface area dominates the properties, as Sample Au-Cit-3.6 with 13 nm diameter particles, i.e. 4.6 times of total surface area for bonding compared to that of samples with 60 nm AuNPs, has a higher stiffness than samples with 60 nm diameter AuNPs. For a fixed amount of AuNPs, a smaller particle size means a larger surface area to volume ratio; thus there is more total surface area available for bonding. The size of the AuNPs thus affects the degree of physical attachment of the AuNPs to the hydrolyzed aramid chains. The stiffness of the sample with 60 nm AuNPs is closer to those of samples with only citrate and no AuNPs, as its total surface area of AuNPs is too small to yield a prominent reinforcement effect. At large strains, the amounts of AuNPs and citrate (i.e. the magnitude of their quantities) in the samples dominate their mechanical properties. The stress-strain curves of Samples Au-Cit-3.6 and Au(60)-Cit-Extra with the same amounts of PA, citrate and AuNPs start to converge, and for those samples with different amount of citrate or AuNPs, their stress-strain curves deviate at larger strains. In Figure 7.7b, the reinforcement effect of AuNPs beyond samples without AuNPs (only with citrate) is also seen for the larger AuNPs but the effect is not as pronounced with larger AuNPs. The addition of AuNPs improves the stiffness and strength of the films. Again, hydrolysis is constant and the level of citrate is the same in each pair.

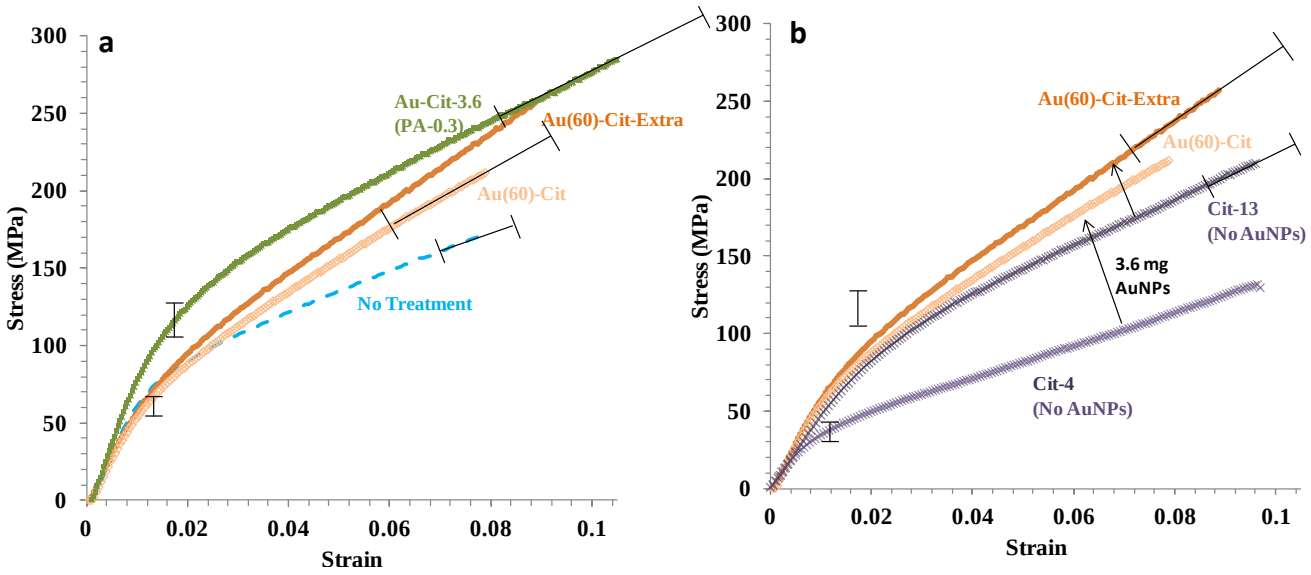

Figure 7.7 a) Stress-strain curves of aramid nanostructured networks with two AuNP sizes (13 vs. 60 nm) used in synthesis, compared with the "No Treatment" sample. Total surface area dominates the mechanical properties at small strains and the amounts of citrate and AuNPs govern the properties at large strains. Sample Au-Cit-3.6 and Sample Au(60)-Cit-Extra had identical amounts of PA, citrate and AuNPs, but one with 13 nm diameter particles and the other with 60 nm. Higher stiffness and strength were obtained for the sample with smaller particle size at small strains, as the total surface area of Sample Au-Cit-3.6 was 4.6 times of that of Sample Au(60)-Cit-Extra. Their behavior at larger strain started to converge which indicated that the magnitudes of the constituents, i.e. how much PA, citrate and AuNPs are used, play a bigger role when deformation of the material is high. b) Additional AuNPs in Samples Au(60)-Cit-Extra and Au(60)-Cit, compared to the corresponding citrate samples with the same amounts of PA and citrate but without AuNPs, help to promote the network stiffness and strength owing to the effective reinforcement effect of AuNPs. At least four tests were performed on each sample until fracture and each sample was repeated to ensure the batch variance. Consistent results were obtained. The uncertainty of the strain to failure is relatively large owing to the relatively brittle nature of the samples.

7.2 Reaction Mechanisms of Phosphoric Acid, Citrate and Gold Nanoparticles

7.2.1 Proposed Interactions among Constituents

The interactions between hydrolyzed ANFs and AuNPs through hydrogen bonding with citrate are discussed in this paragraph, and a schematic of the interactions among the network constituents is shown in Figure 7.8. As aramid macromolecules are known for being relatively inert [1, 6-12], hydrolysis was chosen as a method to induce reactivity of aramids by the formation of amines and carboxylic acids. This chemical modification allows them to be more reactive as more functional groups are created for surface bonding, as discussed in Chapter 5 [1]. Here, we considered the example of citrate-stabilized AuNPs as an effective bonding agent to form hydrogen bonds with hydrolyzed aramid molecules. Citrate is an organic molecule that can interact with hydrolyzed aramid nanostructures. Citrate is attached to the AuNPs in a metal-organic coordination complex in which the electron-rich oxygen atoms of the citrate act as binding ligands to the gold atoms. However, these same electron-rich groups can potentially react with the products of the hydrolysis reaction and yield a network of Kevlar macromolecules with physically bonded gold particles, creating a particle-reinforced nanocomposite with an isotropic Kevlar matrix, as shown in Figure 7.8. In the citrate/AuNP solution, gold forms a metal-organic complex with citrate molecules. Each AuNP has an electro-gradient and its surface has more electro-positivity. The carboxylic acid groups of the citrate can donate electrons to the gold atoms to stabilize the metallic positivity through polar effects [5]. These non-covalent bonds of the citrate/AuNP complexes have a low melting temperature. Therefore, in a heated solution with hydrolyzed Kevlar, some of the functional groups of the citrate molecules will react with the hydrolyzed aramid chains. This results in citrate molecules attached to the aramid chains through hydrogen bonding as well as AuNPs, hence, AuNPs are grafted to the aramid chains. Furthermore, as each citrate has three carboxylic acid groups and one hydroxyl, it is possible for one citrate molecule to attach to more than one hydrolyzed aramid chain, which promotes the interactions among the aramid nanostructures.

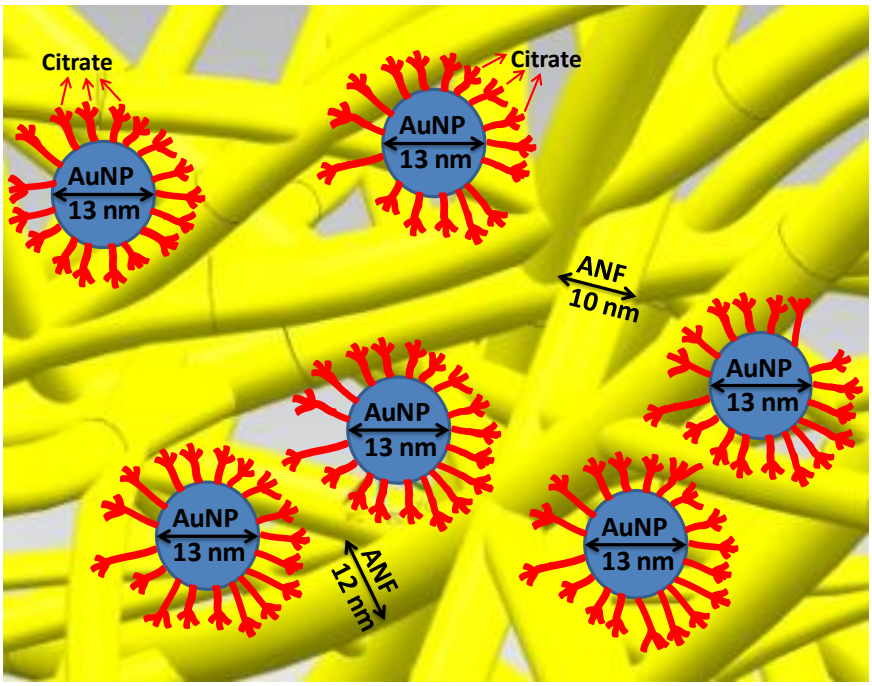

Figure 7.8. Schematic showing the ANF/AuNP interaction through hydrogen bonding with citrate. As a bonding ligand, citrate provides secondary bonding between AuNPs and ANFs, which allows AuNPs to "stick" to the ANF matrix.

7.2.2 Interactions between Citrate and Aramid Matrix

To probe the chemical structures of the aramid networks with PA/citrate treatment, FTIR was used to investigate the synthesis products prior to film formation as well as the filtrated films after. As FTIR has limitation of detecting metal atoms/bonds, the spectra performed on samples with the PA/citrate powder treatment, i.e. Sample Cit-13 in Table 7.1 and Figure 7.3, and with the PA/citrate+AuNPs treatment, i.e. Sample PA-0.3 in Table 7.1 and Figure 7.2, are used to understand the bonding between citrate and aramid molecules by comparing to the FTIR spectra of the aramid network with no treatment and the sodium citrate. The spectrum of the PA/citrate powder treated aramid network showed some changes compared to the spectra performed on the network with no treatment, additional peaks from citrate and interactions between citrate and aramid matrix owing to hydrogen bonding were observed. The spectrum of the PA/citrate+AuNPs treated aramid network, i.e. Sample PA-0.3

in Table 7.1 and Figure 7.2, showed similar peaks as those of citrate in the fingerprint area, showing the trace of citrate in the film. Both spectra with the treatment have similar major features of peaks as the one with No Treatment, indicating that the treatment preserves the majority of the Kevlar chemical structure and the modifications are on the surfaces of the ANFs.

FTIR spectroscopy of the un-treated network shows peaks of nitrogen-hydrogen bonds (3331 cm^{-1}, peak 1 in Figure 7.9.a.1) and the carboxyl groups (1668 cm^{-1}, peak 2 in Figure 7.9.a.1) in amides. Peaks 3 and 4 represent, respectively, amides and aromatic carbon-hydrogen bonds in benzene rings [1, 4, 13, 14]. Figure 7.9.a.2 shows the aramid chemical structure.

FTIR spectroscopy of sodium citrate shows peaks of oxygen -hydrogen bonds (3332 cm^{-1}, peak 1 in Figure 7.9.b.1) and the carboxyl groups (1647 cm^{-1}, peak 2 in Figure 7.9.b.1) in amides [15]. Figure 7.9.b.2 shows the sodium citrate chemical structure.

FTIR spectroscopy of the networks formed after PA/citrate treatment (Figure 7.9.c.1) was performed on a PA/citrate sample (Sample Cit-13 in Table 7.1 and Figure 7.3). The resulting spectrum shows similarity of the peaks and additional peaks compared to the spectra 7.9.a.1 and 7.9.b.1, indicating the presence of citrate and the interaction of citrate with aramid matrix. The spectrum shows the appearance of 1) a broader stretching signal around 3331 cm^{-1} from oxygen -hydrogen bonds, owing to the presence of citrate (peak 1 in Figure 7.9.c.1 compared to Figure 7.9.a.1); 2) the new peaks around 2900 cm^{-1} from carbon-hydrogen bonds in citrate (peaks 2 in Figure 7.9.c.1 compared to Figure 7.9.a.1); and 3) the appearance of a new peak around 1710 cm^{-1} possibly from a combination of bands from C=O (peaks 3 in Figure 7.9.c.1), which can be rationalized by the interaction between citrate and aramid molecules owing to hydrogen bonding [15].

FTIR spectroscopy of the networks formed after PA/citrate+AuNPs treatment shows peaks of nitrogen-hydrogen bonds (3319 cm^{-1}, peak 1 in Figure 7.9.d.1) and the carboxyl groups (1660 cm^{-1}, peak 2 in Figure 7.9.d.1) in amides. Peaks 3 and 4 (in Figure 7.9.d.1) have the same wavenumbers as those of peaks 3 and 4 of citrate (in Figure 7.9.b.1), indicating traces of citrate in the films.

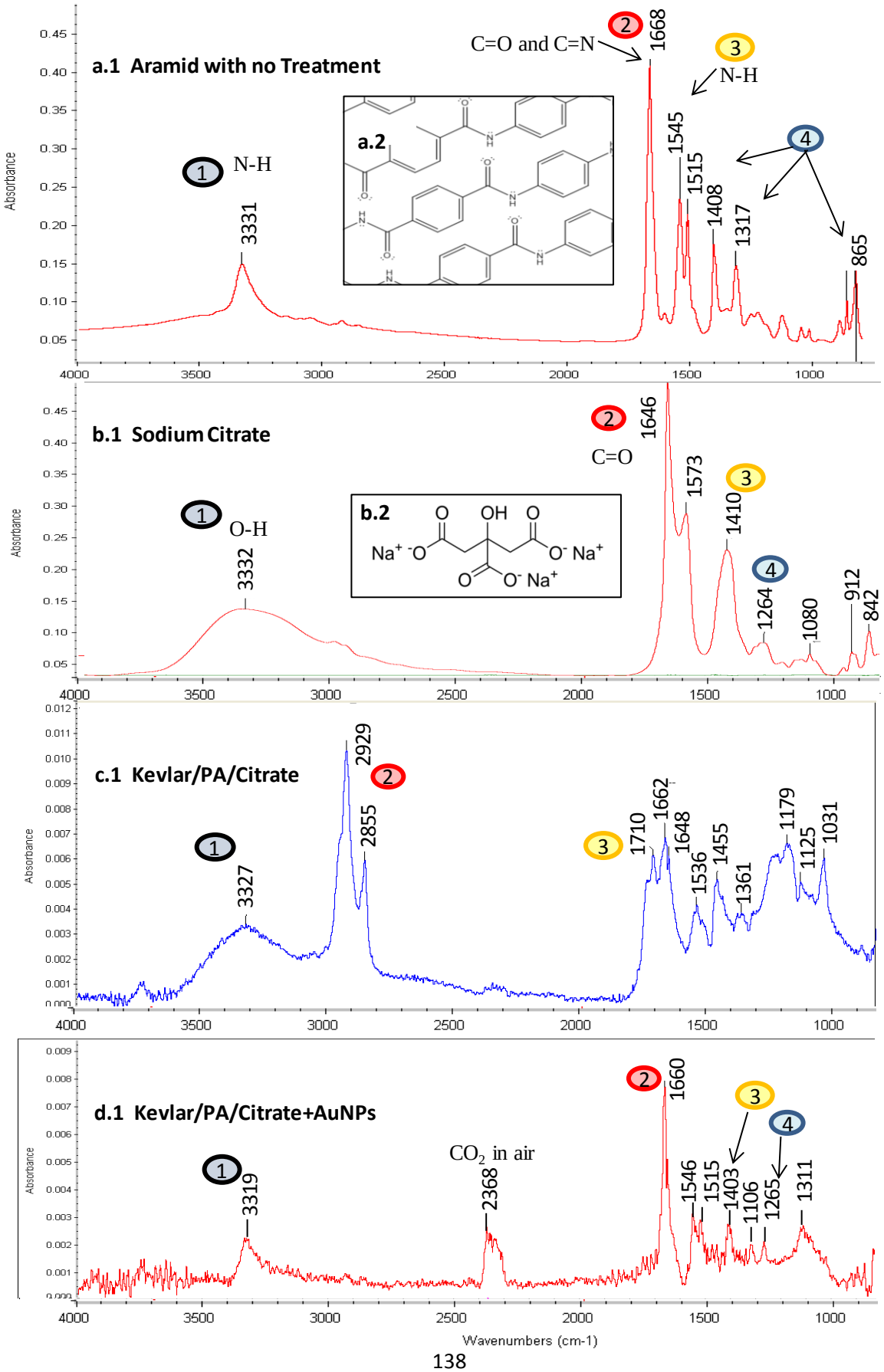
a.1 Aramid with no Treatment
C=O and C=N
1668
N-H
3331
1545
1515
1408
1317
865
a.2
b.1 Sodium Citrate
C=O
1646
1573
1410
O-H
3332
1264
1080
912
842
b.2
c.1 Kevlar/PA/Citrate
2929
2855
3327
1710
1662
1648
1536
1455
1361
1179
1125
1031
d.1 Kevlar/PA/Citrate+AuNPs
1660
3319
CO2 in air
2368
1546
1515
1403
1106
1265
1311
Absorbance
Wavenumbers (cm-1)

Figure 7.9. (a.1) FTIR spectrum of unreacted Kevlar nanofiber network (i.e. Sample No Treatment), showing peaks at (1) 3331 cm^{-1}, (2) 1668 cm^{-1}, (3) 1545 cm^{-1} and (4) the fingerprint region with corresponding microstructure (a.2). FTIR spectrum (b.1) of sodium citrate, dissolved in de-ionized water and dried prior to inspection, showing peaks at (1) 3332 cm^{-1}, (2) 1646 cm^{-1}, and its corresponding structure (b.2). FTIR spectrum (c.1) of Kevlar/PA/citrate sample, i.e. Sample Cit-13, showing peaks at (1) 3327 cm^{-1}, (2) 2929 cm^{-1} and 2855 cm^{-1} and (3) 1710 cm^{-1}. (d.1) FTIR spectrum of Kevlar/PA/citrate+AuNPs sample, i.e. Sample PA-0.3, showing peaks at (1) 3319 cm^{-1}, (2) 1660 cm^{-1} and (3) 1403 cm^{-1} and (4) 1265 cm^{-1}.

7.2.3 Effect of the PA/Citrate+AuNP Treatment on the Aramid Network Morphology

The effect of the PA/citrate+AuNP treatments on the formation of the networks was visualized using TEM to observe the morphology of the solid product left behind after evaporation from a TEM grid (Figure 7.10). Figure 7.10.a shows the carbon-coated copper grid as a reference for the subsequent images. Without any chemical treatment, the morphology in Figure 7.10.b consists of a 3D randomly oriented network of ANFs with the corresponding FTIR spectrum and chemical structure shown in Figure 7.9 a.1 and a.2 [1]. The morphologies of Samples PA-0.1 and 0.4 (with 0.1 mL or 0.4 mL PA respectively, 3.6 mg AuNPs and 13 mg citrate) after each treatment step are shown in Figure 7.10 (c to f). Figure 7.10.c shows that the nanofibers swelled in the presence of a limited amount of PA. After PA-treatment, the hydrolyzed aramid molecules on the nanofibers were crosslinked via secondary bonding by adding the citrate/AuNP solution. This resulted in an ANF network doped with AuNPs (Figure 7.10.d). Figure 7.10.e shows that when a larger amount of PA hydrolysis was done on the ANFs, as in Sample PA-0.4, nanosheets rather than nanofibers were formed after evaporation. The addition of the citrate/AuNP solution resulted in the restoration of a continuous network (Figure 7.10.f), containing AuNPs that are again crosslinked to the ANFs via hydrogen bonds. In both cases the final products (Figure 7.10.d and f) contain AuNPs with good dispersions.

These observations on morphology provide insight into the different mechanical properties of the PA/citrate+AuNP treated samples. The samples prepared with relatively smaller amounts of PA (Samples PA-0.2 and 0.3 in Figure 7.2 with 0.2 mL and 0.3 mL PA respectively and 13 mg citrate/3.6 mg AuNPs) and, hence, with less hydrolysis (*i.e.*, with more of the stiff aramid backbone molecules preserved), were stiffer than those that underwent more hydrolysis (Samples PA-0.4 and 0.5 with 0.4 mL and 0.5 mL PA respectively and 13 mg citrate/3.6 mg AuNPs), as over-hydrolysis breaks down the nanofibers. For the same extent of hydrolysis (Figure 7.3), the sample prepared with more citrate (Cit-13 with 0.3 mL PA and 13 mg citrate), had more citrate interactions among the hydrolyzed chains, because the number of crosslinking sites was not saturated and was stiffer than its counterpart (Cit-4 with 0.3 mL PA and 4 mg citrate) [1]. The fact that AuNPs can be well-dispersed and attached to the aramid matrix, as observed in Figures 7.10.d and f, enhances their effect as a reinforcement phase in the network, as just a small weight fraction of AuNPs (e.g. 6 wt% in Sample PA-0.3), improved the stiffness, strength and strain to failure of the aramid network (Figure 7.4). With this PA/citrate+AuNP treatment, Sample PA-0.3 is essentially the optimal condition for high stiffness and yield strength, since the network consisted of 1) an optimized hydrolysis level, compared with Samples PA-0.1, 0.2 with limited reactive sites for bonding and Samples PA-0.4, 0.5 with nanosheets owing to over hydrolysis; and 2) an amount of citrate/AuNPs that met or exceeded the amount needed to saturate the interaction sites (based on Sample Au-Cit-7.2 with the same amount of PA but higher amounts of citrate and AuNPs), ensuring that the hydrolyzed sites on the ANFs were bonded to the maximum extent.

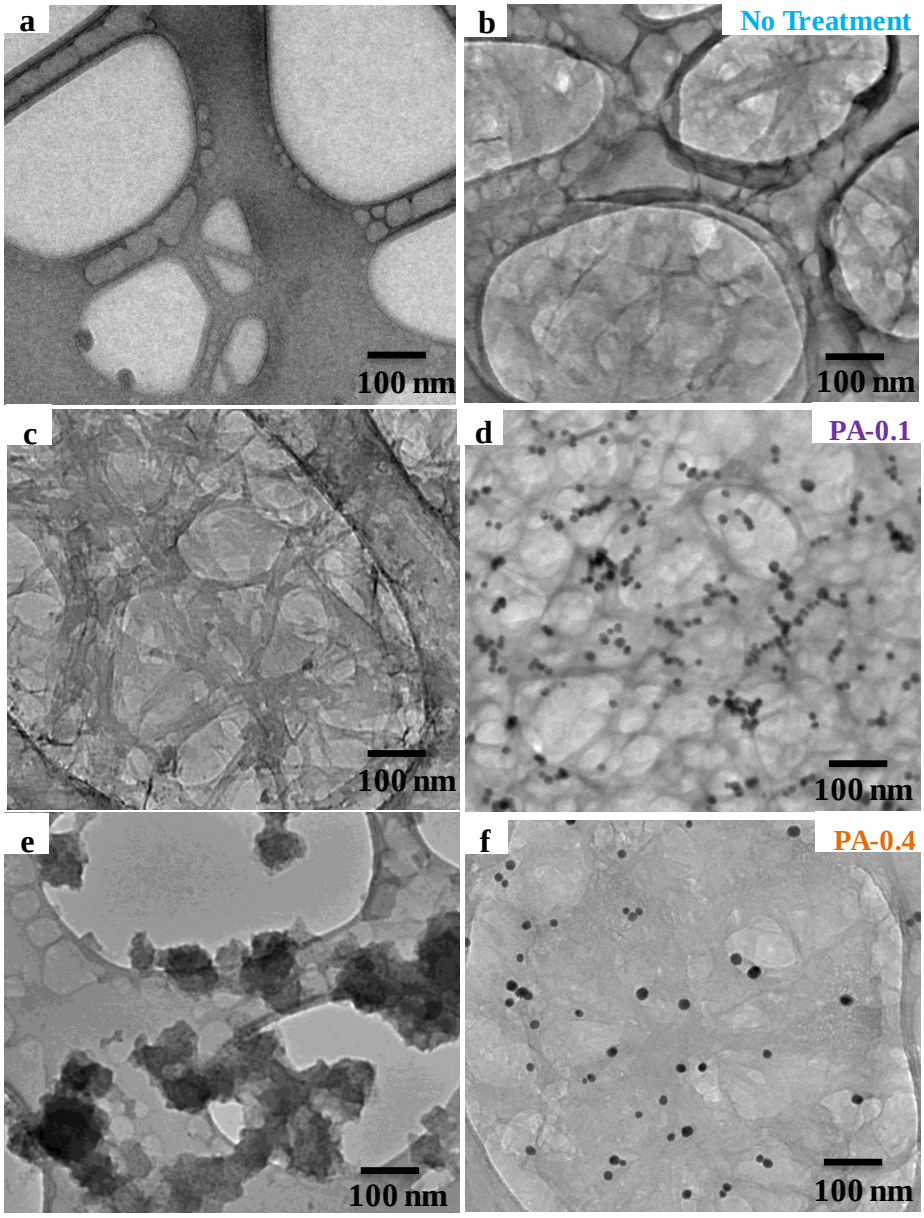

Figure 7.10 TEM images showing a) a carbon-coated copper grid used as a support for the TEM characterization of the networks, and the solid left after evaporation of the aramids dispersed in a DMSO solution b) with no treatment; c) after treatment of 0.1 mL PA for 40 mg Kevlar (as in Sample PA-0.1 but without citrate/AuNP treatment); d) after a further citrate/AuNP treatment (as in Sample PA-0.1); e) after treatment of 0.4 mL PA for 40 mg Kevlar (as in Sample PA-0.4 but without citrate/AuNP treatment): PA-catalyzed hydrolysis turning nanofibers into reactive nanoscale sheets; f) restored aramid network from nanosheets in (e) after a further citrate/AuNP treatment (as in Sample PA-0.4). The changes of the network morphologies correspond to the changes of their mechanical properties characterized by uniaxial tensile tests.

7.2.4 Interactions between AuNPs and Aramid Networks

The nature of the interactions between AuNPs and aramid nanostructures both in solutions and in solid films was investigated using Ultraviolet–visible (UV-vis) spectroscopy. The UV-vis spectra in Figure 7.11 show broadening and red-shifting of the absorption spectra near 557 nm as a result of the functionalized aramid molecules adsorbed onto citrate-AuNPs. This adsorption indicates interactions between citrate-AuNPs and aramid molecules through hydrogen and metal-organic electrostatic bonding, promoting load transfer between AuNPs and the aramid matrix, which explains the effectiveness of using AuNPs as reinforcements. Figure 7.11.a is the UV/vis spectrum of a ruby-colored solution of 13-nm AuNPs in citrate, which shows the well-known characteristic plasmonic absorption peak of AuNPs near 557 nm [3, 16]. This peak is red-shifted and broadened upon the citrate/AuNP treatment with a PA-hydrolyzed aramid nanostructure solution (i.e. PA-treated Kevlar/KOH/DMSO solution), which indicates a reduced nanoparticle-nanoparticle distance and a change in the refractive index, resulting from the hydrolyzed aramid molecules adsorbed onto the citrate-stabilized AuNPs [16, 17**]**. The red-shifting and broadening of the characteristic AuNP peak near 557 nm is also observed in the solid films (Sample PA-0.3 from Figure 7.11.b), formed by filtering the Kevlar/PA/citrate+AuNP solution in Figure 7.11.a. This consistency of the AuNP peak broadening and shifting (Figures 7.11.a and b) further confirms the interactions between AuNPs and the aramid matrix.

Compared to the ANF network with no treatment (Figure 7.11.c), the additional absorption peak of AuNPs in the PA/citrate+AuNP treated aramid network (i.e. Sample PA-0.3 in Figure 7.11.b) makes it a candidate material to be further developed for other applications such as solar cells, as it has both good absorption of visible light and great mechanical properties to sustain load and fracture [2]. The enhanced mechanical properties (Figure 7.2) and the enhanced visible light absorption (Figure 7.11.c) of the PA/citrate+AuNP treated aramid network (Sample PA-0.3) compared to the ANF network (Sample No Treatment) makes the PA/citrate+AuNP treatment a useful way to synthesize advanced aramid based nano-materials. Figure 7.11.c also shows that the ANF network (Sample No Treatment) and the PA/citrate+AuNP treated aramid network (Sample PA-0.3) share

overlapping peaks near 330nm of neutralized aramid and near 400 nm of aramid anion, both from the characteristic peaks of aramid molecules. These aramid peaks are further analyzed by combining with varied amounts of polyacrylic acid (PAA). Changes of the peak intensity and positions were observed owing to the structural changes in Kevlar/PAA composites, which will be discussed in our upcoming paper for a separate work by M. Yang et al in preparation.

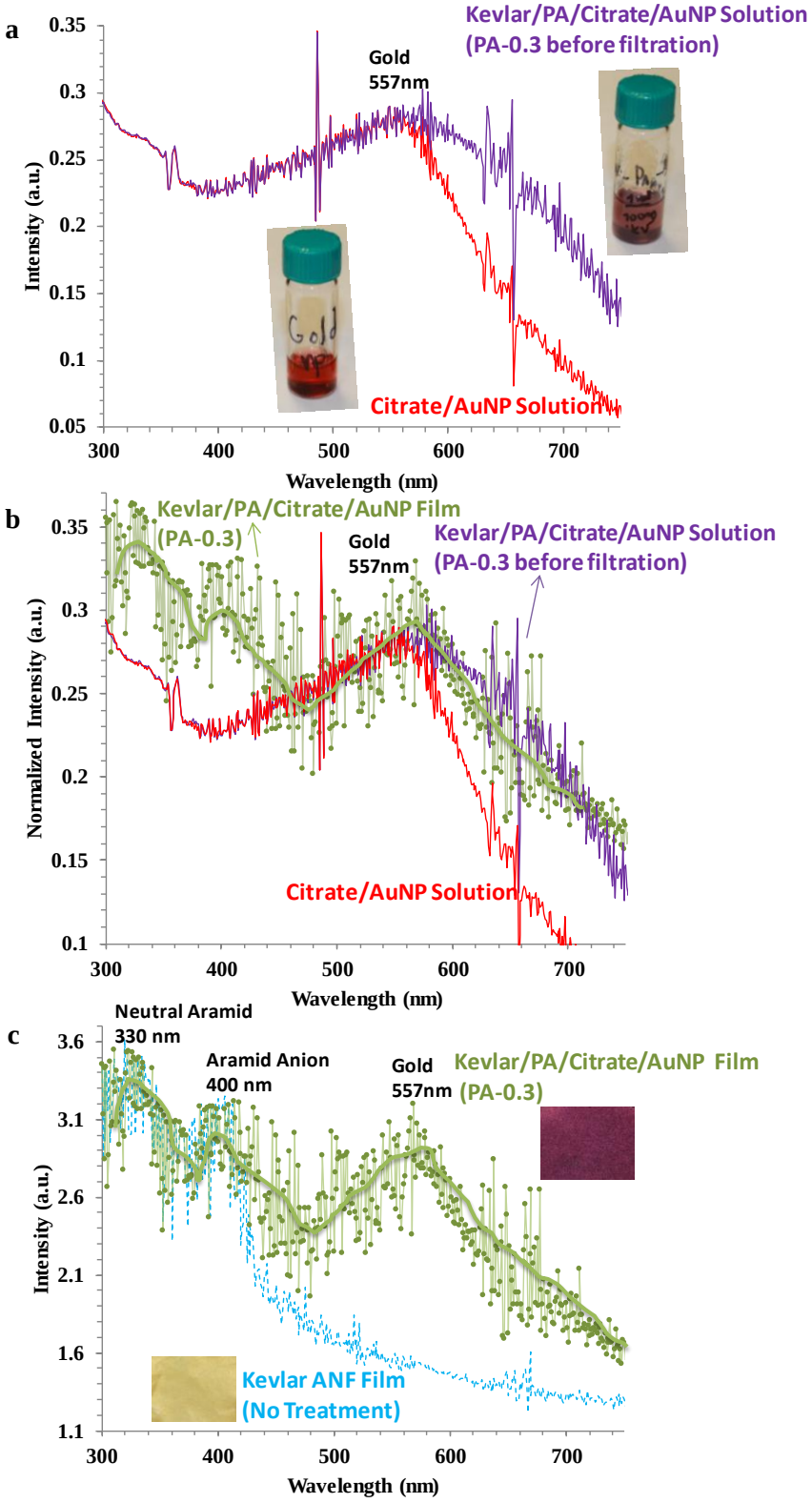

Figure 7.11. UV-vis spectra showing the broadening and red-shifting of the absorption peaks of AuNPs near 557nm: (a) comparison between the 13-nm AuNP solution in citrate and

Kevlar/PA/citrate+AuNP solution (Sample PA-0.3 with 0.3 mL PA, 13 mg Citrate and 3.6 mg AuNPs before filtration); b) comparison between the two solutions in (a) and the filtered solid film (i.e. Sample PA-0.3). The broadening and red-shifting phenomena are also observed in the solid. The broadening and red-shifting phenomena in the nanocomposite are indications of bonding between the AuNPs with the aramid network. c) A comparison between the ANF networks (Sample No Treatment) and the PA/citrate+AuNP treated aramid network (Sample PA-0.3). Besides the absorption peaks of aramid at 330 and 400 nm, the sample with AuNPs show a prominent absorption peak of gold at 557 nm compared to the sample with no treatment.

7.3 Thermal Properties of Aramid Nanostructured Networks

The characteristic decomposition phenomena of the aramid networks in air is characterized by thermogravimetric analysis (TGA), which reveals their excellent thermal stabilities, as well as enhancement of the high-temperature stabilities associated with the structural changes in the networks resulting from the chemical treatments. As indicated in Figures 7.12 (a and b), the thermal stabilities of the ANF network (Sample No Treatment) were exceeded by those of the PA/citrate-treated network (Sample Cit-13 with 0.3 mL PA and 13 mg citrate). The PA/citare+AuNP treated network (Sample PA-0.3 with 0.3 mL PA, 13 mg citrate and 3.6 mg AuNPs) had even higher thermal stability. These improvements in thermal stability properties followed the same trend as their mechanical properties. The addition of citrate and AuNPs to promote bonding among the aramid nanostructures in the network also promoted higher thermal stability. The decomposition rate (Figure 7.12.b) of the ANF network peaks at ~ 600 ^{0}C and the network decomposes completely at ~ 760 ^{0}C. As a comparison, the decomposition of the network with PA/citrate treatment peaks at ~ 700 ^{0}C and is completed at ~ 800 ^{0}C. This enhancement of the characteristic decomposition temperature is an another indication that additional bonding by citrate improves the interactions among the aramid nanostructures in the networks by creating covalent bonding, compared to the secondary bonding in the ANF networks. The addition of AuNPs in the Kevlar/PA/citrate+AuNP network (Sample PA-0.3) further improves the thermal stability, as

the inorganic AuNPs don't decompose at this temperature range and they remain at the end of TGA. The remaining mass fraction at 900 ^{0}C of Sample PA-0.3 in Figure 7.12.a indicates that there is 6 wt% of AuNPs in the network, which agrees well with the synthesis condition in which 3.6 mg AuNPs was added to 40 mg Kevlar along with 13 mg citrate to give 6.4 wt% of AuNPs. This agreement between the weight fractions is also a good indication that the AuNPs are bonded to the aramid matrix and thus don't get filtered during synthesis.

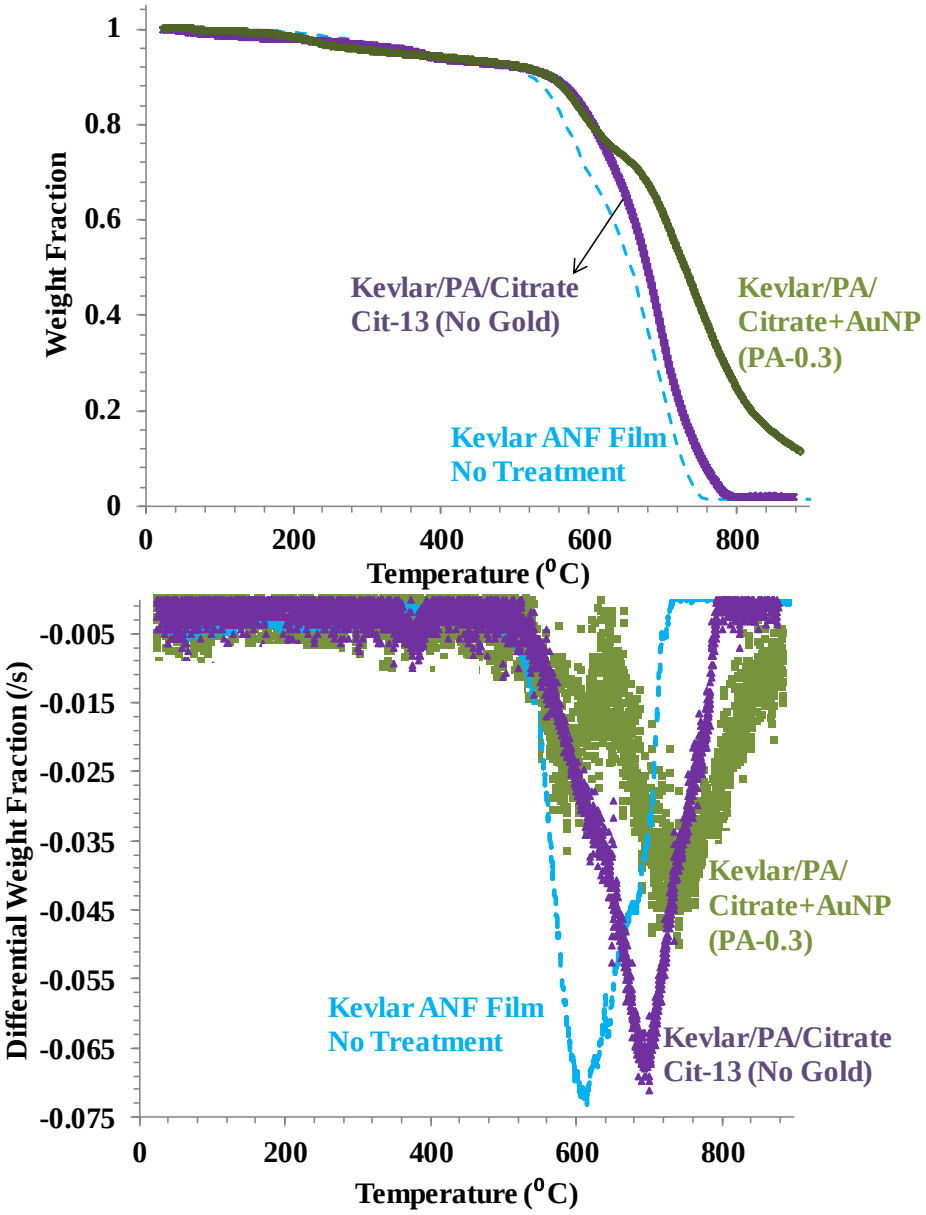

Figure 7.12. Characterization of the network thermal properties. a) Thermogravimetric response in air of the networks (with no treatment, with PA/citrate treatment, and with PA/citrate+AuNP-treatment) at a temperature rise of 10 °C/min. The higher thermal stability at high temperatures of the treated networks came from enhanced level of bonding among aramid nanostructures through citrate. The un-decomposed inorganic AuNPs further improved the thermal stability. b) Rate of weight fraction decrease vs. temperature from the same TGA tests in (a). The raised temperatures of the peak decomposition rates in the treated samples also support the treatment effects on the network structures and properties, indicating enhanced interactions among aramid nanostructures and their bonding with AuNPs.

7.4 Desired Structure of AuNPs Reinforced Aramid Networks

Although the current synthesis condition limits the type of the reactions we can pursue, two chemical reactions between citrate and hydrolyzed aramids are desired and proposed for a stronger chemical attachment of AuNPs and crosslinking among the aramid nanostructures. These reactions will yield a highly crosslinked aramid matrix with chemically attached AuNPs, as shown in Figure 7.13 and the covalent bonding among the aramid nanostructures enhances the interactions among them even further which could lead to improved network mechanical properties such as stiffness, strength and toughness. Figure 7.14 shows a proposed/desired amide condensation reaction between a carboxylic acid from a citrate molecule and an amine from a hydrolyzed aramid molecule. Figure 7.15 shows a proposed/desired ester condensation between a carboxylic acid from a hydrolyzed aramid molecule and a hydroxyl group from a citrate molecule. These reactions are hard to achieve through the current synthesis condition, but are very favorable for obtaining covalently bonded aramid nanostructures and thus higher network stiffness and strength. The amide condensation in Figure 7.14 is favored by the high stability of the products and the relatively large number of the reactive groups, as there are three carboxylic acids per citrate molecule. However, these carboxylic acid groups are also stabilized as they form complexes with the AuNPs, which reduces their likelihood to react with the amines from hydrolyzed aramid molecules. The ester condensation in Figure 7.15 is favored by the high electron density, i.e. low conjugation, of the hydroxyl group from each citrate molecule, which increases the nucleophilicity of this functional group, and the high conjugation, i.e. stability, of the esteric product. However, there is only one hydroxyl per citrate molecule, which makes this functional group sterically hindered and reduces its likelihood to react with the hydrolyzed carboxylic acid.

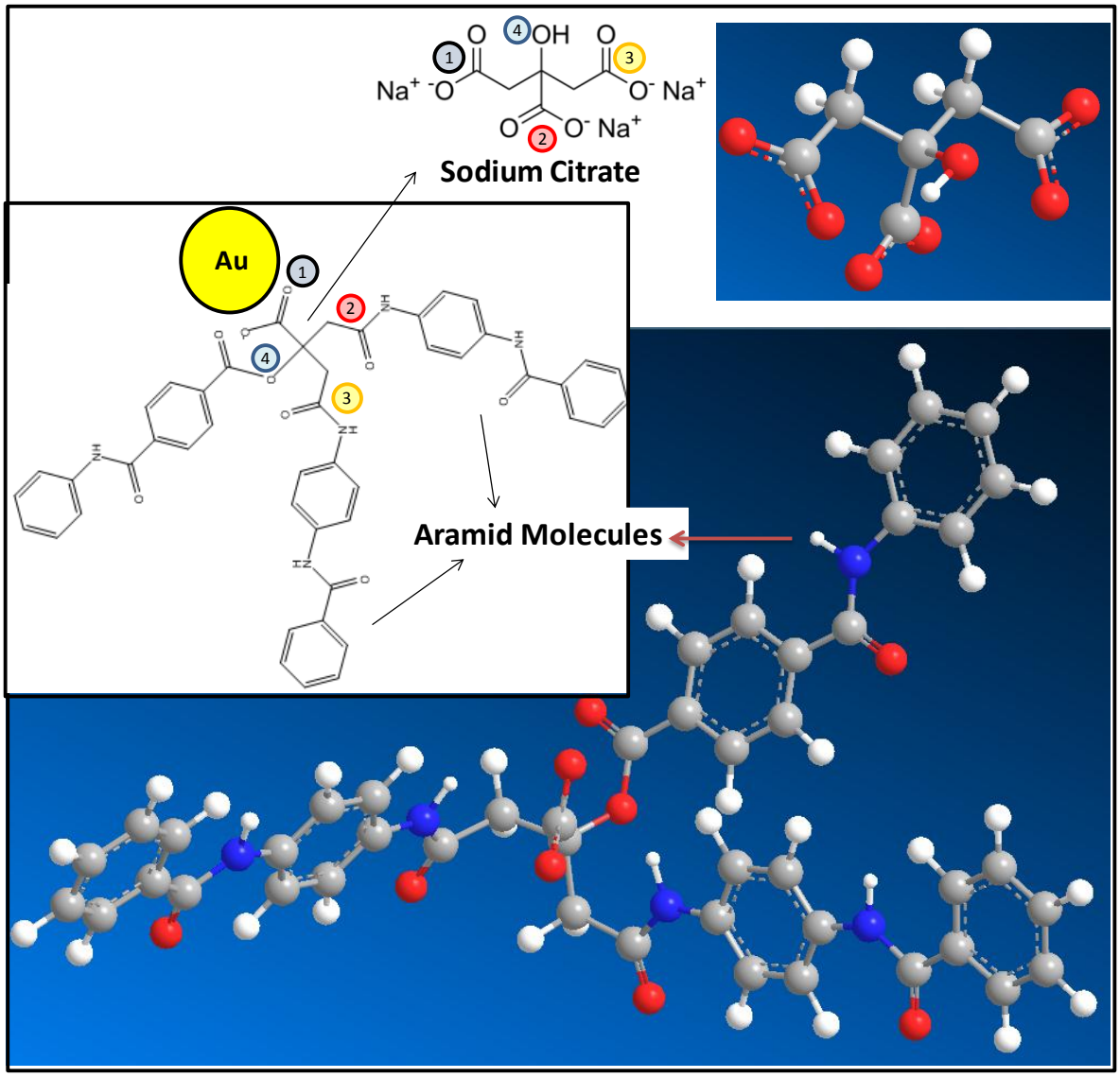

Figure 7.13 A desired aramid network with attached AuNPs through bonding with citrate. A network with well-bonded constituents is desired for obtaining composites with desirable mechanical properties. The four functional groups, three COOH groups and one OH group, from citrate molecules are attached to hydrolyzed aramid molecules or AuNPs.

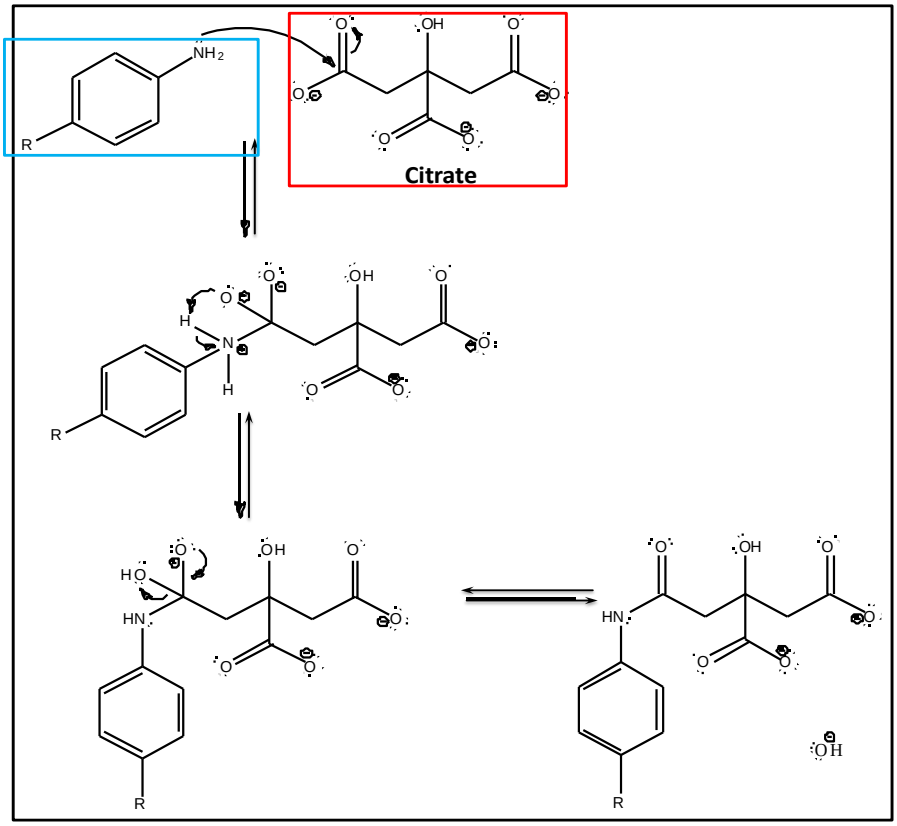

Figure 7.14 Proposed and desired amide condensation reaction of hydrolyzed aramid molecules with a carboxylic acid from a citrate molecule, showing favorable bonding between citrate and aramid molecules that is stronger than the current hydrogen bonding between them. R = Kevlar nanofiber.

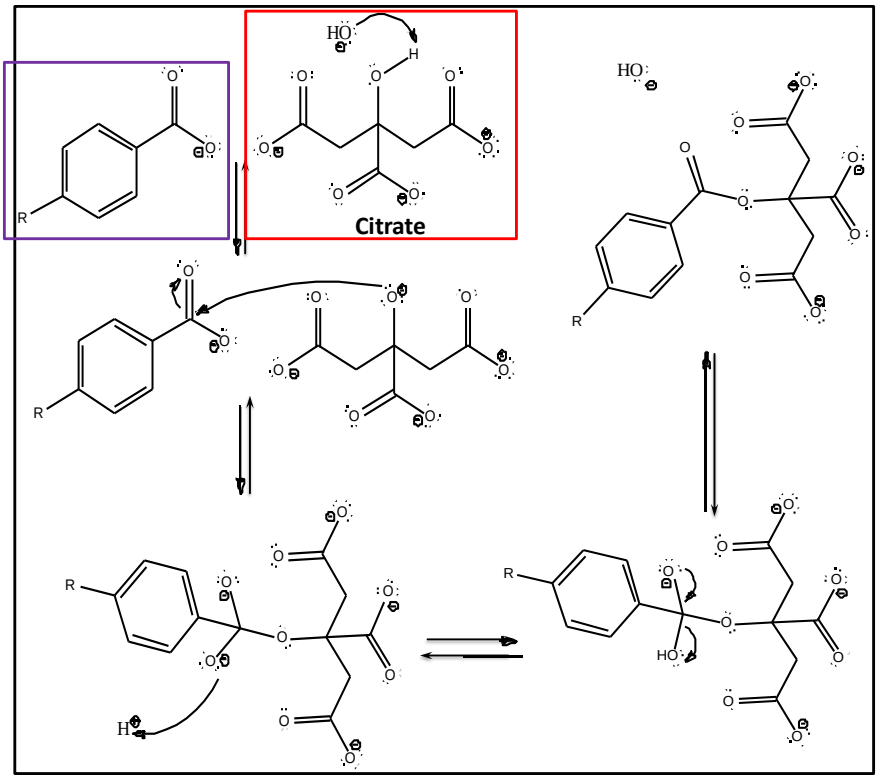

Figure 7.15 Proposed and desired ester condensations of hydrolyzed aramid molecules with a hydroxyl group from a citrate molecule, showing another favorable bonding between them that can provide stronger interactions than hydrogen bonding. R = Kevlar nanofiber.

Stronger interaction between the bonding ligand and AuNPs can also be perused for better mechanical properties. Thoil, an organosulfur compound that contains a carbon-bonded sulfhydryl (–C–SH or R–SH) group, is well known for forming strong bonding with gold [18]. The sulfur-gold interaction is on the order of 45 kcal/mol, which forms a stable and semi-covalent bond [19]; in comparison, the C–C bond strength is ~83 kcal/mol. Future work can be focused on crosslinking thoil groups with the aramid matrix so that strong interaction between AuNPs and aramid matrix can be achieved. This strong interaction can lead to shearing and deformation of the metal particles for an additional energy dissipation mechanism and thus higher material toughness.

7.5 Summary and Conclusions

Through careful investigations, how phosphoric acid, citrate and gold nanoparticles affect the macroscopic properties of the aramid nanostructured networks through controlling their nanostructures and morphologies were demonstrated and discussed. Phosphoric acid serves as a functionalizer to bring more functional groups on the surface of nanofibers for bonding. Citrate forms hydrogen bonding with the hydrolyzed aramid nanostructures and enhances interactions among them. Gold nanoparticles reinforce the network effectively and improve the network stiffness and strength without reducing their strain to failure. Smaller particle size is more desired as it offers a larger surface area for the same amount of AuNPs to bond with other constitutions in the network. This understanding of the effects of the PA/citrate+AuNP treatment on the resultant macroscopic network properties provides a structure-property relationship that is used to optimize the Kevlar/PA/citrate+AuNP system for obtaining best mechanical properties.

The Kevlar/PA/citrate+AuNP nanocomposite also compares favorably with the commercial Kevlar mat. Figure 7.16 shows a comparison between the stress-strain curves of Kevlar/PA/citrate+AuNP nanocomposites and Kevlar mats, characterized by uniaxial tensile testing. The properties of the Kevlar mat were characterized along its strongest axis, i.e. the fiber axis. The Kevlar/PA/citrate+AuNP nanocomposite has a higher strain energy density than that of Kevlar mat measured along its strongest axis. This indicates the promising future potential of the aramid nanocomposites for applications as tough materials to resist extreme loading conditions, such as high strain rate blast and ballistic impact.

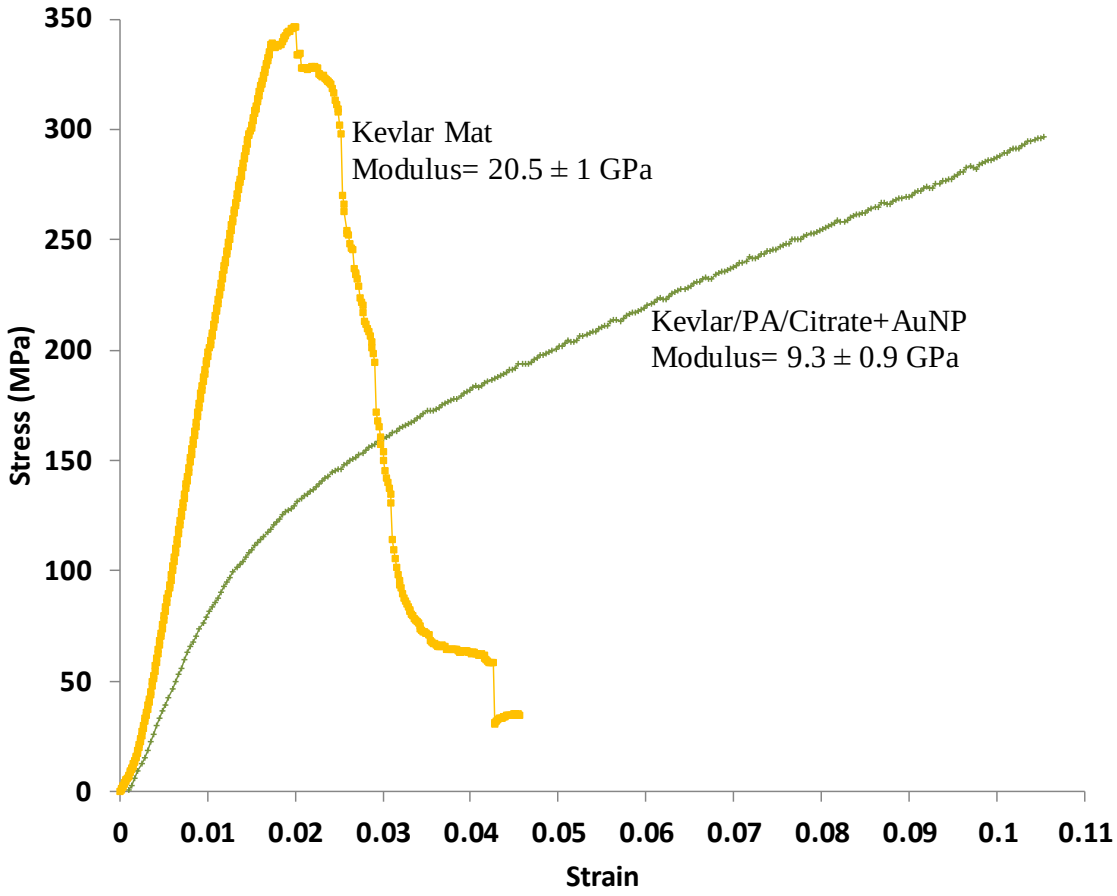

Figure 7.16 In-plane mechanical properties of Kevlar mat tested along its strongest axis and Kevlar/PA/citrate+AuNP nanocomposites, characterized by uniaxial tensile testing at 0.005/s. The Kevlar/PA/citrate+AuNP nanocomposites have a higher strain to failure and a higher strain density than those of Kevlar mat tested along its strongest axis, which makes the nanocomposites a potential material for resisting extreme loading conditions.

Reference

[1] K. Cao, C. Pons Siepermann, M. Yang, A. M. Waas, N. A. Kotov, M. D. Thouless, and E. M. Arruda, "Reactive Aramid Nanostructures as High-Performance Polymeric Building Blocks for Advanced Composites," *Adv. Funct. Mater.* **2013**, Vol. 23, pp. 2072–2080.

[2] Q. Liu, Y. Cui, D. Gardner, X. Li, S. He and I. I. Smalyukh, "Self-Alignment of Plasmonic gold Nanorods in Reconfigurable Anisotropic Fluids for Tunable Bulk Metamaterial Applications," *Nano Lett.* **2010**, Vol. 10, pp. 1347-1353.

[3] J. H. Lee, J. H. Park, J. S. Kim, D. Y. Lee and K. Cho, "High efficiency polymer solar cells with wet deposited plasmonic gold nanodots," Organic Electronics **2009**, Vol. 10, pp. 416-420.

[4] M. Yang, K. Cao, L. Sui,Y. Qi, J. Zhu, A. M. Waas, E. M. Arruda, J. Kieffer, M. D. Thouless, N. A. Kotov, "Dispersions of ANSs: A New Nanoscale Building Block," *ACS Nano* **2011**, Vol. 5, No. 9, pp. 6945–6954.

[5] G. Frens, "Controlled Nucleation for the Regulation of the Particle Size in Monodisperse Gold Suspensions', *Nat. Phys. Sci.* **1973**, Vol. 241, pp. 20-22.

[6] W. Sweeny, "Improvements in Compressive Properties of High Modulus Fibers by Crosslinking," *J. Polym. Sci., Part A: Polym. Chem.* **1992**, Vol. 30, pp. 1111-1122.

[7] S. Park, M. Seo, T. Ma, D. Lee, "Effect of Chemical Treatment of Kevlar Fibers on Mechanical Interfacial Properties of Composites," *J. Colloid Interface Sci.* **2002**, Vol. 252, pp. 249-255.

[8] G. Li, C. Zhang, Y. Wang, P. Li, Y. Yu, X. Jia, H. Liu, X. Yang, Z. Xue, S. Ryu, "Interface Correlation and Toughness Matching of Phosphoric Acid Functionalized Kevlar Fiber and Epoxy Matrix for Filament Winding Composites," *Compos. Sci. Technol.* **2008**, Vol. 68, pp. 3208-3214.

[9] Z. Yu, A. Ait-Kadi, J. Brisson, "Nylon/Kevlar Composites. I: Mechanical Properties," *Polym. Eng. Sci.* **1991**, Vol. 31, No. 16.

[10] M. Rajabian, C. Dubois, "Polymerization Compounding of HDPE/Kevlar Composites. I. Morphology and Mechanical Properties," *Polym. Compos.* **2006**, Vol. 27, Issue 2, pp. 129-137.

[11] F. Guo, Z. Zhang, W. Liu, F. Su, H. Zhang, "Effect of Plasma Treatment of Kevlar Fabric on the Tribological Behavior of Kevlar Fabric/Phenolic Composites," *Tribol. Int.* **2009**, Vol. 42, pp. 243-249.

[12] T. K. Lin, S. J. Wu, J. G. Lai, S. S. Shyu, "The Effect of Chemical Treatment on Reinforcement/Matrix Interaction in Kevlar-fiber/Bismaleimide Composites," *Compos. Sci. Technol.* **2000**, Vol. 60, pp. 1873-1878.

[13] Penn L. and Milanovich F., "Raman spectroscopy of Kevlar 49 fiber," *Polymer* **1979**, Vol. 20, pp. 31-36.

[14] Andrews M. C. and Young R. J., "Analysis of the Deformation of Aramid Fibres and Composites Using Raman Spectroscopy," *J. Raman Spectrosc.* **1993**, Vol. 24, pp. 539-544.

[15] C.P. Sherman Hsu, in: F. Settle (Ed.), Handbook of Instrumental Techniques for Analytical Chemistry, Prentice-Hall, NJ, 1997, p. 254.

[16] M. Brust, B. Bethell, C. J. Kiely and D. J. Schiffrin, "Self-Assembled Gold Nanoparticle Thin Films with Nonmetallic Optical and Electronic Properties," *Langmuir* **1998**, Vol. 14.

[17] J. Cho and F. Caruso, "Investigation of the Interactions between Ligand-Stabilized Gold Nanoparticles and Polyelectrolyte Multilayer Films," *Chem. Master*. **2005**, Vol. 17, pp. 4547-4553.

[18] Nuzzo, R. G. and Allara, D., "Adsorption of bifunctional organic disulfides on gold surfaces," *J. Am. Chem. Soc.* **1983**, Vol. 105, pp. 4481-4483.

[19] Dubois, L. H. and Nuzzo, R. G., "Synthesis, structure, and properties of model organic surfaces," *Annu. Rev. Phys. Chem.* **1992**, Vol. 43, pp. 437-463.

Chapter 8

Conclusions and Future Directions

8.1 Conclusions

The research presented in this work has addressed several issues facing the design of aramid-based nanocomposites. Aramid nanofibers (ANFs) are an exciting new toolset as building blocks for nanocomposites. However, their lack of affinity for bonding makes it hard to obtain aramid-based nanocomposites with ultra-high stiffness, strength and ductility. Investigations to probe structure-property relationships of different aramid-based networks reveal several strategies to obtain optimized synthesis methods for making nanocomposites. Some of the key findings of this research are summarized below:

- Commercial Kevlar microfibers and yarns are anisotropic, inert and have been primarily used as reinforcement phase in nanocomposites or woven in mats. Aramid nanofibers can be used as matrix materials to form transversely isotropic and possibly isotropic networks in the form of thin films and they can also be made reactive through chemical treatments.
- Aramid nanofibers can be functionalized and crosslinked through chemical treatment, which controls the bonding among aramid macromolecules. Phosphoric acid (PA) hydrolyzes ANFs to make them reactive for bonding with crosslinkers such as glutaradehyde (GA) or citrate. Gold nanoparticles (AuNPs) can be used as an effective reinforcement phase to further improve the network stiffness and strength without reducing its strain to failure. The PA/GA treatment and the PA/citrate+AuNPs treatment control the building block nanostructure and the network morphology and thus can tailor the resulting network mechanical properties.

- The aramid nanofiber/gold nanoparticle composites have higher strain energy (i.e. work to fracture) than that of commercial Kevlar mat tested along its strongest axis. This higher toughness, measured as 2.50 MPa$\sqrt{m}$, provides promising potential for the aramid nanocomposites as tough materials to resist extreme loading conditions, such as high strain rate blast and ballistic impact. The combination with AuNPs also opens doors for the exploration of other properties, such as light-absorption or electrical conductivity.
- The stiffness of the aramid nanofiber networks without any treatment is controlled by the ANF morphology and curvature, which are controlled through different assembly methods. Layer-by-layer (LBL) assembly yields randomly orientated nanofibers in the plane parallel to the substrate, i.e. a 2D random orientation of nanofibers. Vacuum-assisted filtration yields a 3D random fiber orientation which results in lower in-plane stiffness compared to that of an ANF film assembled by LBL. The curved fiber geometry and increased randomness in the fiber orientation reduce the in-plane stiffness of the networks compared to that of the commercial Kevlar mat tested along the direction of its highly aligned straight fibers.

8.2 Future Work

Future investigation can be focused on the characterization of the high strain rate mechanical properties of aramid nanocomposites, in order to evaluate their performance and applicability as materials to resist impacts, such as blast loadings. To understand aramid nanocomposite behaviors at strain rates on the orders of 10^3 /s, split Hopkinson pressure bar (SHPB) experiments can be investigated. Figure 8.1 shows the mechanical behavior of aramid nanocomposites at three different strain rates characterized by a low-strain RSA III DMA machine, a high-speed actuator and a tensile SHPB. Strain rate dependence of the material was revealed where higher stiffness and strength were measured at higher strain rates. Dynamic mechanical analysis with frequency sweep testing is another method that can be applied to the aramid nanocomposites. Figure 8.2 shows such a test on the aramid nanofiber/gold nanoparticle composite (the Kevlar/PA/Citrate+AuNP sample with 0.3 mL PA, 13 mg Citrate and 3.6 mg (13nm) AuNPs in Chapter 7). The storage modulus increases and

the tanδ drops with the increase of the frequency (strain rate). These data can also be used for constitutive modeling on the aramid nanocomposites to further understand their deformation mechanisms.

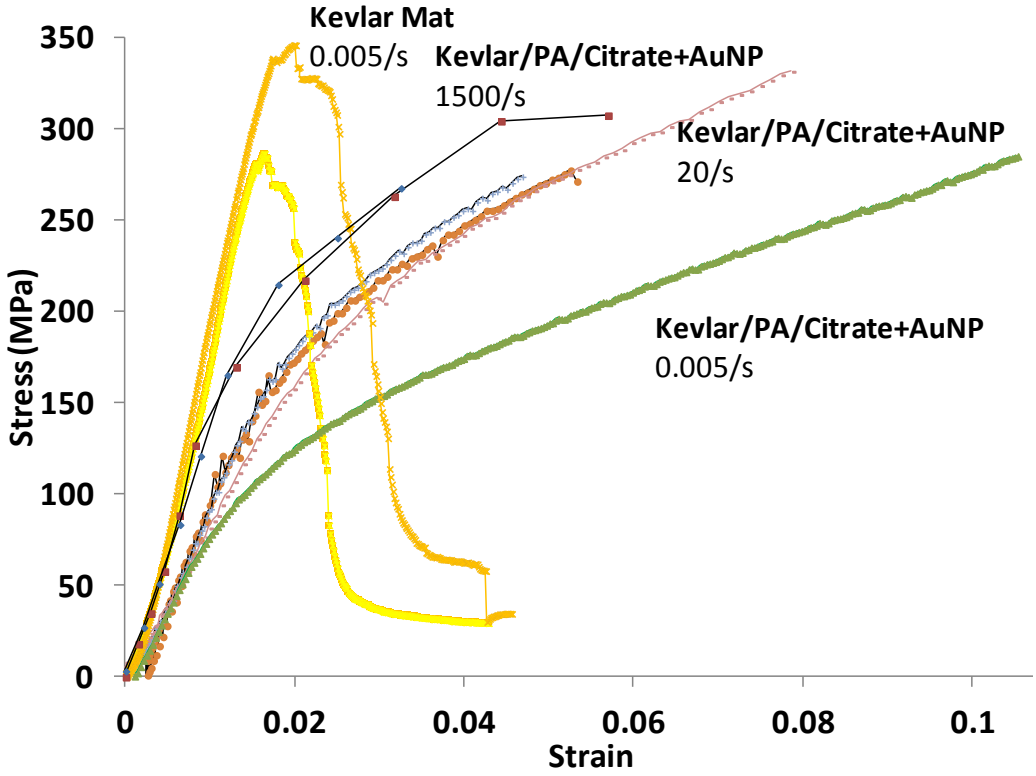

Figure 8.1 Uniaxial tensile testing of aramid nanofiber/gold nanoparticle composites (the Kevlar/PA/citrate+AuNP nanocomposites in Chapter 7 with 0.3 mL PA, 3.6 mg (13nm) AuNPs and 13 mg citrate) at different strain rates with comparison with that of commercial Kevlar mat with plain-woven fibers tested along its strongest axis. The ANF/AuNPs composite shows strain rate dependence of the mechanical properties, where stiffness and strength are higher at higher strain rates. Their strain to failure is still higher than that of the Kevlar mat at higher rates, which makes them attractive candidates for high rate application.

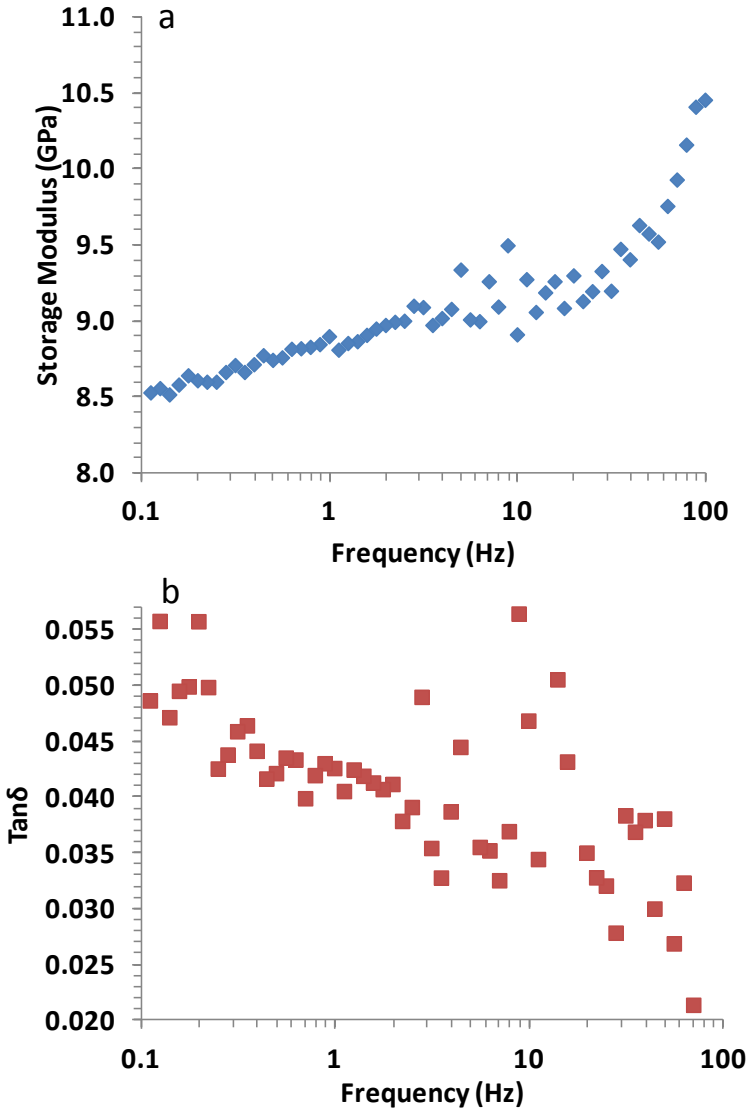

Figure 8.2 Dynamic mechanical analysis with a frequency sweep at room temperature on the aramid nanofiber/gold nanoparticle composite (the Kevlar/PA/AuNP sample with 0.3 mL PA, 3.6 mg (13nm) AuNPs and 13 mg citrate in Chapter 7). A pre-strain of 0.5 % and a strain oscillation of 0.1 % were applied. The storage modulus increases and the loss tangent (tanδ) decreases with the frequency increase.

Other high-strain rate testing such as blast testing can also be implemented to investigate the material behavior and evaluate its performance as a potential material in body armor and helmets. Figure 8.3 shows hotpressed and free-standing films of the same aramid nanocomposites characterized in Figures 8.1 and 8.2. A blast wave, as shown in Figure 8.4a, was used to load the samples and the deformation pattern, i.e. the center deflection, was obtained through digital image correlation analysis. Figure 8.4 compares two center deflection measurements of the hotpressed and free-standing films.

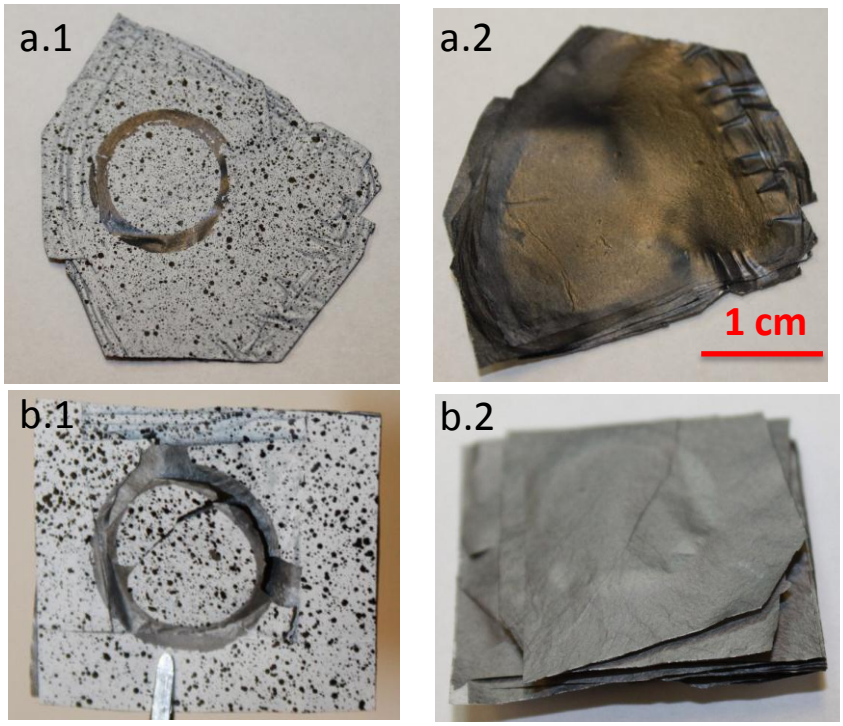

Figure 8.3 The aramid nanofiber/gold nanoparticle composite (the Kevlar/PA/AuNP sample with 0.3 mL PA, 3.6 mg (13nm) AuNPs and 13 mg citrate in Charpter 7) tested by blast. The optical images of a.1) the front and a.2) the back of the hotpressed aramid nanocomposite samples by pressing several films at 200 ^{o}F to form a thicker sample. The optical images of b.1) the front and b.2) the back of the free-standing aramid nanocomposite samples by stacking films together. The samples were clamped by an O-ring and the center deflection at the middle of the circular shape was measured during a blast.

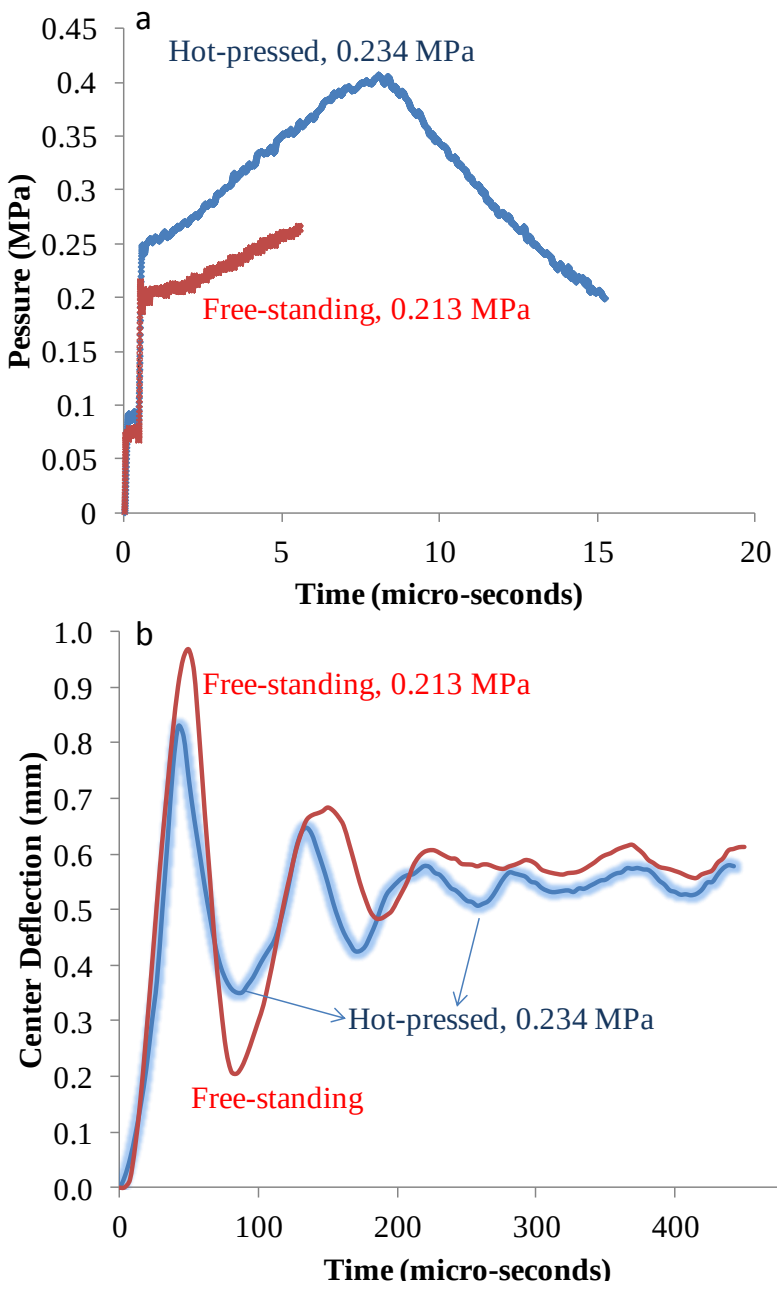

Figure 8.4 The center deflection of the aramid nanofiber/gold nanoparticle composite (the Kevlar/PA/AuNP sample with 0.3 mL PA, 3.6 mg (13nm) AuNPs and 13 mg citrate in Chapter 7) during a blast testing upon blast pressure loading. a) The pressure profile of the blast pulses applied on two types of samples. The levels of the pressure pulses are listed in the legend. b) The center deflection of the freestanding films and the hotpressed films. The freestanding films had a better damping behavior, as the deflection peaks damped out quicker. This was possibly caused by having more friction with air among the films in the freestanding sample, which served as an extra mechanism to dissipate energy.